Advanced Manufacturing Technology

Part 1

Edited by
Jian Gao

TRANS TECH PUBLICATIONS

Advanced Manufacturing Technology

Edited by
Jian Gao

Advanced Manufacturing Technology

Selected papers from the
2011 International Conference on
Advanced Design and Manufacturing Engineering
(ADME 2011)
16-18 September, 2011, Guangzhou, China

Edited by

Jian Gao

Trans Tech Publications Ltd
Kreuzstrasse 10
CH-8635Durnten-Zurich
Switzerland
http://www.ttp.net

Volumes314-316of 3-vol.-set
Advanced Materials Research
ISSN 1022-6680

Full text available online at *http://www.scientific.net*

***Distributed** worldwide by*

Trans Tech Publications Ltd
Kreuzstrasse 10
CH-8635Durnten-Zurich
Switzerland

Fax: +41 (44) 922 10 33
e-mail: sales@ttp.net

and in the Americas by

Trans Tech Publications Inc.
PO Box 699, May Street
Enfield, NH 03748
USA

Phone: +1 (603) 632-7377
Fax: +1 (603) 632-5611
e-mail: sales-usa@ttp.net

Preface

The present book includes a set of selected papers from the 2011 International Conference on Advanced Design and Manufacturing Engineering (ADME 2011), held in Guangzhou, China, from 16 to 18 September 2011, sponsored by Guangdong University of Technology, Huazhong University of Science and Technology, Hong Kong University of Science and Technology, Hong Kong Polytechnic University and University of Nottingham. The conference was organized in four simultaneous tracks: “Advanced Design Technology”, “Advanced Materials and Processes”, “Advanced Manufacturing Technology” and “Equipment Manufacturing Technology and Automation”.

All papers included in this book are under the scrutiny of peer and expert reviews before accepted for publication, and in accordance with high academic standard and quality. This book covers the subject areas of surface engineering/coatings, modeling, analysis and simulation of manufacturing processes, materials processing technology, mechanical behavior & fracture, material design of computer aided, tooling testing and evaluation of materials, thermal engineering theory and applications, CAM/CAE, high-speed/precision machining and inspection technology, micro-machining technology, laser processing technology, bionic mechanisms and bio-manufacturing, digital manufacture and management, the internet of things other related topics

On behalf of the conference organizing committee, we would like to thank all participants. First of all to the authors, whose quality work is the essence of the conference and to the members of the committee for their expertise and time. We also wish to thank all referees for their constructive comments.

Professor Dr. Jian Gao
Guangdong University of Technology, China

The 2011 International Conference on

Advanced Design and Manufacturing Engineering

(ADME 2011)

Organized by:

Guangdong University of Technology, China

Co-organized by:

Huazhong University of Science and Technology, China

Hong Kong University of Science and Technology

Hong Kong Polytechnic University

University of Nottingham, UK

Conference Organization

Chairman

Prof. Xin Chen, Guangdong University of Technology, China

Co-Chairman

Prof. Youlun Xiong, Huazhong University of Science and Technology, China

International Scientific Committee

Prof. Zexiang Li, Hong Kong University of Science and Technology, HK

Prof. Zhouping Yin, Huazhong University of Science and Technology, China

Prof. Xiangwei Zhang, Guangdong University of Technology, China

Prof. Guoqun Zhao, Shandong University, China

Prof. He Yang, Northwestern Polytechnical University, China

Prof. Jianmin Zeng, Guangxi University, China

Prof. W B Lee. Hong Kong Polytechnic University, HK

Prof. Yu Wang, Hong Kong Chinese University, China

Prof. Tian Huang, Tianjin University, China

Prof. Shijian Yuan, Harbin University of Technology, China

Prof. Hejun Li, Northwestern Polytechnical University, China

Prof. Xianghua Liu, Northeastern University, China

Prof. Jingtao Han, University of Science and Technology Beijing, China

Prof. Liping Chen, Huazhong University of Science and Technology, China

Prof. Yongsheng Zhao, Yanshan University, China

Prof. Xinyu Shao, Huazhong University of Science and Technology, China

Prof. Tianlong Gu, Guilin University of Electronic Technology, China

Prof. Xianmin Zhang, South China University of Technology, China

Prof. Xipeng Xu, Huaqiao University, China

Prof. Kaiyong Jiang, Huaqiao University, China

Prof. Jianhua Zhang, Shandong University, China

Prof. Fengzhou Fang, Tianjin University, China

Prof. Zhenduo Cui, Tianjin University, China

Prof. Shiping Zhao, Sichuan University, China

Prof. Yongkang Zhang, Jiangsu University, China

Prof. Jieyu Zhang, Shanghai University, China

Prof. Ming Chen, Shanghai Jiao Tong University, China

Prof. Yong Li, Tinghua University, China

Prof. Liqun Zhang, Beijing University of Chemical Technology, China

Prof. Yongping Lei, Beijing University of Technology, China

Prof. Zhenyuan Jia, Dalian University of Technology, China

Prof. Xuejun Jin, Shanghai Jiao Tong University, China

Prof. Juntang Yuan, Nanjing University of Science and Technology, China

Prof. Jiuhua Xu, Nanjing University of Aeronautics and Astronautics, China

Prof. Lin Hua, Wuhan University of Technology, China

Prof. Zhongxiu Shi, Qingdao University, China

Prof. Di Li, South China University of Technology, China

Prof. Rupeng Zhu, Nanjing University of Aeronautics and Astronautics, China

Prof. Wuyi Chen, Beijing University of Aeronautics and Astronautics, China

Prof. Bingyan Jiang, Central South University, China

Prof. Daoguo Yang, Guilin University of Electronic Technology, China

Prof. Zhijian Zong, Sun Yat-Sen University, China

Prof. Yong Tang, South China University of Technology, China

Prof. Junhe Yang, University of Shanghai for Science and Technology, China

Prof. Xiaochun Wu, Shanghai University, China

Prof. Liyang Xie, Northeastern University, China

Prof. Dong Gao, Harbin University of Technology, China

Prof. Baochun Lu, Nanjing University of Science and Technology, China

Prof. Yinbiao Guo, Xiamen University, China

Prof. Kaiming Wu, Wuhan University of Science and Technology, China

Prof. Shaohui Yin, Hunan University, China

Prof. Jinglong Bu, Hebei United University, China

Prof. GuoGuang Jin, Tianjin Polytechnic University, China

Prof. Pengcheng Wang, Inner Mongolia University of Technology, China

Prof. Lin He, Guizhou University, China

Prof. Shiqiang Lu, Nanchang Hangkong University, China

Prof. Wenlei Sun, Xinjiang University, China

Prof. Jun Wang, Northeastern University, China

Prof. Chunliang Zhang, Guangzhou University, China

Prof. Qiang Wang, Jinan University, China|

Prof. Jialu Li, Tianjin Polytechnic University, China

Prof. Sihai Jiao, Research Institute, Baosteel, China

Prof. Zhengyi Jiang, University of Wollongong, AU

Prof. Niels Bay, University of Denmark, Denmark

Prof. Viktor P. Astakhov,General Motor Business Unit of PSMi, Mi,USA

Prof. Jian Cao, Northwestern University, USA

Prof. Cesar de Sa, Jose, University of Porto, Portugal

Prof. Christian Kloc, Nanyang Technological University, Singapore

Prof. Cheng Kai, Brunel Univeristy, UK

Prof. Yusuf Altintas, University of British Columbia, Vancouver, Canada

Prof. Phil Koshy, Mcmaster University, Hamilton, Ontario, Canada

Prof. Kambakar P Rajurka University of Nebraska-Lincoln, USA

Prof. Nabil Gindy, University of Nottingham, UK

Prof. V.K.Jain, Indian Institute of Technology, Kanpur,UP, India

Prof. Walid Mahmoud Shewakh, Beni Suef university, Egypt

Prof. Yun-Hae Kim, Korea Maritime University, Korea

Prof. Carlos Caceres, The University of Queensland, Australia

Prof. Shahrum Abdullah, University Kebangsaan Malaysia, Malaysia

Dr. Xiangping Bu, Wayne State University, USA

Prof. Sagar Kamarthi, Northeastern University, USA

Prof. Heinz-Gunter, Brokmeier, Technische Universitat Clausthal, Germany

Prof. Toshio Haga, Osaka Institute of Technology, Japan

Prof. Jia-Horng Lin, Feng Chia University, Taiwan

Prof. Jong Kook Lee, Chosun University, Korea

Prof. Junan Shen, Georgia Southern University, USA

Prof. Jiwei Cai, Hebei United University, China

Local Organizing Committee

Chair

Prof. Jian Gao, Guangdong University of Technology

Co-Chairs

Prof. W. B. Lee, Hong Kong Polytechnic University, Hong Kong

Prof. Zhongning Guo, Guangdong University of Technology, China

Technical and Organizing Committee

Prof. Chengyong Wang, Guangdong University of Technology, China

Prof. Naiqi Wu, Guangdong University of Technology, China

Prof. Xindu Chen, Guangdong University of Technology, China

Prof. Hanwu He, Guangdong University of Technology, China

Prof. Qiusheng Yan, Guangdong University of Technology, China

Prof. Xin Wei, Guangdong University of Technology, China

Prof. Xiangdong Gao, Guangdong University of Technology, China

Prof. Qingxin Chen, Guangdong University of Technology, China

Prof. Xiao Li, Guangdong University of Technology, China

Prof. Ping Zhang, Guangdong University of Technology, China

Prof. Ketian Li, Guangdong University of Technology, China

Prof. Qiang Liu, Guangdong University of Technology, China

Prof. Ping Ma, Guangdong University of Technology, China

Prof. Siyuan Cheng, Guangdong University of Technology, China

Prof. Qingke Yuan, Guangdong University of Technology, China

Prof. Yousong Sun, Guangdong University of Technology, China

Prof. Haiyan Zhang, Guangdong University of Technology, China

Prof. Xiaohua Jie, Guangdong University of Technology, China

Secretary

Dr. Yixiang Zhao, Guangdong University of Technology, China

Dr. Yan Bu, Guangdong University of Technology, China

Dr. Yinhui An, Guangdong University of Technology, China

Dr. Qiang Liu, Guangdong University of Technology, China

Dr. Mark Fong, Hong Kong Industrial Technology Research Centre

Table of Contents

Modeling, Analysis and Simulation of Manufacturing Processes

Materials Processing Technology

Mechanical Behavior & Fracture

Material Design of Computer Aided

Tooling/Testing and Evaluation of Materials

Thermal Engineering Theory and Applications

CAM/CAE

High-Speed/Precision Machining and Inspection Technology

Micro-Machining Technology

Laser Processing Technology

Bionic Mechanisms and Bio-Manufacturing

Digital Manufacture and Management

The Internet of Things

Other Related Topics

Surface Engineering/Coatings

Advanced Materials Research Vols. 314-316 (2011) pp 3-9

doi:10.4028/www.scientific.net/AMR.314-316.3

Experimental Study on Laser Surface Cladding of Ni60 alloy on AZ31B Magnesium Alloy

Yaqiong Ge[1, a], Wenxian Wang[2,3,b]

[1] College of Materials Science and Engineering, Taiyuan University of Science and Technology, Taiyuan, 030024, China

[2] College of Materials Science and Engineering, Taiyuan University of Technology, Taiyuan, 030024, China

[3] Key Laboratory of Interface Science and Engineering in Advanced Materials of Taiyuan University of Technology Ministry of Education, Taiyuan, 030024, China

[a]joan1028@163.com, [b]wwx960@126.com

Keywords: AZ31B magnesium alloy, Ni60 laser cladded layer, Microhardness, Wear resistance, Corrosion resistance

Abstract: In order to improve the corrosion and wear resistance of AZ31B magnesium alloy, Ni alloy cladding layer which had no crack and hole on AZ31B magnesium substrate was created by a 5kW continuous wave CO_2 laser. The microstructure was analysed by means of OM(Optical Microscope) and XRD(X-ray Diffraction), the electrochemical corrosion and the abrasion performance were also tested by electrochemical corrosion equipment and the abrasion testing machine. The results show that: the Ni alloy cladding layer can combine with the substrate metallargically, the microstructure of cladding layer is dendritic crystal, and becomes fine significantly from the interface to surface, and the phase of the cladding layer are $MgNi_2$, Mg_2Ni, Mg_2Ni_3Si, Mg_2Si and FeNi. Micro-hardness of the cladding layer is 470~601HV which is improved 840%~1102% to the substrate(40~50HV). Average friction coefficient of the cladding layer is 0.321 lower than AZ31B substrate, and the wear mass loss is 91.43% less than the substrate, the wear resistance of the cladded layer has been improved observably. The corrosion voltage of cladding layer moves 136~417mV to plus direction compared to AZ31B magnesium substrate, and the corrosion current of the cladding is 2~3 stages lower.

Introduction

Owing to the advantages of low density, rich in natural resources, free-pollution, recirculation, high specific rigidity and strength and well thermal conduction etc., magnesium alloy become the third largest metallic engineering materials after steel and aluminum materials, and is titled as 'the new-style and green industry structure materials' for the 21st century[1,2]. Unfortunately, magnesium alloys could not yet be accepted widely in many applications due to their inferior hardness, wear and corrosion properties[3]. Therefore, Surface treatment technologies of magnesium alloys have attracted many researchers.

With the well-known infiltration, corrosion resistance, wear resistance, self-lubrication under high temperature and moderate price [4], Ni alloy powder is the most extensive used cladded materials.

In the paper, a detailed investigation had been undertaken on laser clad Ni60 alloy on AZ31B magnesium alloy by a 5kW CW CO_2 laser. The microstructure and properties of the caldded layer were researched.

Experimental materials and procedures

Experimental materials. In the present investigation, hot-rolling AZ31B magnesium alloy was chosen as the substrate material. And its composition is listed in Table 1. The dimension of specimen is 200mm×50mm×10mm.

Table 1 Chemical composition of AZ31B (wt.%)

Al	Mn	Zn	Ca	Si	Cu	Ni	Fe	Other	Mg
2.5~3.5	0.2~1.0	0.6~1.4	0.04	0.10	0.01	0.001	0.005	0.30	Bal.

Ni60 self-fluxing alloy powder was used as the cladded material. And its composition is listed in Table 2, its graininess is 250 sieve.

Table 2 Chemical composition of Ni60 (wt.%)

Ni	Cr	B	Si	Fe	C
Bal.	16	3.5	4.5	≤15	0.8

Experimental procedures. Before laser cladding, the substrate was needed to be pretreated. First of all, rubbed it with 80# sandpaper to wipe off the surface oxide and greasy dirt. Secondly, washed it by acetone, then aired dry. Finally, coated the uniform preset Ni60 alloy powder which was mixed with cellulose binder to the surface of the substrate, aired dried again until the Ni60 powder was dry and combined with the substrate's surface strongly.

Laser surface cladding was carried out by a 5 kW CW CO_2 laser with 10.6μm wavelength. The specimens were placed on a work plat and the laser was controlled with a computer-controlled XY stage. The specimens were melted using a constant laser power of 3kW as a heat-generating source for producing and the laser beam moved at a speed of 180mm/min with a circle laser beam of 5mm dimensions. The laser melt pool was shrouded by pure 99.99% argon gas with a flow rate of 20 L/min to prevent excessive oxidation of the substrate. While it was need to lap the path, the overlap was 20% of one path, which was controlled by a computer. After one path was cladded, the next path would be cladded till the temperature was down to room temperature. Fig.1 is the schematic diagram.

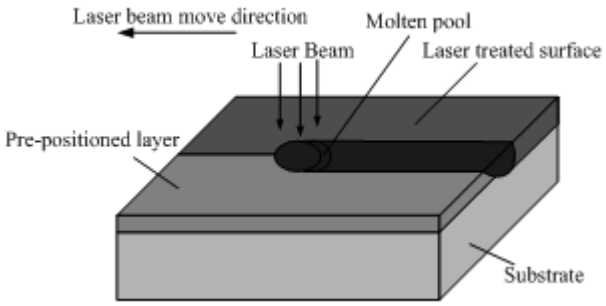

Fig.1 Sketch map of laser cladding

The laser caldded sample was cut along transverse section, then polished and etched. The microstructure of the cross-section of the laser cladded layer was observed by CMM-20 OM and JSM-6700F SEM (Scanning Electron Microscope). The phase compositions were analyzed by Y-2000 XRD. Micro-hardness of laser cladded layer and the substrate were measured by a HVS-1000A Vickers microhardness tester with a 200mg applied load and a 15s applied time. Abrasion performance was tested by a MS-T3000 friction wear testing machine, and the dimensions of wearing part was 15mm, the spherical GCr15 used as grinding material, with a 20min scraped time and 200r/m rotated speed and 500g applied load. Corrosion resistance of the samples surface before and after laser surface cladded were studied in a 3.5% NaCl solution by a PS-168A electronic-chemical measure system.

Results and discussions

Microstructure. The macrostructure of laser cladded Ni60 alloy layer on AZ31B magnesium alloy is shown in Fig.2. Though the melting point of Ni alloy is higher than of Mg alloy, the Ni60 alloy integrats well to the substrate because of its good self-fluxing nature and wetting property, and the physico-chemical consistency of them. It showed in Fig.2(a) that the cladded layer has no defects such as cracks and holes etc. A part of the cladded layer were analysed with EDS, and the results are listed in Table3. The composition of AZ31B substrate (A zone of Fig.2(b)) is Mg, of heat affected zone which is the melted zone of substrate (B zone) are Mg mainly and a little O, it is because that the test circumstance was not vacuum but Ar, the specimen was oxidized slightly. The composition of integrated zone(C and D) are Mg and Ni, there will be Mg/Ni compound according to the Mg-Ni binary phase diagram. Melted Ni60 powder forms the cladded layer, a little melted Mg of substrate enters the molten pool due to pool's convection , there will be multiform Mg/Ni/Fe/Si intermetallic compound.

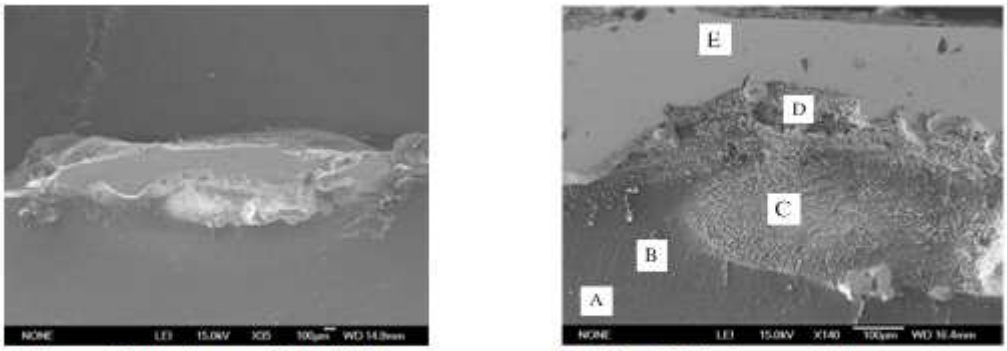

(a) Min-multiple picture of cladded layer (b) Magnified picture of picture (a)

Fig.2 Macrostructure of laser cladded Ni60 alloy layer on AZ31B magnesium alloy

Table 3 Chemical composition of cladded layer and substrate (%)

Element		zone A	B	C	D	E
Mg	Weight%	100.00	92.53	48.23	8.94	2.59
	Atomic%	100.00	89.07	51.66	13.43	3.67
O	Weight%	——	7.47	21.43	14.88	——
	Atomic%	——	10.93	34.88	33.94	——
C	Weight%	——	——	——	——	15.74
	Atomic%	——	——	——	——	45.12
Si	Weight%	——	——	——	7.24	3.78
	Atomic%	——	——	——	9.40	4.64
Ni	Weight%	——	——	30.34	57.34	48.02
	Atomic%	——	——	13.46	35.65	28.16
Fe	Weight%	——	——	——	11.61	29.86
	Atomic%	——	——	——	7.59	18.40

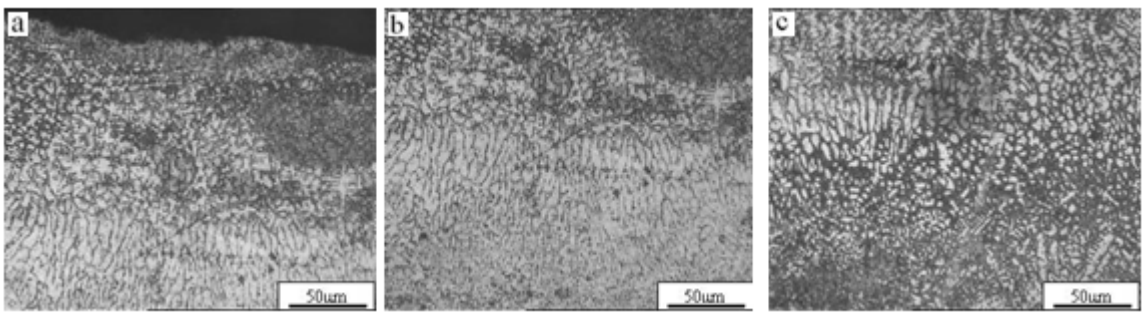

(a)Top of cladding layer (b) Middle of cladding layer (c) Bottom of cladding layer

Fig.3 Microstructure of laser cladded Ni60 alloy layer on AZ31B magnesium

The microstructure of the laser cladded Ni60 layer is shown in Fig.3. During the laser cladding procedure, as solidify, the G/R decreases, and dendritic crystals along with heat flow's direction are generated. In the integrated zone(c of the Fig.4), because of increased Mg and diffused Ni , there is a concurrent zone of α-Mg and intermetallic compound. There are minute dendritic crystals which show directivity with the changes of heat flow in t he middle of the cladded layer (b of the Fig.3). More minute dendritic crystals are in the upper part of the caldded layer (a of the Fig.3).

X-ray diffraction. X-ray diffraction pattern for laser cladded Ni60 layer is shown in Fig.4. It could be seen that the cladded layer is consisted of Mg, $MgNi_2$, Mg_2Ni_3Si, Mg_2Ni, Mg_2Si and FeNi. Compared to Ni alloy, the melting point of magnesium is lower, and specific density of them is different greatly, in the cladding process, there is obvious pool convection. A part of laser's energy is used to melt the Ni60 alloy powder, at the same time, part of the heat quantity is transferred to AZ31B substrate by Ni60 alloy powder, the molten pool is generated by melted the surface of the substrate, Mg in the bottom of the pool diffuses to the whole pool for mass transferred. At the meantime, Mg and many intermetallic compounds generate because of the different melting point of Mg and Ni, and the variant combining degree of Mg and Ni, Fe and Si etc. in Ni60 alloy powder.

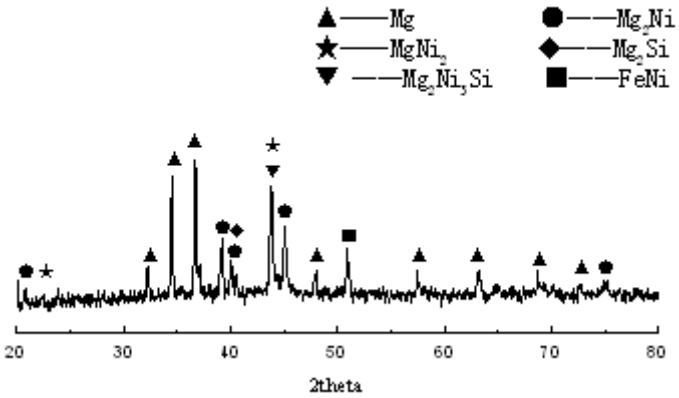

Fig.4 XRD of the laser cladding Ni60 alloy layer

Microhardness. The microhardness of the melted layer is measured from the surface-edge towards the melted pool-substrate interface along the cross-sectional plane, and it is showed in Fig.5. It is clear that the microhardness of the cladded layer's surface is descent because some alloy element is burning lost. At 0.1mm to 0.4mm zone of the subsurface, the microhardness is uniform, as the distance to the surface increases , the microhardness descends to that of AZ31B substrate. The microhardness of the caldded layer has significantly increased by about 840%~1102%(470~601HV) as compared to that of the substrate(40~50HV).This improvement in microhardness may be attributed to refined grain and many various intermetallic compounds.

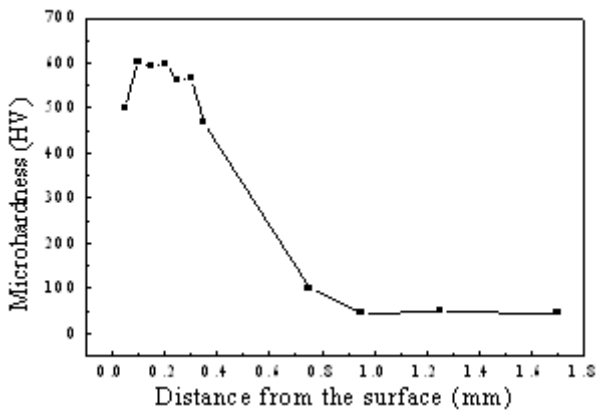

Fig.5 Microhardness of laser cladded Ni60 alloy layer on AZ31B magnesium alloy

Wear resistance. The worn morphology of AZ31B alloy and laser cladded layer is shown in Fig.6. There are grooves which are the characters of grain-abrasion, but the grooves of Ni60 cladded layer are shallow and fine to as-received magnesium, so it can be inferred that the wear resistance of cladded layer is higher. For one thing, grooves are generated by free abrasive dust in fricting course and grindings in the subsequent. For another thing, the microhardness of Ni60 cladded layer is higher than the as-received magnesium, so the difference of mirohardness between cladded layer and grinding material is less.

Friction coefficient for laser cladded layer and the as-received magnesium are shown in Fig.7 and Fig.8. The friction coefficient of as-received fluctuated greater, it is illustrates that there are more adhesion on the surface. However, the curve of the cladded is flatter. At the beginning of wearing(0~1min), the friction coefficient rises to about 0.3 gradually, as the time progressed, it is about 0.3 steadyly. The maximum and the average friction coefficient of as-received magnesium are 0.961 and 0.578, but them of the caldded are 0.422 and 0.257. Then, the wear mass loss of as-received and cladded layer are also been weighed, they are 3.5×10^{-3}g and 0.3×10^{-3}g. It is proved that the wear resistance of cladded has been improved observably.

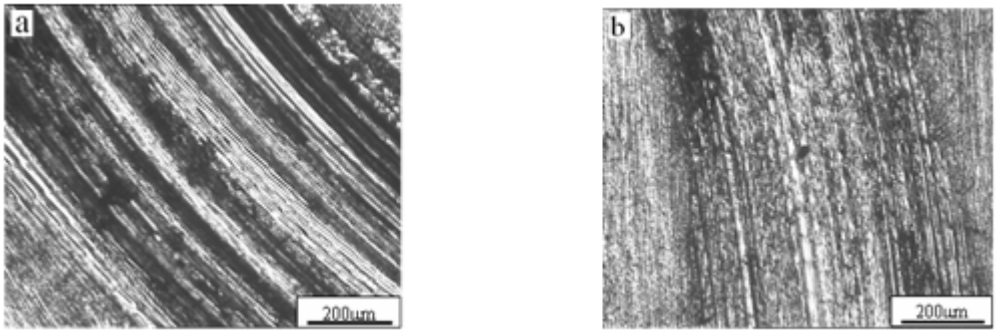

Fig.6 Worn morphologies of as-received AZ31B alloy (a) and laser cladded Ni60 alloy layer(b)

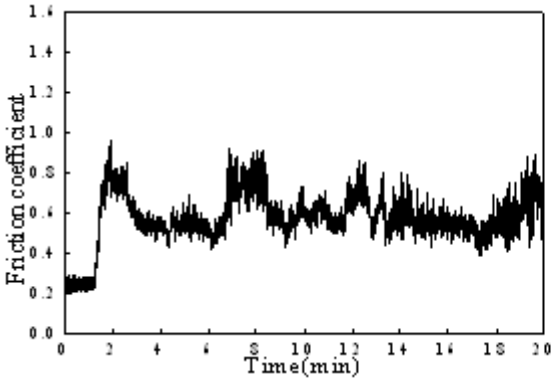

Fig. 7 Friction coefficient of as-received AZ31B

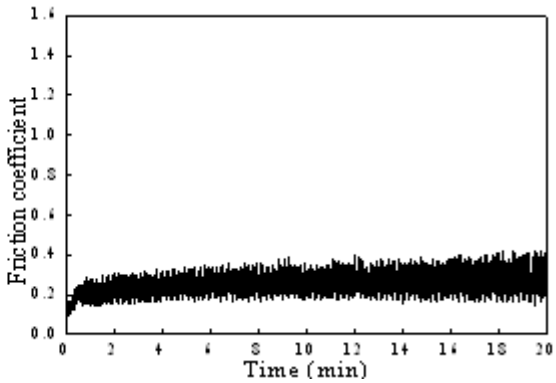

Fig. 8 Friction coefficient of Ni60 cladded layer

- **Corrosion resistance.** Fig.9 displays the potentiodynamic anode polarization curves of the cladded layer as well as as-received magnesium alloy. Compared with the as-received magnesium alloy, the corrosion potential (E_{corr})of cladded layer is increased by 251 mV, and the corrosion current (I_{corr})of cladded layer is reduced 2~3 order of magnitude. So, the corrosion resistance of laser melting layer is better than that of the as-received Mg alloy. Firstly, the grains of the cladded layer are finer. Secondly, there exist many Ni, Ni-Mg compounds in cladded layer.

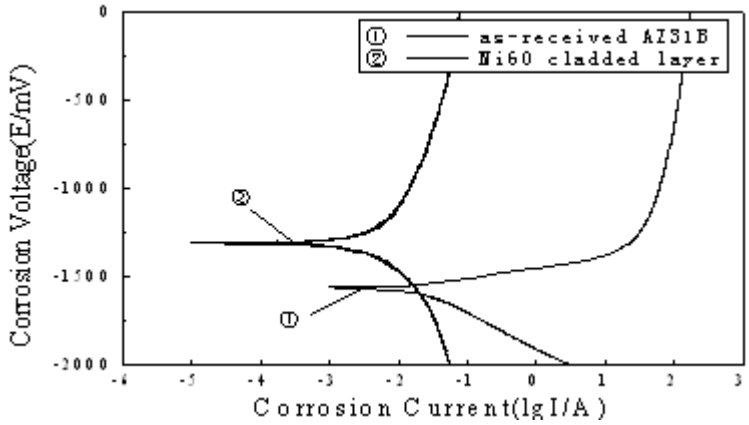

Fig.9 Potentiodynamic polarization curves of as-received AZ31B and Ni60 alloy cladded layer

On the basis of electrochemical corrosion principle, under the effect of electrochemical corrosion, corrosion rate is the varying mass at unit time and on the unit area. Therefore, the corrosion rate is:

$$v = \frac{M}{S\tau} = KI \tag{1}$$

The corrosion rate is direct ratio to current density. So, under the corrosion system, the dynamics resistance force enlarges [5]. Besides, there is no obvious passivating zone, passivating performance is obscure. It is because that different alloy layer integrats to substrate's surface, and more compounds exist in the cladded layer, it is difficult to generate passivating film. However, the corrosion resistance has been improved.

Conclusions

(1) The Ni60 alloy cladded layer was prepared on the surface of AZ31B by laser cladding, the caldded layer integrates well to the substrate, and there are no defects in the cladded layer.

(2) The phase of the cladding layer are Mg and intermetallic compounds $MgNi_2$, Mg_2Ni, Mg_2Ni_3Si, Mg_2Si and FeNi, the microstructures present the typical dendritic crystals of Ni alloy.

(3) Micro-hardness of the cladding layer is 470~601HVwhich is improved 840%~1102% to the substrate(40~50HV). Average friction coefficient of the cladding layer is 0.321 lower than AZ31B substrate, and the wear mass loss is 91.43% less than the substrate, the wear resistance of the cladded layer has been improved observably.

(4) The corrosion voltage of cladding layer is -1308mV, which moves 251mV to plus direction compared to AZ31B magnesium substrate(-1559 mV), and the corrosion current of the cladding is reduced 2~3 order of magnitude to the substrate.

Acknowledgements

This work was financially supported by the National Natural Science Foundation of China (51075293), Young Foundation of Taiyuan University of Science and Technology (20103008) and UIT of Taiyuan University of Science and Technology (XJ2010021).

References

[1] W.X Li: *Magnesium and Magnesium Alloy.* (Central South University Publications, China 2005) (In Chinese)

[2] Z.Liu, K.Zhang, X.Q.Zeng: *Theory and Application of magnesium lightweight alloy*.(China Machine Press, China 2002) (In Chinese)

[3] B.Gao, S.Z.Hao, J.X.Zou et.al. Journal of Surface & Coatings Technology, Vol. 201(2007), p. 6297-6303

[4] G.S.Zhang: *Modern laser manufacturing engineering.*(Chemical Industry Press, China 2006) (In Chinese)

[5] C.H.Zhang, S.Zhang. Journal of Rare Metal Materials and Engineering, Vol. 34(2005), p.701-704(In Chinese)

Advanced Materials Research Vols. 314-316 (2011) pp 10-16

doi:10.4028/www.scientific.net/AMR.314-316.10

Transparent Glass Window with Energy-saving and Heat Insulation Capabilities

Ching-Mu Chen[1,a],Shen-Yuar Chen[2,b],Wei-Ching Chuang[2,c] and Jen-Yu Shieh[2,d]

[1]No. 6, Lane 2, Sec. 3, Shanjiao Rd., Yuanlin Township, Changhua County, Taiwan
[2]No.64, Wunhua Rd., Huwei Township, Yunlin County, Taiwan
[a]kchen@dragon.ccut.edu.tw, [b]yaur@nfu.edu.tw, [c]eocwc@nfu.edu.tw, [d]reed@nfu.edu.tw

Keywords: Infrared light, coating technology, energy-saving, carbon reduction, heat insulation.
Abstract. This paper proposes capabilities of transparent glass window design with energy-saving and heat insulation for carbon reduction issues. An optical thin film coating technology is used for coating multilayered dielectric materials on the transparent glass to achieve an infrared ray shielding effect; especially to prevent rising temperature easily of indoor room. That is infrared ray incidence from outdoor and the thermal flux effect of the transparent window influent the indoor room temperature. In winter, the outdoor temperature is increased more easily by infrared ray incidence. However, the heat insulation window allows 98% of visible light penetration through the window and also allows 90% of infrared light reflection and roughly 10% of infrared light penetration into indoor.

Introduction

The glass is an important building material and has been used increasingly in industry because of the growing demands and decoration purposes. With taking aesthetic and appearance characteristics of glass into consideration, people are also paying more attention on its abilities of control heat and cooling costs as well as sunlight projection. Therefore, Low-E Glass with coated glass category is getting popular.

Low-E Glass is known as low emissive glass derived from coating multilayer of metallic films or other compounds on a glass surface to form a coated product [1]-[3]. In this paper, the coated layer has many characteristics such as high visible light penetration, high reflection of mid-infrared ray and so on. Also, it features the following significant merits when compared to the common glasses and conventional architectural coated glasses.

Excellent thermal performance: The transmittance of exterior door and window is related to the thermal conduction of buildings more than 50% of its energy consumption. Relevant studies indicated that heat conduction at the inner surface of glass is dominated by radiation up to 58% of overall heat consumption. This means that the most effective way to inhibit radiation at the inner surface of glass is to change the glass performance to reduce the heat conduction of heat energy. The emissive ordinary float glass is about 0.84 which can be down to 0.1 when coated with a low emissive film of multilayer dielectric materials. Therefore, the usage of glass door and window proposed in this paper is able to prevent the indoor heat energy and achieve an ideal energy saving effect.

A reduction of indoor temperature around 1℃~3℃ is able to reduce the usage of air conditioning in summer time and bring with issue of the significant environmental protection benefit. During the cold season time, the most important pollution is CO2 and SO2 gas emissions caused by heating building. However, the goal of this paper is especially for the energy-saving and heat insulation glass and then it can significantly reduce fuel consumption in heating due to a reduction in heat loss, and thereby lowering harmful gas emissions.

Good optical properties: This paper can also down more than 80% about the usage on visible sunlight and its reflectivity is very low. The optical performance can thus be improved remarkably compared with conventional coated glasses. When looking from outside, it has a high transparency

and clarity appearance to ensure good daylight in the building; at the same time, avoiding light reflection caused by hollow glass window and door in conventional glass curtain walls to result in light pollution phenomenon, and able to create a softer and more comfortable environment.

The aforesaid characteristics of Low-E Glass have been prompted to be used widely day by day in the developed countries. As Taiwan towards a relatively energy-poverty country with low energy consumption, architectural energy consumption has already taken some 27.5% of the country's total energy consumption. If the production technique of Low-E Glass can be developed extensively and actively, it would definitely bring in significant social and economic benefits to the country.

Definition and types of Low-E Glass

The glass with high transparency, low glare and high radiation shielding effects is known as Low Emissivity Glass, or Low-E Glass. In other words, the reflective glass with high glare rate is known as high emissive glass. The current Low-E glass can be classified into three categories [4]-[6].

Hard Low-E Glass: The glass can be made of single, laminated, or multi-layered combination glass sheet, and it can be high-temperature reinforced directly or curve-processed to ease applications. The flaw is a slightly poor heat insulation effect and suitable to use in cold regions to prevent heat loss and keep warm in buildings.

Soft Low-E Glass: The excellent heat insulation effect has made it ideal to be used in tropical regions. However, its metallic coating is unable to resist high temperature and tends to oxidize after being long-term exposure in air. Therefore, it is suitable to be made as flat multi-layered glass.

PET Low-E Glass: Thin film, PET Low-E Film, can be applied as single, laminated, and multi-layered combination glass sheets. Excellent heat insulation such as UV resistant and sound insulation performances is capable of keeping warm in winter and cool in summer so that it is suitable to use both tropical and cold regions.

Coating principles and methods

Basic coating principles: The general metallic reflective film is simple manufacturing equipment and technology in production its disadvantages are high optical loss and a possible high reflectivity. An increase in reflectivity is adversely lower the transmittance to affect the image quality. Most importantly, the metallic film such as gold, silver, chrome and aluminum has a high absorption band on infrared ray causing the infrared ray unable or difficult to pass through the metallic-coated heat insulation glass window to result in high infrared ray absorption. Therefore, it is ineffective to insulate against infrared heat.

The heat insulation coated window is made up of a sheet of transparent substratum coated with a layer of dielectric in two different wave fields for the penetration of visible light and infrared ray. The visible light wave field is a spectral area of high penetration and low reflectance. The infrared wave field is a spectral area of high reflection and low penetration ratio. For example, after a 100% incidence ray has struck on the coating material, there is 98% penetration of visible light to form a high transmission rate, 90% reflectivity of infrared ray, meaning 90% of infrared ray reflection from the material and 10% of infrared ray penetration. Therefore, the optical divide ratio of high reflection and low penetration is 90:10. In general, the loss such as absorption from the coated substrate and coating materials on light is relatively small and this loss of light is neglected. The simple calculation is 100% that is infrared light is equal to 90% reflection plus 10% penetration as shown in Fig. 1.

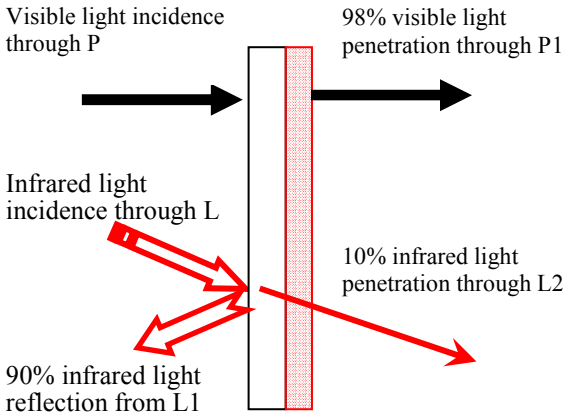

Fig. 1 90% reflection and 10% penetration of incidence light

Physical Vapor Deposition (PVD): Fig. 2 is a schematic diagram of physical vapor deposition which involves a high-energy electron beam to bombard on the coating material and convert it into heat energy with a temperature as high as several thousand degree Celsius. Therefore, it will evaporate the coating material into vapor to penetrate through the vacuum and deposit it on top of the glass substrate.

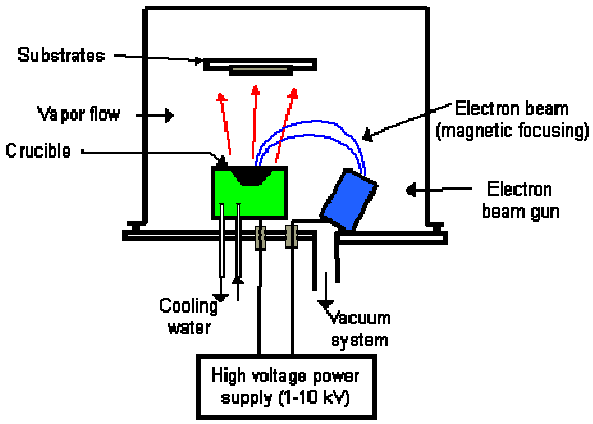

Fig. 2 Schematic diagram of physical vapor deposition

The infrared wave field is a reflective area of high reflectance ratio. For instance, the reflectivity on infrared ray is higher than 90%. Two coating materials are used alternatively as the dielectric membranes in the vapor deposition process for the substrate, namely titanium oxide (TiO2 of refractive index 2.2) and silicon dioxide (SiO2 of refractive index 1.54).

The process involves an alternative vapor deposition method coating 1~3mm for TiO2 and SiO2 of that is different refractive indexes on the transparent glass. This utilizes a multi-layered coating to reflect 90% of infrared ray and penetration of 10% infrared light and 98% visible light. In Fig. 1, L refers to the infrared ray incidence, L1 to the infrared ray reflection, L2 to the infrared ray penetration, and P1 to the visible light penetration.

A piece of coated sample is made during the experiment. The main parameters of the spectra are the follows: The y-coordinate refers to the transmittance T% and the x-coordinate is the spectrum wavelength (nm) that is about the white light environment, the positive incidence angle (0 degree), the reference wavelength of 450nm, and a quarter wavelength.

In thin film optics, it is easily to obtain the predicted transmittance T% from vector or admittance diagram method through multi-layered coating with a high refractive index on the quarter-wave stack of the optical-grade substrate. Theoretically, the reflectivity obtained from quarter-wave stack is

much higher than non-quarter-wave stack when a similar multi-layered coating is used. The greater the coating layers, the greater will be the reflectivity R%. However, it is easily to control the proportion of penetration and reflection. In the current existing coating materials, the high reflectivity in visible light area is smaller or equal to 2.4 and the low reflectivity is greater than or equal to 1.35. Therefore, the high reflective band width of single quarter-wave stack is limited.

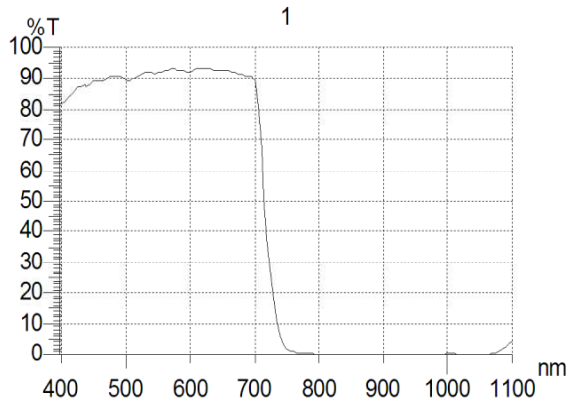

Fig. 3 The spectrogram of the coated sample

The widening method: According to geometric progression or arithmetic progression, the widening method is to regularly increase the concentration in every layer of coating progressively. Any wavelength within the wide area is covered with an adequate coating and its optical concentration is also sufficient to approach the quarter-wave. However, the reflectivity generated from this high reflective area will come with many descending ripples and must be optimized using the optimization method. Another option is to overlay the quarter-wave stack with a shorter central wavelength on another quarter-wave stack. Basically, the coating design can be started from standard coating system. In the case of a high reflective mirror, it can be designed from fundamental quarter-wave stack regardless of the size of pulse width, single or double wave number. If the initial design is unable to meet the requirement of optical performance, using the current commercial computer software design can optimize or synthesize it.

By optical thin film interference phenomenon, when light enters the single-layered coating in vertical incidence, the optical thickness Nd (multiplication of thin film refractive index and thin film thickness) is λ0/2, λ0, 3λ0/2 and so on. The reflective strength of the coating on wavelength will remain unchanged. If the optical thickness Nd is λ0/4, 3λ0/4, 5λ0/4 and so on, the reflectivity will come in maximum value or minimum value and its value is determined by whether the coating's refractive index n is greater or smaller than the reflectivity ns of the substrate. If n>nS, the reflectivity will become maximum value and if n>nS, the reflectivity become minimum value. In Fig. 4, a layer of optical thickness in 1/4 odd number multiplication of incidence light is allowed to form destructive interference for the reflected wave. Then, the anti-reflection effect of reflectivity is zero. However, the reflectivity on other wavelengths will not be zero. In order to obtain a wide reflectivity of the visible light scope, the multi-layered structure is prevailing. An appropriate selection of film refractive index and coating design is able to help us obtain a proper reflectivity as shown in Fig. 4.

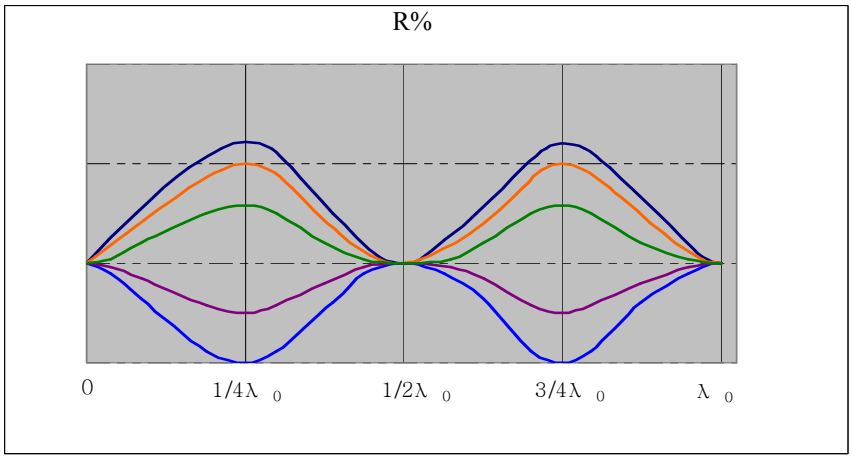

Fig. 4 Interference phenomenon in optical thin film

Transparent substrate: The transparent substrate can generally be classified into two categories that are optical-grade transparent glass and transparent resin. The transparent substrate must come with a high level of transparency, a strict surface requirement, no speckles and stripes, air pores, whitening, fogginess, black spots, discoloration, roughness, poor luster and other defects. The transparency of visible light and infrared ray on the transparent substrate is also affected by light reflection, penetration, absorption, scattering and other factors. The light scattering and absorption phenomena caused by light incidence on the optical-grade transparent substrate are negligible compared to metallic coating. In industrial plastics, the transparent resins with a high transparency includes PMMA (transparency of roughly 93%), PC (transparency of roughly 88%), PS (transparency of roughly 89%), CR-39 (transparency of roughly 90%), SAN resin (transparency of roughly 90%), MS resin (transparency of roughly 90%), and TPX (transparency of roughly greater than 90%). In addition, the transparency of polyethylene ether, styrene copolymer (MAS), PET, PP and PVC, etc. is also impressive.

When light enters the transparent resin, it will get lost through surface reflection. Reflection is normally calculated from surface reflectivity R% through the polymer where n1=1 and refers to the refractive index. n2 as the refractive index arises from vertical light incidence in the air and is represented by (n-1)2 divided by (n+1)2. Data from manufactures indicate that the refractive index of transparent acrylic (Polymethyl methacrylate or PMMA) is 1.49, and the surface refractive index R% can be calculated as roughly 4%. The full transmittance of PMMA is roughly 93%. The loss of light on this material is mostly caused by secondary reflection on the surface. The interior loss through light absorption and scattering is then negligible.

When light enters the transparent resin molecules, the molecules will absorb the light energy and generate a rotary motion to lead the light absorption and lower the transmittance. During light absorption, the scattering light generated simultaneously will also significantly reduce the transmittance. As the scattering rate at transparent resin interior is directly proportional to the power of eight of reflective index and inversely proportional to the power of four of wavelength; therefore, the light scattering loss on material with a low reflective index is small and the effect of light scattering on visible light area of longer wavelength is also small. In the infrared domain of longer wavelength, the impact on light scattering is almost equal to zero. PMMA is a non-crystalline (amorphous) material where the high polymer chains are arranged in chaotic and tangling manner rather than in an orderly arrayed structure. During the course of solidification, there is no occurrence of nucleation and growth processes, only a frozen phenomenon of free high polymer chains and giving rise to its high transparency appearance. Non-crystallized plastic polymer features a low material density to result with a good transmission; whereas, due to different refractive indexes of spherulite and the irregular area of crystallized polymer, its material density is greater to result with a poorer transmittance, and thus not suitable to use in this thesis. The good workability of PMMA sheet has made it easy to be thermo-formed (including mold pressing, blow molding and vacuum forming)

in any shapes and mechanical processed such as turning, drilling, cutting and so on. Not only can the use of microcomputer-controlled machinery be able to improve the processing accuracy of cutting and engraving significantly, it can also produce complicated shapes and patterns that cannot be accomplished by conventional processing methods.

The coating method adopted in this paper is vacuum vapor deposition where the heat resistance of transparent glass is 300℃. PC and PMMA is about 130℃ and 70℃, respectively. Among them, PMMA is much difficult in the cold treatment process because high temperature would result in deformation, and cold temperature would result in poor adhesion of coating.

Experimental results

Fig. 5 is the scaled down version of energy-saving experimental model and four coated glass are sealed with silicon. The glass on the left is multi-layer coated with dielectric coating material compared to the non-coated control model on the right. The left model is the infrared ray reflection and shields the most of the heat source while the temperature on the right model would rise over the time. Based on the comparison of using the 100W bulb for 15 minutes duration, there is a temperature variance of about 10℃. Fig. 6 is the side view of the scaled down experimental models with energy-saving windows. Fig. 7 is a comparison chart to simulate 100W bulb irradiation for 16 minutes duration. Serial 1 represents the experimental results of glass with special coating material. Serial 2 represents the non-coated control group. It is found after 16 minutes of irradiation; there is a temperature variance of about 10℃.

Fig. 5 Simulated energy-saving windows

Fig. 6 Simulated energy-saving windows

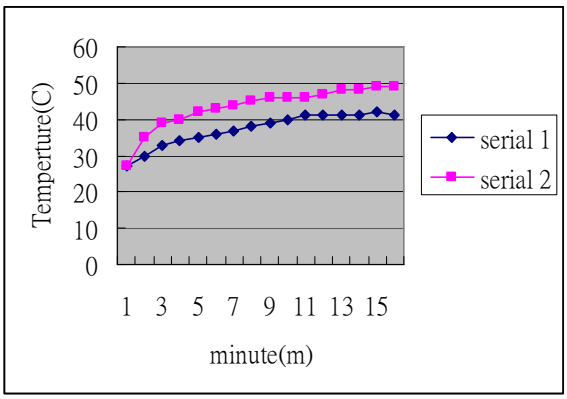

Fig. 7 Comparison chart about 100W bulb irradiation for 16 minutes duration

Conclusions

The current existing heat insulation papers or films tend to generate a mutual contradiction between transmittance and heat insulation performances. The higher the transmittance of visible light, the lower of the heat insulation effect is; in particularly for models coated or incorporated with metallic content. As the coating technology is adopted by this proposed paper and utilized the alternative evaporation of semiconductor materials on the heat insulation glass window, its visible light transmittance is able to reach as high as 98%, and capable of shielding 90% of near-infrared light and allowing 10% of infrared light penetration.

Acknowledgements

This work was financially supported by the National Science Council (982622E150090CC3) and Night-Hawk Optic-Electronics Co., Ltd. With National Formosa University for granting us the subsidies in 2010 Excellence in Teaching Project, giving us the opportunity to present this work in 2010 Invention and New Product Exposition (INPEX) at Pittsburgh and win a Gold Medal, and a Silver Medal in 2010 Taipei International Invention Show and Techno mart. Meanwhile, we would also like to thank the assistance given by graduate students Chi-Ming Lin and Jun-Ming Chang for making this entity model so incredibly persuasive.

References

[1] D.L. Blackshear, U.S. Patent 3,819,856. (1974)

[2] G. Behles, U.S. Patent 3,739,703. (1973)

[3] M. Tovi, U.S. Patent 4,225,811. (1980)

[4] B. Gompf, J. Beister, T. Brandt, J. Pflaum, and M. Dressel: Optics Letters, Vol. 32, Issue 11 (2007), pp. 1578-1580.

[5] J.H. Liu, “Investigation of Functional Coatings on PI Substrates for Flexible Display Applications,” Graduate Institute of Optoelectronic Engr., National Chung Hsing University, Master Thesis. (2009)

[6] J.H. Liu, “Investigation of Functional Coatings on PI Substrates for Flexible Display Applications,” Graduate Institute of Optoelectronic Engr., National Chung Hsing University, Master Thesis. (2009)

Advanced Materials Research Vols. 314-316 (2011) pp 17-22

doi:10.4028/www.scientific.net/AMR.314-316.17

Development and Experiment of Surface Engineering Technology on Mulberry Silk Brocade Fabrics

Shichao Li[1,a], Changbo Tang[1,b], Xuan Wang [2,C], Jianping Shi[2,d*]

[1]Silk Applied Technology Research Institute of Suzhou Vocational University, Suzhou, Jiangsu 215104, China

[2]College of Textile and Clothing Engineering, Soochow University, Suzhou, Jiangsu 215021, China

[a]shichao-66@163.com, [b]tangcb@jssvc.edu.cn, [c]wangxuan3220@yahoo.com.cn,
[d] Corresponding author: shijp88@163.com

Keywords: Surface Engineering; Mulberry Silk Brocade Fabrics; Anti-aging Antibacterial Mold

Abstract. Exploring and using surface engineering technology into the Anti-aging antibacterial mold of mulberry silk brocade fabrics through multiple dipping and padding to carry out limited permeation and effective bonding strength on material surface. It has obvious effect on antibiotic action and less effect on the silk materials' original performance.

Introduction

Surface engineering technology is system engineering. In order to acquire the material surface performance needed, it uses a composite processing way to transform superficial configuration, chemical composition and organizational structure or stress condition of material. The way contains superficial coating, modification and other various surface technologies. Among them, the treated materials are mainly metals and also some nonmetals. Because of this technology can acquire some special performance without changing the original performance of material, and carry out an effective surface protection for the material. Therefore, the technology was widely applied in product manufacturing fields and become an advanced production technology [1]. This experiment uses the surface engineering techniques, developing and testing the mulberry silk brocade fabrics to achieve the effective protection of high range silk decoration product.

Experimental Materials and Equipments

Experimental Materials

Mulberry silk brocade fabric: 100% mulberry silk fabric bought from market.

Surface treatment agent: water-soluble latex to form film, solid content 30%, provided by Jiangsu Silk Research Institute.

Antimicrobial agent: FM-2598, provided by Jiangsu Silk Research Institute.

Standard germ stub: PS-11 standard penicillium stub, provided by Microorganism Laboratory of Suzhou Vocational University [2,3]. Czapeck culture media: sodium nitrate 2g, bipotassium hydrophosphate 1g, potassium chloride 0.5 g, the magnesium sulfate 0.5g, ferrous sulfate 0.01 g, cane sugar 30 g, agar 15-20g, water 1000 ml, prepared by ourselves.

Experimental Equipments. Liquid bath, padding roller (made by ourselves), E5EM type heating press machine (Suzhou Yuandong Hardware & Electrical Appliance Factory), Hitachi S4700 type scanning electron microscope (made by Hitachi Corporation), JB-CJ-1F type super net workbench (Suzhou Purify Equipment Limited Company), Autoclave ES2315 high pressure sterilizing pot (Medical Equipment Plant of Shanghai Boxin Industrial Limited Company), ZHWY22102 type constant temperature culturing box (Changsa Xiangyi Centrifugal Instrument Limited Company), YG(B) 026PC electron fabric strength tester (Wenzhou Darong Textile Instrument Limited Company),YG811 fabric drape tester (Wenzhou Textile Instrument Plant), AP-360 fabric breathability tester (Japan DAIRON Fine Instrument Plant).

Experiment Measures

Preparation of Test Samples. The synthetic resin emulsion was diluted to concentration 10% with water, and then added 5% antibacterial agent to form working liquid. Mulberry silk brocade fabric sample was evenly immersed in the liquid, and the immersion time was total 30 minutes. During that time, the sample was taken out from the liquid at former15 minutes, and its surface was slightly rolled twice using padding roller. After natural dryness, the sample was put into heating press machine to hot each side one minute at 75 ℃ temperature. Finally test sample was prepared to use for the following test.

Electron Microscope Scanning Test. Mulberry silk fabric and the test sample were treated separately for spraying. Then observe and record their superficial appearances under scanning electron microscope. Magnification of scanning electron microscope was 50 times.

Antimicrobial and Mildew-resistant Test

1) Sample preparation. Mulberry silk fabric and the test sample were separately cut into a 3.8±0.5cm diameter round sample. The test samples were prepared for two groups test.

2) Preparing germ suspension liquid. The germ crumb was scraped from the matured green mildew seed culture germ were added into conical flask with 50±1ml sterile water and glass balls, then shaking the flask to make germ spore suspending in water.

3) Inoculation. Make the spore suspension liquid (1.0±0.1ml) evenly spread on the agar surface.

4) Soaking. The round sample was pre-wetted with water solved 0.05% non-ion wetting agent, and put it on the agar surface. Then 0.2±0.01ml germ suspension liquid was evenly spread on each round sample with sterilized pipet.

5) Culturing and recording. The round samples were put in culture dish to incubate at 28±1℃ for 6, 9, 12days, till 15days. The fungi erosion situation at sample surface was observed and recorded [4,5].

Tensile Strength Test. Mulberry silk fabric and the test sample were cut into a 50mm width strap sample, to test their breaking strength and elongation respectively on fabric strength tester. Setting gauge length as 200mms±1mm, preset tension as 200 CN, tensile velocity as 100 mm/min [6].

Drape Test. Mulberry silk fabric and the test sample were cut into a 240mm diameter round test samples, and tested their drape coefficient on the fabric drape tester [7].

Breathability Test. Mulberry silk fabric and the test sample were cut into a 20cm^2 area test sample, and measured their breathability on the fabric breathability tester to get the different breath rate of treated materials and control ones. Testing pressure drops to 100Pa [8] .

Results and Discussion

Characteristics of mulberry silk brocade materials and surface treatment techniques. The mulberry silk brocade is a pure natural silk fabric woven with mulberry silk in warp and weft. It adopts brocade weave structure so that surface structure of this fabric is looser relatively. The brocade structure is made up by multiple groups of warp and weft yarns overlapped with each other. Therefore, it is inevitably that a quantitative long float threads exist on its surface and forming sinking crossing-link pits on up and back. The section structure of mulberry silk brocade fabrics is shown in Fig. 1.

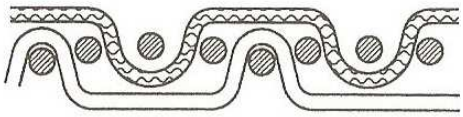

Fig. 1 Section structure of mulberry silk brocade fabrics

Although mulberry silk brocade has looser surface structure, its coverage factor is not lower than other silk fabrics such as gauze or leno etc., and it has higher open porosity. That because the silk yarns overlapped with each other. Otherwise, mulberry silk brocade's surface has some long float yarns, so it doesn't have stability structure as others, such as habotai and plain silk. The routine

method of surface treatment for textile is surface coating. That is to say, it uses blade or roller coating head to apply coating agent on fabric surface and makes treating agent to the fabric's back under the external force. So the agent can bond the yarn weaving points and prevent from the yarns' free sliding. It finally makes the fabric structure closing, stiff and stable. Considering the performance of mulberry silk brocade and its application, the routine method cannot be suitable. Special method should be applied to control the penetration of react agent and effective bonding of yarns. Because mulberry silk brocade should be treated in relax state of warp and weft, it is hardly to realize the treatment by use of blade or roller head coating.

This experiment adopted the surface treatment measures of multiple impregnating and padding, which employed some times of slight roll padding during impregnating process. The first roll-padding was arranged after impregnating fabric15 minutes, in order to make the dry material wetted sufficiently. After the limited penetration, the roll-padding increased the effective bonding between react agent and the mulberry silk material, and carried out the even spreading react agent on the convex surface of material. Because the process of mulberry silk brocade surface treatment was in loose and tensionless status, so the viscosity of treating liquid should be controlled properly. If the viscosity is too higher, the surface silk fiber may be slipping and sliding while slightly roll-padding.

Fig. 2 is a SEM photograph of mulberry silk brocade surface appearance after surface treatment, which shows the fibers of mulberry silk brocade fabric were whole coated by treating agent. The state of film-forming is perfect.

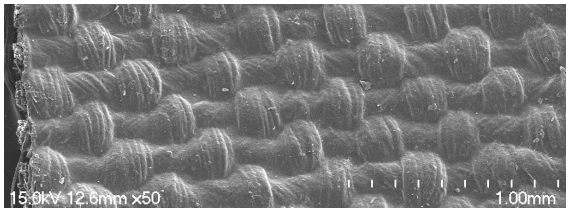

Fig. 2 Perfect film-forming state after surface treatment to mulberry silk brocade

Comparison of mulberry silk brocade's antimicrobial properties after surface treatment works. The aim of surface treatment is to form a layer of protective film on the silk fiber's surface and to block erosion of fungi microbes to silk fiber. Mulberry silk fiber is an organic material and necessary for its growth. So in certain proper environment, the fungi suspending in air will be colon on silk fiber surface and quickly growing, till to produce spores and form bacterial colony. Surface treatment took a layer of membrane as medium to deal with the fiber surface, the medium not only links silk fiber and air but also separates them, to block fungi hypha from penetration into silk fiber matrix. It is used to cut off the nutrition source to control fungi growing. This treatment form a closing environment to silk fibers, which can block off oxygen and keep internal material environment not influenced by outside, such as humidity, oxygen and pH value, etc.

If the design of antimicrobial agent is used in film-forming latex, it will have block action and also a further action to break off fungi glowing. It will change the single isolation action into a double action way of passive suppressing and active antimicrobial to kill the living microorganism. So that it will achieve more effective antimicrobial results [9].

Fig. 3 and Fig. 4 showed differences between surfaces treated mulberry silk brocade fabrics and untreated ones, culturing for 6, 9,12and 15days.

Fig. 3 The fungi growing state of untreated mulberry silk brocade fabrics' surface

Fig. 4 The fungi growing state of treated mulberry silk brocade fabrics' surface

The results of experiment showed that the silk material will not be corroded by fungi after the protective film forming on the surface of mulberry silk brocade fabric, as indicated in figure 4. 15 days later since germ culturing, the surface of material still maintain clarity and clean. That is to say, fungi cannot be survival at its surface and they must be away from the material, for antibitoic action of protective film. When germ cultured for 12 days, germ spores growing and developing colony appeared at marginal area of culture dish. It was shown in fig.4, the black area at dish fringe, but the surface of silk material is still clarity and clean.

The state of untreated silk material was great different. As shown in fig. 3, after germ culturing for 6 days, fungi spores appeared at the surface of silk material and spread in pits and pieces. 9 days later, the spores produced different sizes of colony clearly. When 15 days, colony produced by the spores can cover the whole surface of silk material. According to AATCC-30 standard (ANTIFUNGAL ACTIVITY ASSESMENT ON TEXTILE MATERIALS: MILDEW AND ROT RESISTANCE OF TEXTILE MATERIALS), it is up to the state of "macroscopic growing", which also means a degree can be observed evidently by naked eyes. Compared with the treated silk materials, it belongs to a state of "non-growing", its antimicrobial and microorganism resistant effect is obvious.

The influences of the surface treatment on mulberry silk brocade fabric performances. Mulberry silk fiber is a natural fiber reeled from silkworm cocoons, which has good elongation and flexibility as high grade textile materials to use. The mulberry silk brocade fabric made from pure silk contains the all good performances of natural silk. Meanwhile, its antimicrobial and rot resistant properties will be enhanced by surface treatment, which provides a layer of antimicrobial protective film suitable for various high grade decoration engineering. But surface treatment makes fabric stiffen and bonding the yarns so that the elongation and flexibility of fabric were influenced.

As a high range silk product, the mulberry silk brocade fabric should be treated without or less influences on its original performances, especially the tensile elongation, flexibility and breathability. To realize the aim of antimicrobial resistant function, this experiment made use of the limited treating agent penetration, effective bonding and both original and additional performances.

The following diagram listed the tensile elongation, flexibility and breathability test results of mulberry silk brocade fabrics treated and untreated, as shown in Table 1.

Table 1. Mechanical property of mulberry silk brocade fabrics treated and untreated in the test

Test Item	Breaking strength(N/mm)	Breaking elongation(%)	Drape coefficient(%)	Breathability (mm/s)
Fabric untreated	13．64	16．08	24．5	2542
Fabric treated	13．54	17．88	24．8	2406

Table 1 shows that the breaking strength of mulberry silk brocade fabrics treated has a small change without any influence upon the original performance, but the breaking elongation is improved that of treated one is 17.88% and untreated one is 16.08%. It indicated that the treating agent was not penetrated into the back of fabric to bond the weaving points of fabric, and then to block the yarns free sliding in the fabric. In the opposite, the limited penetration and effective bonding were only appeared on the surface of fabric, so it lubricated the fibers efficiently. Finally the fibers may be slipped in some degree by force leads to the improvement of elongation.

Fabric draping is performance that the fabric is able to free drop under its deadweight action. It reflects the flexibility of material, and the drape coefficient is a percentage ratio of the sample sag projection area and its original area. Therefore, the smaller drape coefficient, the better material flexibility is. Because mulberry silk brocade fiber is soft, its fabric is also soft. According to the data of drafting test, its drape coefficient is 24.5%, 30% smaller than that of other fabrics. This value of treated fabric was 24.8%, just 0.03% greater than untreated fabric, which is less than the error range of the test method (±2 % error range). It indicated that loose structure of material would not be damaged by the film-forming latex, good soft state of the whole fabric would be still maintained.

Considering the materials' elongation and flexibility, it may be deemed that the original function and structure of the materials were not damaged by surface treatment but to increase the action of anti-aging antibacterial mold. It was validated by the test of breathability. Although the routine surface treatment used to make the materials stiffen and breathability dropping greatly. But in this experiment, the breathability test results of the treated materials only decreased 5.4% smaller than that of original materials. It can be considered that the pores between fibers in fabric were still open, and the surface treatment had less influence on the original performance of mulberry silk brocade fabrics.

Conclusions

The surface engineering teghnology can modify the surface performance and provide effective surface protection for the materials by use of surface coating, which can be used in mental and non-metal materials also including textile materials. Using this technology, it can acquire additional special performances without changing original performance of material, and carry out useful surface safeguard for materials, therefore the technology is widely applied in many manufacture fields as advanced processing techniques.

Developing and testing the mulberry silk brocade fabric by use of the surface engineering techniques, it not only provided the additional functions, but also maintains the original performances of material with reasonable processes and techniques. Especially by the way of the limited treating agent penetration and effective bonding, the fabric can acquire additional antimicrobial and rot resistant functions, and at the same time maintain original performances including the breaking strength and elongation, breathability and drape coefficient.

Surface treatment is designed to form a layer of membrane as medium between silk fibers and air which separate them but also link them. This medium can block fungi hypha from penetrating into silk fiber matrix and cut off the nutrition source to control fungi growing. Meanwhile, the design is added an antimicrobial agent in film-forming latex, besides blocking action, it will also further break off fungi glowing. The added agent will change the single isolation action into double action way with passive suppressing and active antimicrobial. This way can be used in the different fields, such as high grade silk decoration products, natural silk home textiles and industrial silk products, to satisfy the wash-less characteristics of these products and achieve effective protection for the high grade silk decoration products.

Acknowledgements

A Project Funded by the Priority Academic Program Development of Jiangsu Higher Education Institutions.

References

[1] Yinfang Jiang, *in: Modern Surface Engineering Technology*, Beijing, Chemical Industry Press, 2006, p. 3-12

[2] Jinying Tian, Chunlei Wang, Zhiping Bai, *in: The Research of Ancient Cultural Relic Silk Goods Mildewed Spot Clearance*, Cultural Relic Protection and Archaeology Science Press, 2005. 17: (4), p. 1-6

[3] Deqing Zhou, *in: The Microbiology Experiment Manual,* Shanghai: Shanghai Science & Technology Press, p. 164-194(1986)

[4] Yuanlin Xiong, *in: The Microbiology Experiment*, Wuhan: Central China Normal University Press, p. 30-35(2008)

[5] Junhui Ji, *in: Antimicrobial Materials,* Beijing: Chemical Industry Press, p. 344-348(2004)

[6] [7] [8] Textile Industrial Standardization Research Institute. China Textile Standards Collection, Beijing: China Standard Press. No.1, p.215-221(2007); No.4, p.172-175; No.1, p. 297-302

[9] Shichao Li, Changbo Tang, *in: Isothiazolinones Resin Antimicrobial Finishing on Natural Silk*, Silk. No.9, p. 29-31(2009)

Advanced Materials Research Vols. 314-316 (2011) pp 23-27

doi:10.4028/www.scientific.net/AMR.314-316.23

Cladding of Tantalum and Niobium on Titanium by Electron Beam, Injected in Atmosphere

M.G. Golkovsky[1, f] T.V. Zhuravina[2, b], I.A. Bataev[2, c], A.A. Bataev[2, d], S.V. Veselov[2, e], V.A. Bataev[2, f], E.A. Prikhodko[2, g]

[1] 630090 Russia, Novosibirsk, Academician Lavrent'ev ave, 11

[2]630092 Russia, Novosibirsk, Karl Marks ave., 20

[a] golkovsky@inp.nsk.su, [b] zhuravina@ngs.ru, [c] ivanbataev@ngs.ru, [d] bataev@adm.nstu.ru,

[e] veselov_s@inbox.ru, [f] vabataev@yandex.ru, [g] helens_case@ngs.ru

Keywords: cladding, tantalum, niobium, titanium, electron beam.

Abstract. The aim of the work was to clad Ti-Ta-Nb coating on a substrate of pure titanium. Cladding was carried out by non-vacuum electron-beam treatment. As a result a good quality coating thickness of about 2 mm was obtained. Microstructural and microhardness tests were conducted. Dendritic structure and the borders of the former grains of β-phase were revealed. At the microlevel, the coating has a martensitic structure. The average hardness of coating is about 4000 MPa.

Introduction

At the present time titanium and its alloys are the most popular materials destined for use in aggressive environments. The wide use of titanium in many areas of industry is explained by high set of its physical and mechanical properties, particularly by high specific strength and phenomenal corrosion resistance. Nevertheless, even more stringent requirements to materials properties are required in some fields of industry. Tantalum has even higher corrosion resistance compared to titanium. This material is resistant to almost all kinds of acids, as well as to many liquid metals (Na, K, Li). However the widespread use of tantalum is limited by several factors, mainly its high cost and low production volumes. In recent years, new alloys of Ta-Ti-Nb system are of particular interest due to their high corrosion resistance and lower price compared to pure tantalum.

In papers [1,2] it was noted that alloy containing 40 % of tantalum provides the same corrosion resistance as that of pure tantalum. Authors of [3] note that alloys of titanium and tantalum are the most promising for nuclear waste processing plants, when it is important to take into account corrosion resistance, mechanical properties, availability and cost of material. Possible application of Ta-Ti-Nb alloys in biomedicine was noted in [4].

Ta-Ti-Nb coatings on a substrate of pure titanium are promising from the position of the cost reduction of the corrosion resistant composition. This work studies the structure of Ta-Ti-Nb coatings, obtained on a pure titanium substrate by high-power electron beam injected in the atmosphere. The advantages of this method are that the coating is produced in an air atmosphere and the process is short [5].

Experimental procedure and research methods

Commercially pure titanium plates were used as substrates. Dimensions of the substrates were as follows: 100x50x10 mm. Powders of pure titanium, tantalum and niobium were used for cladding. Some characteristics of cladding powder are presented in table 1. It should be noted that commercially available powders of tantalum, niobium and titanium contain sufficiently large amount of oxygen on the surface. CaF_2 and LiF mixture was used as flux. Non-vacuum electron beam cladding was performed on the facility ELV-6, produced by the Budker Institute of Nuclear Physics SB RAS.

Table 1. Features of cladding powders.

Powder type	Ta	Nb	Ti
Oxygen content according to EDX-analysis, wt. %	5,7	3,5	-
The average particle size, μm	100	40	5 – 200*

* - Porous titanium with the size of the porous conglomerates of about 200 microns, composed of particles about 5 microns was used.

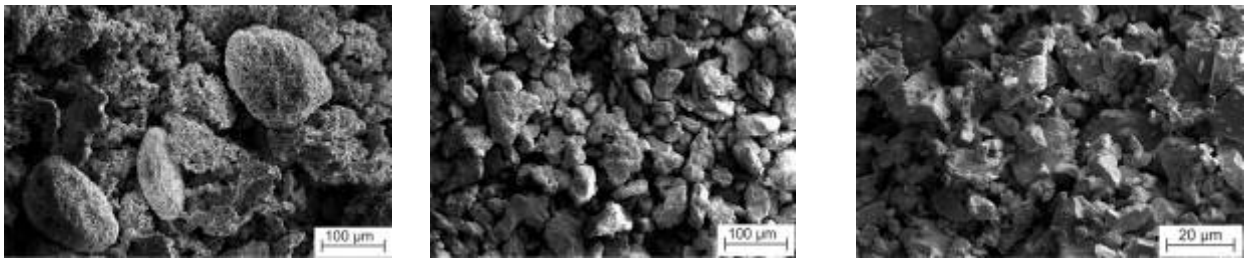

a) b) c)

Fig. 1. Photos of the powders used for deposition a) titanium b) tantalum c) niobium

Before the cladding mixtures of Ta, Ti and Nb powders with addition of the flux were deposited on the substrate surface. The composition of the mixture is presented in table 2. During the cladding the substrate with a layer of powder progressively moved relative to the electron beam at a speed of 10 mm/sec. In order to increase processing efficiency beam scanned the surface of the sample in the transverse direction. Scanning amplitude was equal to the width of the sample (50 mm). Scanning frequency (50 Hz) was sufficient to ensure the homogeneity of the beam exposure over the sample area. Electrons energy was 1,4 MeV, beam power was 33,5 kW.

Table 2. Parameters of treatment and composition of the alloy

Powders filling density [g/cm^2]	Velocity of the samples' movement [mm/s]	Beam current [mA]	Mass fraction of the component before cladding [%]				
			Ta	Nb	Ti	CaF_2	LiF
0,45	10	24	26	26	18	23,3	8

The cladding structure was studied by metallographic analysis using a microscope AxioObserver A1m. Mechanically polished cross-sections were etched by a five percent aqueous solution of hydrofluoric acid. To study local chemical composition of the cladding scanning electron microscope Carl Zeiss EVO50 with INCA XACT EDX-analyzer was used. Diffraction patterns were recorded by θ-θ diffractometer using a copper X-ray tube as a source of X-rays. Pictures were recorded with increments $\Delta 2\theta = 0{,}02°$ and 0.05° and dwell time 3 - 9 sec. Microhardness studies were performed using the device WolpertGroup 402MVD. Four-sided diamond pyramid was used as indenter. The load on the indenter was 0.98 N.

Results and discussion

Fig. 2 shows appearance of the coating formed during the cladding. The cladding thickness is about 2 mm. At least three clearly separated zones can be marked out in the cladding structure: a zone of a melted metal (1), a heat affected zone (2) and an unaffected zone (3). Average chemical composition of the cladding determined by EDX microanalyses is presented in table 3.

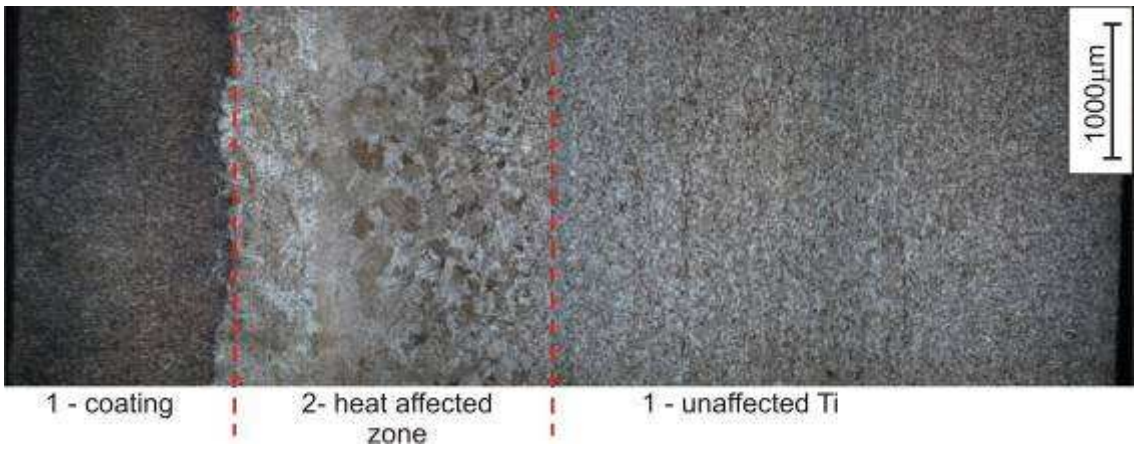

Fig. 2. The cladding appearance

Contours of dendritic structure formed during primary crystallization is seen in the molten metal (zone 1). The most clearly dendritic morphology of coatings was observed by the SEM using back scatter electron detector (Fig. 3a). In this case, the dendrites appear as bright and interdendritic spaces in the form of dark areas. Large dendritic crystals are drawn towards the direction of heatsink. High contrast between the branches of dendrites and interdendritic spacing is indirect evidence of a difference in chemical composition and structure of these areas. Results of EDX-analysis, obtained at points 1 and 2 (Fig. 3a) are presented in Table 4. It should be noted that the precise quantification of the oxygen content in titanium by EDX-analysis is a difficult task. This is because the Kα-line of oxygen and L-line of titanium are sufficiently close to each other. Nevertheless, the analysis of the spectral profile presented in Fig. 4a indicates of the presence of a certain amount of oxygen in the material. Its presence may be caused by the oxygen adsorbed in the starting powders and coatings interaction with the atmosphere during the cladding. Preferential concentration of oxygen in the interdendritic spacing is also observed in the maps of oxygen distribution (Fig. 3b).

Table 3. Average chemical composition of the coating (results of EDX - Analysis)

Element	Ta	Nb	O	Ti
Content (wt %)	19,2	18,8	6	the rest

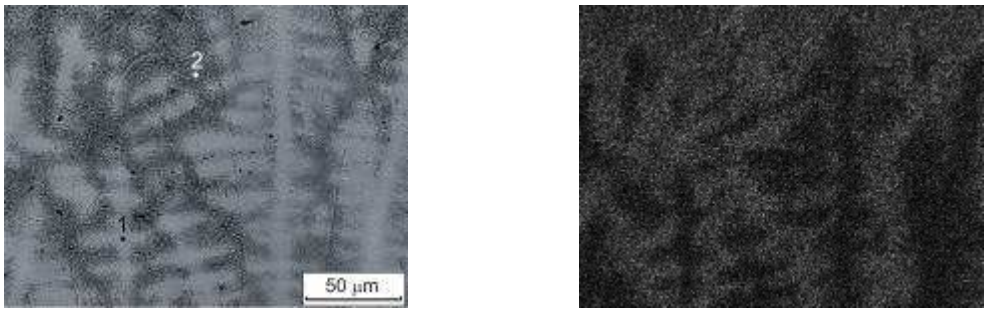

a) b)

Fig. 3. The structure of the coating (in backscattered electrons) (a) and the map of oxygen distribution (b).

Table 4. The results of EDX-microanalysis of the points 1 and 2 (see Fig.3a)

	Ta	Nb	O	Ti
Point 1	21,6	20,2	3,8	the rest
Point 2	18,3	14,3	12,2	the rest

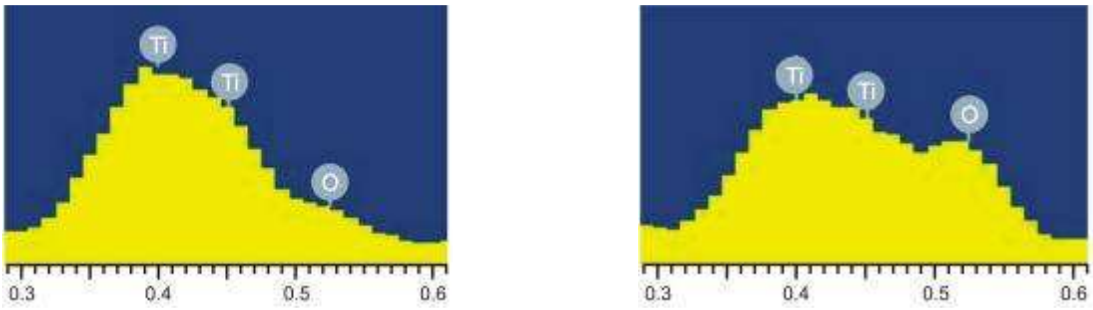

Fig. 4. Sections of the spectra in the low energies, obtained from the point 1 (a) and point 2 (b)

(see Fig. 3a)

It should be noted that boundaries of large grains can be clearly seen against the dendritic background (Fig. 3a). Analysis of many regions revealed that dendrites are often crossed by grain boundaries. This fact indicates that the formation of grains occurred after the formation of dendritic structure. Data provided by the authors of [6], suggest that the boundaries observed in the photographs are probably the boundaries of the former β-phase.

To carry out X-ray analysis the coating material was prepared in form of randomly oriented particles of size 10 - 100 nm. This complication of the sample preparation technology was done in order to obtain non-textured objects. Obtained X-Ray pattern is shown in Fig. 5. Analysis of the diffraction patterns of powder material led to the assumption of the presence of cubic modification of titanium (β-Ti). This assumption was based on analysis of the diffraction peaks intensities distribution. The ratio of the integrated intensities of most of α-titanium peaks correspond to the distribution of randomly oriented powder. At the same time, the intensity of the (002) peak substantially exceeds the average value, typical for the samples without texture. One can suppose that the strongest line of β-titanium (110) planes also contributes to this peak. Absence of the remaining β-titanium peaks reflects the small volume fraction of this phase in the sample. This phenomenon was also observed by the authors of [6].

The fine structure of the coating was analyzed by SEM and TEM. Analysis of the photographs presented in Fig. 6, indicates that during the cooling process diffusionless transformations $\beta \rightarrow \alpha'$ occurred and elongated crystals of α'-phase in the martensitic morphology were formed. The method of electron diffraction confirmed the presence of a small amount of residual β-phase.

Microhardness distribution profile is shown on Fig. 7. The average level of the coatings microhardness was 4000 MPa, while the microhardness of the initial titanium was at the level of 2000 MPa.

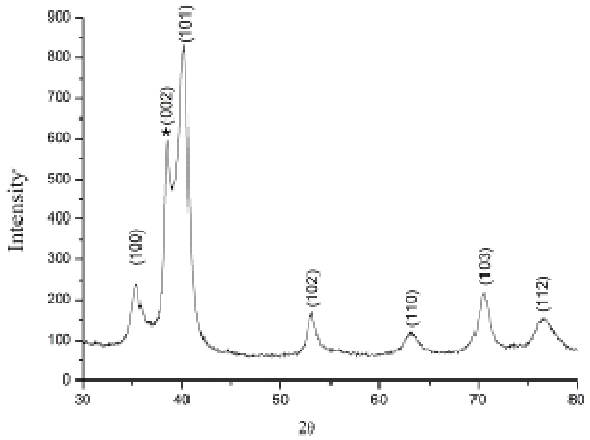

Fig. 5. X-ray pattern of the cladding material ground to the state powder.

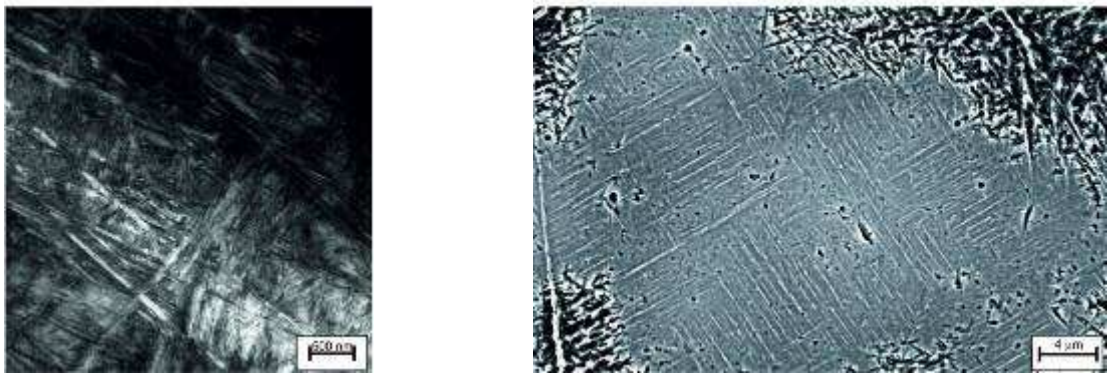

a) b)

Fig. 6. Martensitic microstructure of the coating: a – TEM, b – SEM.

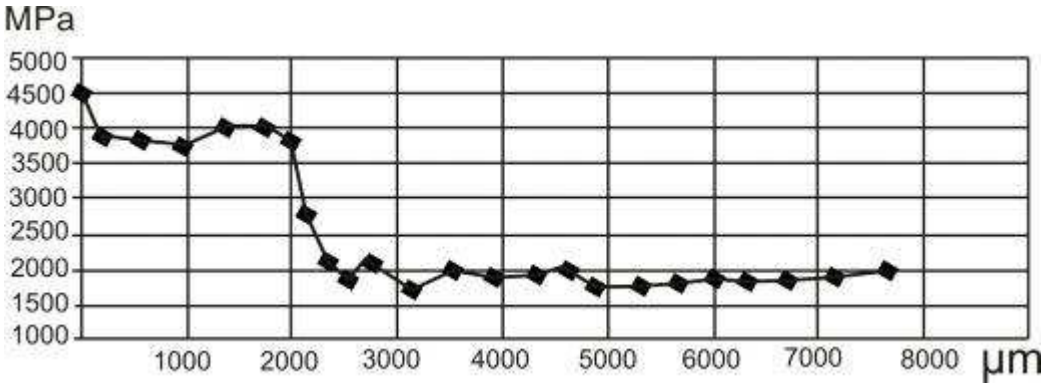

Fig. 7. Microhardness distribution profile

Conclusion

Ti-Ta-Nb coating with a thickness of about 2 mm was formed on a substrate of pure titanium by non-vacuum electron beam cladding. This methods provides high quality of coatings, without pores and cracks. The average microhardness of the coating is about 4000 MPa. The coating structure retained the contours of dendritic structure, and perhaps, the boundaries of the former β-phase grains. At the micro level, the coating has a structure of martensite. Elevated content of oxygen was found in interdendritic spacing. In order to reduce the oxygen content more pure starting powders should be used.

References

[1]. Andrei Ionut Mardare, Alan Savan, Alfred Ludwig, Andreas Dirk Wieck, Achim Walter Hasse: Corrosion Science 51 (2009) pp. 1519–1527

[2]. Karen Alves de Souza, Alain Robin: Materials Chemistry and Physics 103 (2007) pp. 351–360

[3]. Baldev Raj, U. Kamachi Mudali: Progress in Nuclear Energy 48 (2006) pp. 283–313.

[4]. Ying-Long Zhou, Mitsuo Niinomi: Materials Science and Engineering C 29 (2009) pp. 1061–1065

[5]. J.C. Oh, E. Yun, S. Lee, M.G. Golkovski: Materials Science and Engineering: A (2003) V. 351. № 1-2. pp. 98-108.

[6]. R. Mythili, V. Thomas Paul, S. Saroja, M. Vijayalakshmi, V.S. Raghunathan: Materials Science in Engineering A 390 (2005) pp. 299-312

Advanced Materials Research Vols. 314-316 (2011) pp 28-32

doi:10.4028/www.scientific.net/AMR.314-316.28

The Research on Cylindrical Ultrasonic Rolling Machining Used for Strengthening Metal Surface

Wenrui Chen[1, a], Yong Ma[1, b] and Zhifeng Lou[1, c]

[1]Key Laboratory for Precision & Non-traditional Machining of Ministry of Education, Dalian, Liaoning, 116023, China;

[a]chen.wenrui@yahoo.com.cn, [b]yongma@dlut.edu.cn, [c]louzf@dlut.edu.cn

Keywords: ultrasonic; roller; the size of grain; yield strength

Abstract. Material mechanics and dynamic properties affect the service life of parts, and also the normal operation of machines. In order to reduce the processing time and improve the quality of machining, a cylindrical roller was used in the research. Cylindrical ultrasonic rolling machining (CURM) is an efficient way to enhance the service properties and surface characteristics of components. CURM was designed and later tested on the 45# steel surface. The result showed that the plastic deformation of surface layer was symmetrical and the surface grain was reduced in size by approximately 4.2%. The result of the experiment showed that CURM was effective in enhancing the productivity as well as enlarging the yield strength and hardness of components.

Introduction

With the development of mechanical manufacturing, mechanical parts are applied widely in science & technology field, such as in mechanical industries, astronautic industry, vehicles, transformers, among other things. The surface faults of mechanical parts are considered to be the most important factor to affect the service life and to some extent the normal operation of a machine. The technology of material aggrandizement can improve material mechanics, while enhancing dynamic properties. It not only increases the adaptation to the environment, but more importantly, it also prolongs service life of mechanical parts and the complete machine.

Ultrasonic rolling machining is one of new surface hardening technology. It has many advantages in improving properties of materials and increasing their service life. A great deal of tests have shown that Ultrasonic rolling machining has a positive effect on reducing surface roughness, increasing micro hardness and developing a significant residual compressive stress in the surface of metal[1~2].

At present, it is the main strengthening method that makes use of the relative motion between the work piece and steel ball which rolls freely in the tool [3~5]. Owing to the limit of the amount of feed and the diameter of the ball, there are some light and dark fringes caused by improperly choosing technical parameters in the strengthening process on the processed surface. These conditions seriously influence the machining precision, the continuity of plastic deformation, and block the equalization of the residual stress in the surface layer. Moreover, this kind of measure is inefficient because of the feed on both side of the surface. At the same time, it is inconvenient to strength irregular surfaces such as the surface of gear.

In this paper, the structure of the tool is transformed. A cylindrical roller was used to replace the rolling ball. The type of contact changed from point contact to line as well as the progress of gearing. It can solve the problem resulted from the ball. The experiment on the 45# steel surface shows that the plastic deformation of surface layer was symmetrical and the surface grain size was reduced. Thus, not only the contour accuracy was guaranteed, but also the machining efficiency was increased greatly. The strengthening characteristics are represented summarily.

The Principle and Experimental Device of CURM

The Principle of CURM. Cylindrical Ultrasonic rolling machining is compound machining technology. Ultrasound technology has an additive source of mechanical power, when it combined with the traditional rolling processing in the strengthened process. Under the cooperative action of extrusion pressure and shock action of ultrasonic, the tool contacts with the surface of work piece which causes the surface layer of metal to plastically deform. Waves through on the surface, which affect the surface finish on a micro scale, were filled by the crest. The surface roughness was lower because of the plastic flow. After several times of processing, there was a uniform metal surface layer of plastic and elastic deformation. Due to the recoverability of the elastic deformation and non-restorative plastic deformation of plastic deformation non-restorative, the residual compressive stress was generated in a certain depth. It helped to prevent the formation of surface micro-cracks, increase the service life of parts, and improved the mechanical properties of the metal surface. In the CURM, grains on the surface absorbed the tremendous energy generated by the ultrasonic vibration. The number and the density of surface defect were increased. The defect clusters made the grain boundaries and sub grain boundaries produce. The grain size is reduced [6].

The Experimental Device of CURM. At present, a popular procedure is to use a rolling ball to strengthen the surface area. In this experiment, a point on the surface was connected to the ball. It increased processing time and lowered the processing efficiency. In response to these problems, the experimental device of CURM was designed as shown in Fig. 1. Fig. 1(a) refers to the experimental device of CURM. Fig. 1(b) is the amplification of the tool.

Different from the traditional point-connect type, in this apparatus, the tool is a deforming cylinder holding a cylindrical roller designed as wide or nearly as wide as part. The roller rotated smoothly and knocked the surface regularly. It reduced wear and extended the service life of the tool because of the character of rolling friction. Generatrix of roller prolonged the line which connected with the surface. By eliminating traverse feed it improved the machining precision of part, and reduced the time of processing.

(a) (b)

Fig. 1 The Experimental Device of CURM

The device comprised of four parts, an ultrasonic generator for generating high frequency energy of 20 kHz, ultrasonic actuating mechanism, x-y mobile device for moving the part to realize horizontal and vertical feeding, and a pressing unit for applying a static pressure to maintain the continuous ball contacting with the part surface. The ultrasonic vibration system is a core of the power ultrasonic equipment generally composed of transducer, amplitude transformer and tool.

After static pressure was applied, ultrasonic transducer received the electricity resonant signals produced by ultrasonic generator and converted it into mechanical vibration. An amplitude transformer increased and transmitted the amplitude output wave function. Such vibrations made the tool vibrated on the part surface area while the tool moves along the surface. The center of frequency of the device was 20 kHz, and the output of amplitude was between 0 and 25μm.

Table 1 The chemical composition of 45# steel (mass fraction %)

Material	C	Si	Mn	Cr	Ni	Cu
45	0.42～0.50	0.17～0.37	0.50～0.80	≤0.25	≤0.3	≤0.25

Experimental Method and Results Discuss

Test Material and Experimental Method. The sample material was 45# steel. In order to facilitate the detection of X-ray diffractometer, the size was 15mm×10mm×2mm. Basic properties of materials were that yield strength was 355MPa and the tensile strength was 600MPa. The chemical composition of 45# steel was shown in Table 1.

The test used the device of Cylindrical Ultrasonic rolling machining. Specific processing parameters are shown in Table 2.

Table 2 Processing parameters

Frequency (kHz)	Static pressure(N)	Feed speed (mm/s)	Amplitude (μm)	Times of process	Size of rolle(mm×mm)	Ra (μm)
20	150	1	12	8	5 × 12	0.02

Surface Roughness of CURM. The surface roughness measurements of treated surfaces by CURM are given in Table 3. The results showed that the surface roughness in longitudinal direction was decreased after both processes. However, the surface roughness in Longitudinal direction is very high after CURM treatment. This is due to the high plastic deformation obtained after UDCR which results in even higher peaks and deeper valleys on the treated surface as compared to those on the untreated surface.

Table 3 Surface roughness parameter Ra(μm)

	Direction of the Surface	
	Longitudinal	Transverse
Untreated surface	0.49	0.23
Treated surface	0.25	0.18

Surface Topography of CURM. Repeated processing did not only increase processing time, but also made the squamous pattern generated on the surface and improved surface roughness of the workpiece. Cylindrical roller can effectively solve the problem by the way of no transverse feed. There are two pictures processed by scanning electron microscope (SEM) in Fig. 2. Fig. 2 (a) shows the surface topography prior to processing, Fig. 2 (b) is the surface processed by the equipment of CURM

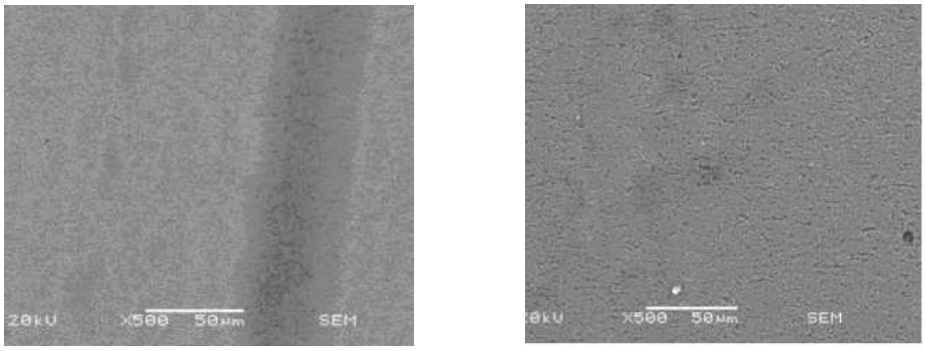

(a) (b)

Fig. 2 Observation of SEM

As we can see in Fig. 2 (a), significantly, there are banding pits on the surface, which is the scratch produced by cutting plan. There are some uniform and shallower pits on the surface of Fig. 2 (b). Owing to the smoothing effect of the roller, the pits were filled, and it improved the surface finish. Surface pits are evenly throughout the surface so that the plastic deformation of the surface was uniformed, and equal deformation layer can prevent stress relaxation

Observation of Treated and Untreated Surface by XRD. Fig. 3 shows the untreated and treated surfaces by CURM taken by X-ray diffraction. Comparing the two compare, it shows that the diffraction peaks shift to the right. It meant that diffraction angle increased by less than 90 °.

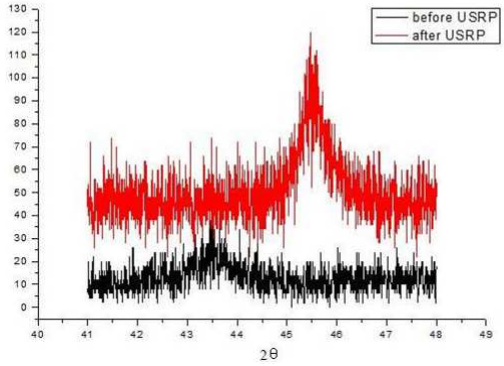

Fig. 3 The Result of XRD

The relation between the Diffraction angle and the grain size on the metal surface is shown in Bragg [7].

$$2d\sin\theta = n\lambda \quad (1)$$

In this equation: λ is wavelength; d is interplanar spacing, θ is Bragg angle, which is equal to 1/2 of diffraction angle.

From Eq. 1，interplanar spacing was inversely proportional to the sine value of diffraction angle. From 42°to 47°, Bragg angle and the diffraction angle increased and the sine of it changes in the same direction. As the diffraction peaked and shifted to the right, the diffraction angle 2θ increased, sinθ increased. After calculated, grain size was decreased by approximately 4.2%. CURM then produced a large number of sub-grains. Sub-surface structure of the metal is refined. In the beginning, plastic deformation on the surface appears. With the increase in processing time the amount of plastic deformation increased and gradually progressed to the deeper surface. Constant moving and proliferation of Dislocation in the grain led to dislocation annihilation and rearrangement, and form dislocation tangles. As the deformation continues, the high dislocation density separated by areas with low dislocation density, the lattice is formed in the original smaller dislocation cells. With the strain increasing, dislocation cells increased in the number and reduced in the size. High-density dislocation tangles concentrated around the cell wall and came to the composition like cell wall. Finally there are many sub-grains within the grain, the size of grains on the metal surface is smaller. The smaller the grains are, the more grain boundaries and sub grain boundaries appeared and the more obstacles to dislocation movement appeared. It needed greater resistance to transform, which played the role of grain boundary strengthening,

Smaller grain size in the same volume needs the larger number of grains in the same deformation. The deformation was more evenly distributed, which could withstand greater surface deformation. This was helpful in improving the plastic parts.

The relationship between grain size and sub-grain size and can be conveyed in Hall–Petch equation. σ_s is the yield strength of the metal, σ_0 is decided by the material. K is a constant, d is the diameter of the grain [8].

$$\sigma_s = \sigma_0 + Kd^{-1/2} \quad (2)$$

According to Hall–Petch equation, when grain size becomes smaller, it becomes greater on the surface treated by CURM, the grain size then reduces by about 4.2%, so that it is obvious that CURM is an effective way to enlarge the yield strength and hardness of the metal.

Conclusion

The investigations revealed that CURM is a reliable and effective surface enhancement technique as it can be used for enhancing the service properties and surface characteristics of 45# steel components. It can improve the surface finish. The plastic deformation of the surface is uniform, and equal deformation layer can prevent stress relaxation. It is an effective way to reduce the processing time, and enhance the productivity. In further study, it can be used into the irregular surface such as the work piece of an involute gear caused by changing the route of the roller.

Work hardening on the surface is achieved. It can reduce the size of grains about 4.2%, and enlarge the yield strength and hardness of the metal. These physical effects lead to improvement of fatigue strength of components as well as increase in resistance to corrosion and foreign objects.

Acknowledgement

This project is supported by National Natural Science Foundation of China (No.50905026), the National High Technology Research and Development Program of China (No. 2008AA042506) and Dr. Scientific Research Start Foundation, Liaoning Province (No. 20091013).

References

[1] Ting Wang, Dongpo Wang and Gang Liu: Baoming Gong and Ningxia Song: Journal of Mechanical Engineering. 45(2009), p.177(In Chinese)

[2] Youli Zhu, Li Li, Kan Wang and Yuanlin Huang: Chinese Journal of Mechanical Engineering. 39(2003), p. 1(In Chinese)

[3] R.K. Nalla, et al: Materials Science and Engineering. A355 (2003), p.216

[4] A. Tolga Bozdana, Nabil N.Z. Gindy and Hua Li: International Journal of Machine Tools & Manufacture. 45 (2005), p. 713

[5] Ting Wang, Dongpo Wang, Yu Shen, Baoming Gong and Caiyan Deng: Journal of Tianjin University. 42(2009), p168(In Chinese)

[6] Ying Lu, Yuping Wang, Hua Li and Hongbin Niu: Modern Manufacture Engineering. 8(2003), p.46(In Chinese)

[7] Binshi Xu: Nano Surface Engineering, edited by Chemical Industry Press, Beijing (2004).

[8] Daoyi Qiu: X-ray diffraction techniques, edited by Sichuan Science and Technology Press,Chengdu(1994).

Advanced Materials Research Vols. 314-316 (2011) pp 33-40

doi:10.4028/www.scientific.net/AMR.314-316.33

Microstructure and Properties of Carbonitride Alloying Self-shielded Wear-resistant Coatings by HVAS

Yu Deng[1,a], Shengfu Yu[1,b], Shule Xing[1,c] ,Linbing Huang[1,d]

[1]College of Materials Science and Engineering, Huazhong University of Science and Technology, Wuhan 430074,China

[a]dengyu200808@163.com, [b]yushengfu@mail.hust.edu.cn

[c]xingshule2002@yahoo.com.cn, [d]huanglinbin88@163.com

Key words: carbonitride alloying; self-shielded flux-cored wire; wear-resistant coatings; high velocity arc spraying; microstructure and properties

Abstract: A kind of self-shielded carbonitride alloying flux-cored wire was developed. Wear resistant coatings was prepared on the surface of the Q235 low-carbon steel by HAVS using the wire. Detection and analysis on the microstructure and properties of the coatings were done by the equipments such as scanning electron microscope, microhardness tester and wear tester. The forming, the wear resistance and its mechanism of the coating were studied. The results show that the coating has good forming property, uniformity of microstructure and compact structure, but the coating also has large oxidate and porosity, this may due to gasforming and slagforming constituents in the wire; the coatings has high hardness, the average microhardness value reachs 510 $HV_{0.1}$, and the highest value up to about 560 $HV_{0.1}$; the coatings has good abrasive wear performance and bonding strength.

Introduction

Preparing high performance wear-resistant coatings on the surface of equipment parts is an effective way to improve the equipment service life. The domestic and foreign researchers developed a variety wear-resistant coatings techniques, one of which was prepared by thermal spraying attracts more and more attention in recently years. Some coatings materials like nano, ceramic, metal ceramic, iron-based amorphous etc, based on supersonic flame spraying, plasma spraying technologies, have been used in production [1-7]. Compared with other thermal spraying, arc spraying begin to be widely used for its advantages as simple device, convenient operation, high efficiency and low cost. The research on wear-resistant coatings made by arc spraying achievement some success. He Ding-yong prepared metal coating and metal-ceramic coating with better erosion resistance at high temperature by arc spraying [8]. Fu Bin-you and others successfully prepared coatings contained some amorphous using arc spraying [9].

Adding. alloy element into flux-cored to form hard particles is one possible solution which can improve the the wear performance. In this study, a kind of self-shielded carbonitride alloying flux-cored wire was developed containing C, N, and some microalloy elements. Self-shielded wire is mainly researched on welding at present [10-11], but the study on the arc sprayed coating with this wire have not been found yet. In this paper, wear resistant coatings was prepared on the surface of the Q235 low-carbon steel by HAVS using the wire. Detection and analysis on the microstructure and properties of the coating were done by the equipments such as scanning electron microscope, microhardness tester and wear tester. and the forming, the wear resistance and its mechanism of the coatings were also studied. These can lay the foundation for further study on such coatings.

Materials and Experiments

Experimental Materials

The coatings were sprayed onto Q235 steel test specimen ($40\times20\times5mm^3$).

Self-shielded cored wire with a diameter of 3.2mm was used to produce coatings, which is carbonitride alloying [12], and its main components are shown in Table 1.

Tab.1 Chemical composition of cored wire(wt%)

C	Si	Mn	Ni	B	Cr	Nb	Ti	V	N	Fe
0.15	0.36	1.35	3.10	2.10	16. 15	0.15	0.52	0.20	0.10	others

Process and Equipment of the Coatings

The arc spraying machine ZPG-400B was used as the arc spraying system.

Oil, grease and rust must be removed, blasting roughening treatment must be done on the sample surface before spraying. The spraying operation was done under the optimized parameters, as shown in Table 2.

The coatings include the base coating and the working coating. the base thickness is 0.2mm made by Ni95Al5 alloy wire, the working thickness is 1.0mm.

Tab.2 Parameters of arc spraying

Spray current /A	Spray voltage V	Air pressure /MPa	Spray distance/mm
180	37	0.6	210

After spraying, heat treatment was done for the coatings: heated 1 hour at 600 ℃, followed by air cooling.

Analytical and Testing Method

Two samples with dimensions of 10×10mm were cut off the surface of coating by Wire Electrical Discharge Machining (WEDM), one for surface observing, and the other for section observing. The specimens were corroded by 4% nitric acid alcohol solution after being inlaid, ground, and polished.

The microstructure and morphology of coatings before and after wear was observed by Quanta 200 Scanning Electronic Microscopy (SEM). The chemical composition of coatings was analyzed by an Energy Dispersive Spectrometer Analyzer (EDS).

The micro-hardness tester(HV-1000) was used to test hardness value of the coating. The testing position was the cross-section, including bottom coating and working coating. Along the direction of bottom coating to woking coating, 10 points were chosen to test the micro-hardness on the load of 100g and hold on 10s.

The abrasive wear test was done by a self-made rubber wheel abrasive wear tester. The coatings were subjected to 10min test using quartz sand. A load of 80 N was applied to the coating, which was rotated at a speed of 100 rpm. Each specimen was weighed before and after the test, using a electronic scale with an accuracy of 0.01g. The observation was measured by the mass losses, and the contrast sample was Q235 steel.

The bonding strength of the coating was tested according to GB/T8642-2002 from < Thermal spraying-Determination of tensile adhesive strength >. The testing equipment is WDW3200 micro control electronic all-powerful tester. During the test, the loading rate was 0.3 mm/min and the beginning load was 10N.

Results and Discussion

Morphology of the coatings

Fig.1 shows the morphology of the coatings surface. There are little gray oxides dispersed in the white metallic structure from the Fig.1. Most of the metal particles deform obviously and become metallic structure of various sizes and shapes after being sprayed on the specimen surface at high speed, and connect with each other. The coating have a good forming.

Section morphology of coatings is shown in Fig.2. The white part near the substrate (Q235 steel) is the base coating which has dense structurer, it bonds closely with the substrate and working coating. Obviously, it is determined by the base coating material Ni95Al5 itself (its properties will be discussed below). Working coating has a typical layer structure, in which flat and irregular metal structure and oxides overlaps each other. The cored wire is melted into droplets heated by arc during arc spraying, then the droplets is

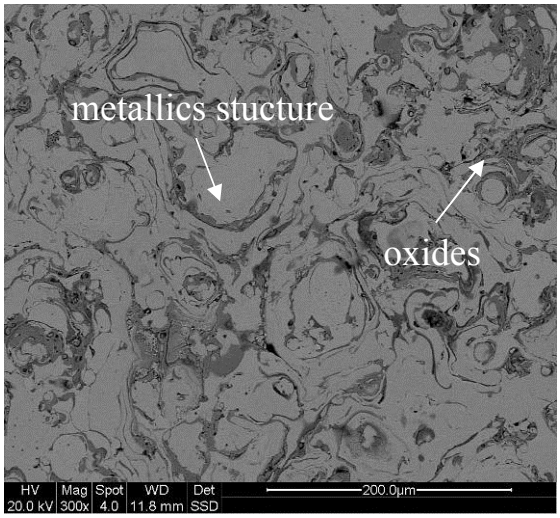

Fig.1 Microstructure of the surface

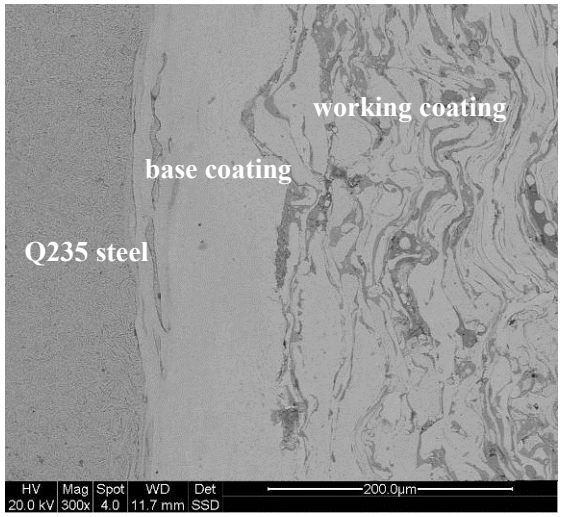

Fig.2 Microstructure of the cross-section

atomized by high pressure air and impacted the specimen surface intensively, and the droplets deposit and solidify layer by layer, finally form a compact coating. The porosity of coatings measured by image analysis software is about 5.72%. The value level is a little higher. It might be related to the gasforming and slagforming constituents in the self-shielded hard-facing cored wire.

Microstructure of the coatings

Fig.3 shows the energy spectrum of the metallic structure. It is comprised of martensite and compound such as carbides and nitrides, and a certain number of oxides. The oxides may mainly come from the following sources: First, the arc spraying equipment had no effective protection for metallurgy process, and it will cause the oxidation of alloy elements. Second, although there are some self-protective elements in cored wires, oxides in the previous coating are covered with the subsequent coating before they are separated out.

As what mentioned before, Cored wires in this test is carbonitride alloying wire. In order to get hardfacing alloy which has high strength and well wear resistance, nitrogen is put into the hardfacing alloy materials instead of a part of carbon, and some microalloy elements such as Nb and V are added to aiming at forming carbonitride. This cored wire has a good result in actual application. Microstructure analysis on the surfacing weld showed that lath martensite and residual austenite existed. Moreover, some ultrafine particles are distributed in grain boundary and on the surface of martensitic. The second phase particles are carbonitride complex, and it might be $Cr_7(C, N)_3$, Ti(C, N), V(C, N), Nb(C, N). The precipitated particles were square and they show typical carbonitride particle feature [13]. The size of carbonitride particles is less than 2μm, and they distribute evenly, so they have good strengthening effect.

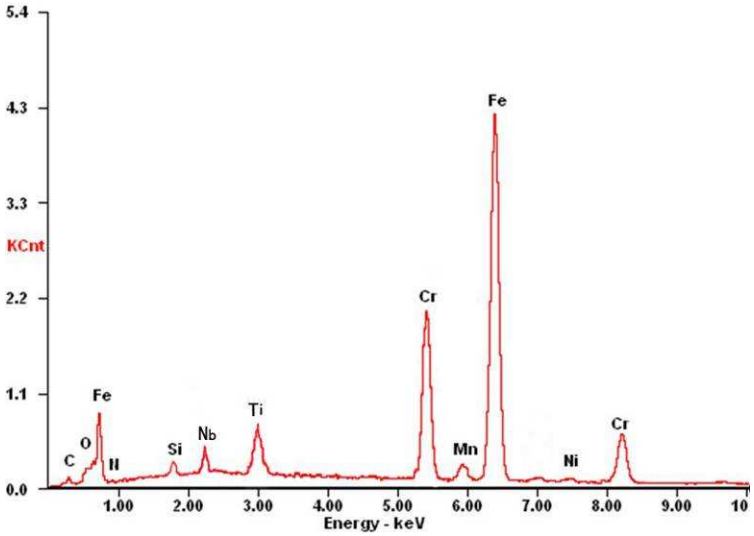

Fig.3 EDS of the coatings

Microhardness of the coatings

Microhardness test was carried out on the cross section of coatings. The results showed in Fig.4 indicate that the average microhardness of coatings reachs 510 $HV_{0.1}$ and the maximum is near 560 $HV_{0.1}$. The microhardness of the base coating is higher than that of pure Ni coating for using Ni and Al alloy., another reason is that high speed droplets of the work coating impact the base coating intensively during spraying, and this wil cause plastic deformation and work hardening of the surface, so the hardness of the base coating is improved. The hardness value of work coating is high and relatively stable, because the work coating of hardfacing alloy material contains hard phase such as carbide and nitride that will improve the hardness of coating. In addition, B and Si have the effect of dispersion strengthening and solid solution strengthening on microstructure. The third reason is that Cr_2B , CrB and carbon in alloy can form carboboride particles.

Abrasive wear performance of the coatings

The wear mass loss of carbonitride alloying coating is 0.319g，while that of the Q235 specimen is 1.162g. It is observed that the wear rate of Q235 specimen is about 3 times of the carbonitride coating, which means the wear-resisting property of self-shielded hardfacing coating is better.

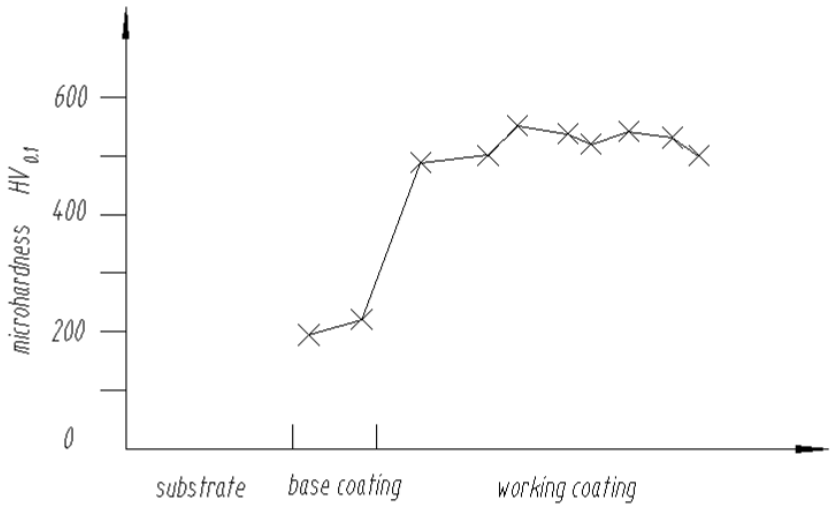

Fig.4 Microhardness of the coatings

The worn surface of coating after abrasive wear is shown in Fig5. Comparing with the Q235 specimen, the depth of wear scar from the worn surface of coating is shallower. Abradability of coating is significantly related to its microstructure and crystal structure. The main reasons why the coating made in this research has higher abradability are explained as follows: First, the structure combined closely not only between coating and coating, but also between coatings and substrate (Q235 steel). Second, the latter coating has the effect of impact hardening on the former coating. Finally, the second phrase particles are the complex which consist of the carbonitrides of Cr, Ti ,V

and Nb can produce precipitation strengthening to the hardfacing alloy. The carbonitrides which precipitated with very fine sizes and distributed homogeneously in the matrix can enhance the abrasive wear resistance of alloy.

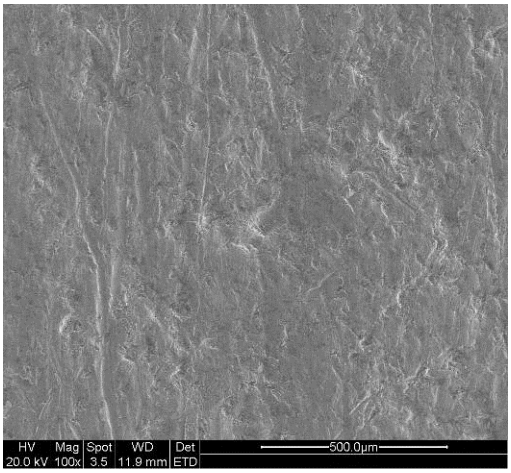

Fig.5 Morphology of the coating after abrasive wear

Bonding strength of coating

Bonding strength is one of the most important factors to determine the coating quality. Coating will peeling , scaling, or even fail for lower bonding strength. The bonding strength of coating tested in this research specially means strength between coatings and substrate (Q235 steel), and its value reachs to 45.8Mpa.

The higher bonding strength of coating is mainly attributed to the following reasons. One is the material NI95Al5 used in base coating has the property of self-felt: The exothermic reaction will occur among the components at high temperature of arc to form intermetallic compounds, and large amount of heat is released so that the surface of substrate is heated up to the molten state, and good metallurgical bonding between the coating and the metal can be obtained .Second, the surface of the self-felt base coating with high roughness can be prepared, which roughness value is even greater than that of pretreatment with sand blasting. Thus the stronger mechanical interlocking between the working coating and base coating can be formed, and is benificial to improve the bonding strength. The third is that the element B and Si in the wire can decrease the melting point of the alloy, widen the temperature range between its solid phase and liquid phase. and the fluidity and wettability of the alloy can be improved. So the bonding between coatings is also improved.

It can be seen from the fracture of tensile specimen that the fracture is occurred at the interface between coatings and substrate. This means, on the one hand, the coatings has excellent bonding strength among themselves, and the cohesive strength of particles in the coatings is higher than the bonding strength of between coatings and substrate. On the other hand, it is also proved the coatings has close structure.

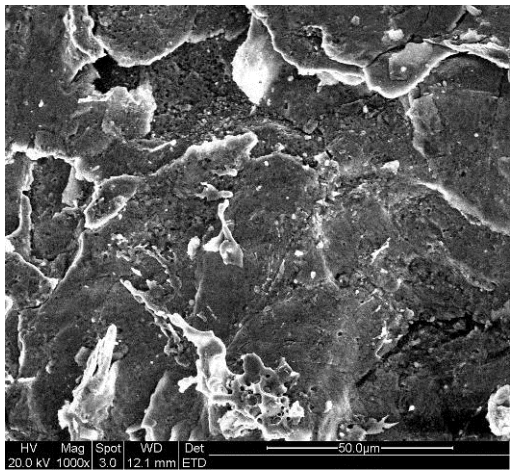

Fig.6 Fracture morphology of the coatings

The pores in the coatings mostly distribute on the boundary between coatings and substrate as shown in Fig.6. It is just the boundary and the place where pores and oxides exist that become the main source of cracking during the fracture process. Obviously, It is a brittle fracture indicated as the fracture. and also shows that the boundary and the place where pores and oxides exist are the area with the weakest bonding strength.

Conclusions

(1) The coating prepared with self-shielded flux-cored wire has good forming property, uniformity of microstructure, compact structure and less porosity. But the composition in the self-shielded wire will increase porosity and oxide.

(2) Higher hardness coatings can be prepared by Arc spraying with self-shielded wire, which average microhardness is 510 $HV_{0.1}$, the maximum value is up to 560 $HV_{0.1}$. The coatings have high abrasive wear resistance.

(3) Because the base coating was prepared, the bonding strength of the coatings in this research is up to 45.8MPa, which can meet the basic requirement of production. But if the bonding strength can be improved further, the coatings would have better service performance.

References

[1] Xun Bin-shi. The basis and applications of the remanufacture engineering.Harbin: Press of Harbin University of Industry, 2005.

[2] Serres N, Hlawka F, Costil S, et al. Combined plasma spray and in situ laser melting treatment of NiCrBSi powder. Journal of Optoelectronics and Advanced Materials, 2010,12(3):505-510.

[3] Tillmann W, Vogli E, Baumann I, et al. Influence of the HVOF Gas Composition on the Thermal Spraying of WC-Co Submicron Powders (-8+1 mu m) to Produce Superfine Structured Cermet Coatings. Journal of Thermal Spray Technology, 2008,17(6).p924-932.

[4] Masahiro Fukumoto. The current status of thermal spraying in Asia. Journal of Thermal Spray Technology,2008,17(1).p7-9.

[5] Y.Ishikawa, S.Kuroda, J.Kawakita etc. Sliding wear properties of HOVF Sprayed WC-20％Cr2-7％Ni cermet coatings. Surf. Coat.Technol,2007,201.p4718-4727.

[6] J.K.N. Murthy and B. Venkataraman, Abrasive Wear Behaviour of WC-CoCr and Cr3C2-20(NiCr) Deposited by HVOF and Detonation Spray Processes, Surf. Coat. Technol., 2006, 200(8),p 648-2650

[7] Zhou Xiao-ping; Hu Xin-bin. Microstructures and Properties of Mo_2FeB_2 Cermets Coating by Reactive Flame Spraying. Surface Technology,2009,38(2).p7-9.

[8] He Dingyong. Study on Arc-Sprayed Cored Wires and Wear Properties of Coatings.Beijing: Press of Beijing University of Technology, 2004.

[9] Fu Bingyou, He Dingyong. Microstructure and properties of arc sprayed coatings containing Fe-based amorphous phase. Transactions of the China Welding Institution,2009,30(4).p53-56.

[10] Menon R. Recent advances in cored wire for hardfacing. Welding Journal, 2002 , 82 (11).p 53-58.

[11] Ke Yang, Shengfu Yu, Yingbin Li, Chenglin Li. Effect of carbonitride precipitates on the abrasive wear behaviour of hardfacing alloy.Applied Surface Science.254(2008),5023~5027.

[12] Ke Yang, Shengfu Yu, Yingbin Li, Pangfeng Tao. New type of carbonitride alloying self-shielded hardfacing flux-cored wires. Journal of Huazhong University of Science and Technology(Nature Science Edition),2008,36（7）.p112~115.

[13] Qingbao Wang, Jing-feng Liu, Feng-gang Shen. Development and property analysis of ultra-low carbon self-shielded flux-cored wire with nitride solid solution strengthening.Welding Journal,2006,27(4).p81-84.

Advanced Materials Research Vols. 314-316 (2011) pp 41-47

doi:10.4028/www.scientific.net/AMR.314-316.41

Investigation of Laser Parameters Influence of Direct-part Marking Data Matrix symbols on Aluminum Alloy

Huadong Qiu[1, a], Wenshuang Bao[2, b], Changhou Lu[1, c], Xueyong Li[1, d]

[1]School of Mechanical Engineering, Shandong University, Jinan, Shandong 250061, China

[2]School of Commerce, University of South Australia, Adelaide, South Australia, 5000, Australia

[a]sonntag@yeah.net, [b]wenshuangbao@126.com, [c]luchh@sdu.edu.cn, [d] lxy88@sdu.edu.cn

Keywords: Laser processing, Optimum laser parameters, Direct-part mark, Data Matrix, Al alloy

Abstract. Different laser parameters and the interactional production can affect the barcode grade profoundly. In order to mark barcodes on aluminum alloy with a laser effectively, it is important to search out the optimum parameters and establish a relationship between critical laser parameters and the quality of the symbol. In this research, a Nd:YAG laser was utilized to produce 3136 Data Matrix symbols onto aluminum substrates. The experiment focuses on all interval values of the vector step, inter-step time, laser Q frequency and laser Q release time. From the experiment results, the optimized parameters are the vector step of 0.005~0.009 mm, the inter-step time of 29~43 μs, laser Q frequency of 7~10 KHz, and laser Q release time of 13~19 μs. And then, by analyzing the higher and the lower power density processing module SEM images and EDS data, it was found that the microstructure and micro-components of formations that created by the interaction between the laser and the aluminum alloy can affect the barcodes grade level significantly.

Introduction

Direct-part marking can solve the problems of missing tags and survived exposure to harsh environments. Laser marking is essentially a thermal process that employs a high-intensity beam of focused laser light to create a contrasting mark on the substrate surface [1]. Comparing to one-dimensional barcode, Data Matrix two-dimensional barcode encode the information in the compact space containing the maximal data with high security. According to the investigation from Ohio University research, Data Matrix barcode can still be accurately located even if it has sustained up to 30% damage as appeared, therefore Data Matrix symbol is an ideal barcode for laser Direct-part marking on the mental surface [2].

Direct-part marking technology cannot be used widely in industrial applications because of the complex interaction between laser and materials. Different laser parameters and the type of material create the different appearances [3]. Data Matrix barcode that has been directly marked, will significant impact the classification of barcodes. During the marking with the laser, complex interaction occurs on the surface of metal. Different laser energy interacts with the metal surface forming a different resultant. By studying the different processing parameters of laser, it will let the laser product the high quality machine-readable tags on aluminum continuously [4]. It will expand the scope of direct-part marking technology for industrial applications. The investigation of the influence between the barcode quality and the composition and microstructure of the resultant can also further understand the laser direct-part marking technology.

The relationship between specific sets of laser parameters and their effect on different substrates has been investigated extensively over the last 20 years. Qi and Leone studied the laser marking on stainless steel. Qi focused on the influence of the pulse frequency of the laser beam on the depth

and width of the mark [5]. Moreover, Leone aimed at pulse frequency, beam scanning speed, and current intensity [6]. Porter discussed the different parameters in laser marking Data Matrix symbol onto carbon steel substrates [7, 8]. He found that contrast and print growth factors limited the laser mark achieving a higher grade. He also analyzes the laser tool path overlap, profile speed, average power, and frequency parameters by using the carbon steel substrates. Hayakawa developed a method by using a Nd:YAG laser to mark bar codes on glass substrates [9]. In his method, bar codes were created by a combination of laser deposition and laser trimming, in order to study the laser power tolerance of the film deposition for code identification was studied.

To conclude based on the literature of the laser marking, the understanding of the physical interaction between light and materials during the marking process plays an important role in the production of laser marks on different types of substrates [3]. The important factors often being investigated include laser parameters (e.g., frequency, power, and scanning speed) and properties of the substrate (e.g., materials chemical composition).

In this paper, a 1064 nm Nd:YAG laser was utilized to produce Data Matrix symbols onto aluminum alloy. The quality of the laser marked Data Matrix symbol was then evaluated according to the ISO/IEC standards for Data Matrix. Parameters such as the vector step, inter-step time, laser Q frequency and laser Q release time were found to have significant effects on the quality of the Data Matrix symbols produced with the laser. By analyzing the higher and the lower power density processing module SEM images and EDS data, it was found that the interaction between the laser and the aluminum alloy explained the laser parameters and materials influence on barcode grade in microstructure and micro-components.

Experimental material, Setup and Methods

Substrate material. Aluminum alloys have a number of desirable features, including low density, high strength-to-weight ratio, excellent casting capability, good machinability and damping characteristics, and they are now increasingly used in aerospace industry, automobile industry, mechanical engineering. Therefore, we chose the aluminum alloy as experimental substrate material. Its thickness was 0.4 mm. The specific components are shown in table 1.

Table 1 Chemical composition of Al-alloy (mass fraction) %

Al	Fe	Si	Cu	Mn	Ti	Mg	Zn
99.48	0.34	0.11	0.016	0.019	0.011	0.002	0.007

Laser parameters setup. A 1064 nm neodymium YAG (Nd:YAG) laser was used to mark the Data Matrix symbols onto the test substrates. The laser average power is 80 w. when the laser current exceeds the material damage threshold, the laser current has a little effect on the barcode grade. The effect of the laser current was investigated via a separate experiment.

Experiment laser is a Q-switched diode pumped Nd:YAG laser. The Q frequency and the Q release time are key parameters, which can adjust the laser energy. Vector step is a single stroke length that divided an entire marking stroke into a number of equal parts. The time that the laser finishes each single stroke is the inter-step time. The adjustable ranges of four parameters and the test's levels selected are shown in table 2. The inter-step time parameters equate the delay of vector step.

Table 2 Experimental parameters of the laser

Laser parameters	Parameters ranges	Selected parameters levels
Q frequency	1~20 KHz	1,4,7,10,13,16,and 19 KHz
Q release time	1~40 μs	1,7,13,19,25,31,and 37 μs
vector step	1~30 μm	1,5,9,13,17,21,25,and 29 μm
the inter-step time	8~60 μs	8,15,22,29,36,43,50,and 57μs

In this research, the INTEGRA 9500 verifier+system was used to determine the quality of laser-marked Data Matrix symbols according to the ISO/IEC 16022 standard [10].

Cleaning process. A cleaning process was employed to remove particle debris after the marking process was complete. The protocol followed for the cleaning process is as follows:

1. Put the barcodes in water for 30 minimums
2. Each barcode is washed five minimums with running water
3. Dry the substrate with pressured air

Experimental methods. The different laser energy achieved by adjusts the laser parameters. It can get the deeply understanding and knowledge about the connection among laser parameters and substrate properties with barcode quality. First, permutation and combination of the four laser parameters can produce 3136 kinds of the laser energy and create 3136 Data Matrix symbols on the aluminum alloy surface. Next, the Data Matrix symbols were evaluated in accordance with the ISO/IEC 16022 standard. Statistical analyses were then conducted to identify the critical parameters in the laser direct-part marking process. This statistical analysis can be divided into two parts. The first part discussed the influence between laser parameters and symbol quality. The second part was based on the resultant analysis. The methodology followed in this research to achieve this goal is depicted graphically in Fig. 1.

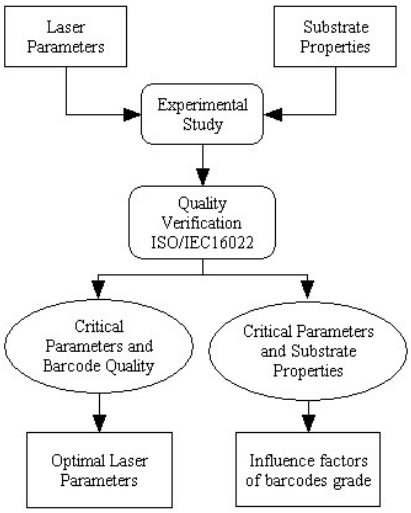

Fig.1 Research methodology to identify critical parameters in lased direct-part marking

Results and Discussion

Experiment results. According to the International Organization for Standardization/International Electrotechnical Commission (ISO/IEC) 16022 standard [10], the quality of a Data Matrix symbol can be divided into five levels that are A,B,C,D, and F. However, this standard was established for printed barcodes. Base on the experimental conditions, we set the barcode as E class, which can be easily observed but cannot be detected by the verifier; set the barcode as G class, which cannot be recognized by the observer and be detected by the verifier. So the barcodes would be classified into seven classes in this experiment. The statistics of the experiment are shown in Table 3.

Table 3 Statistical table of Laser Direct-part Marking Data Matrix Symbols

Data Matrix Barcode Grade	Number of Barcode	Percentage (%)
A	12	0.382653
B	178	5.67602
C	221	7.047194
D	231	7.366071
F	299	9.534439
E	496	15.81633
G	1699	54.1773
Total	3136	100

Laser parameters analysis. Four laser parameters were merged into two parameters based on the physical meaning. Scanning speed is the vector step divided by the inter-step time. Q frequency multiplied by Q release time is the laser energy. In this experiment, the laser current did not change, so consider this product as laser energy. In proper order numbers for graphic display replaced barcodes quality levels. Combined parameters and the barcodes grade distribution are shown in fig.2.

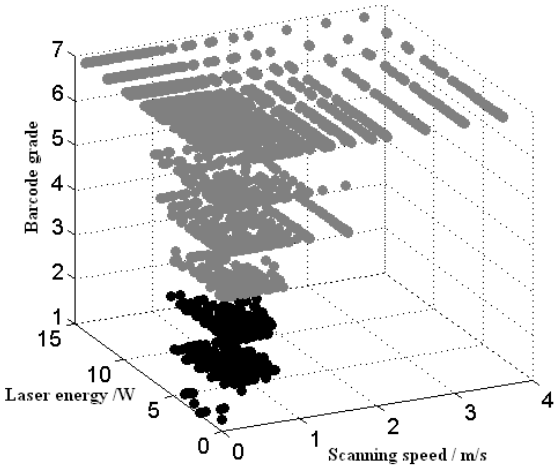

Fig.2 Distribution of the lased barcodes

Fig.2 shows the overall barcodes quality distribution. Number 1 represent A class of barcode quality level, and number 6 is F class. It can clearly be observed that the higher grade barcodes were all appear in lower scanning speed and lower laser energy area. The A class barcodes appears in the range of laser scanning speed 0.03448~0.8056 m/s and laser energy 1.26~4.5 w.

In above-mentioned ranges, the Q release time and the inter-step time parameters were plotted against the barcodes grade separately. The results are shown in Fig.3 and Fig.4.

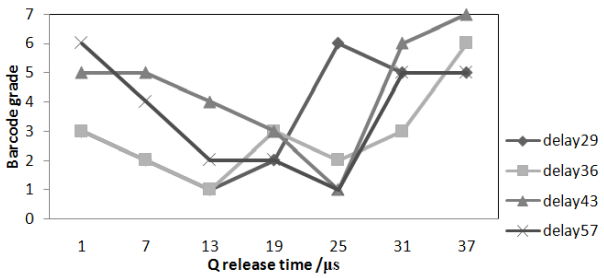

Fig.3 Q release time and barcode grade

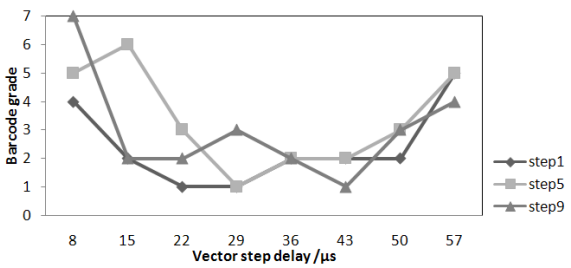

Fig.4 Delay of vector step and barcode grade

Fig.3 shows the relationship between the Q release time and barcodes grade under the condition of Q frequency is 10 KHz and vector step is 9 μm. Four curves are drawn under the inter-step time are 29, 36, 43, and 57 μs. The same regulation is indicated by the four curves. With the Q release time increasing, the barcodes grade level appears increased first, and then decreased. Two curves, which the inter-step time is 29 and 36 μs, achieve the highest level of barcodes grade when the Q release time is 13 μs. When the Q release time is 25 μs, two curves which the inter-step time is 43 and 57 μs also got the highest level. This indicates that reduce the laser scanning speed must increase the laser energy to keep the barcodes in same grade level. The two curves of 29 and 36 μs have a little fluctuation range than the 43 and 57 μs. It indicates that the higher laser scanning speed is useful for getting the high-quality barcodes grade level in the same vector step.

Fig.4 shows the relationship between the inter-step time and barcodes grade under the condition of Q frequency is 10 KHz and Q release time is 9 μs. Three curves are drawn under the vector step are 1, 5, and9 μm. Same discipline is clearly observed between the inter-step time and the Q release time. As the inter-step time increased, the barcodes grade level appears increased first and then decreased. In addition, as the vector step increased must increase the inter-step time at the same time in order to obtain a higher barcodes grade level.

The inter-step time and the Q release time are the same order of magnitude. The influence between this two of parameters is much more complex. To achieve the high-quality barcodes grade level the inter-step time and the Q release time must be carefully selected. In the experiment, all A class level of barcodes are created at 7 and 10 KHz of the Q frequency.

In summary, the range of laser scanning speed 0.03448~0.8056 m/s and laser energy 1.26~4.5 w are optimal region. The optimized parameters are the vector step of 0.005~0.009mm, the inter-step time of 29~43μs, laser Q frequency of 7~10 KHz, and laser Q release time of 13~19μs.

Resultant analysis. The scanning electron microscope (SEM) and Energy Dispersive Spectrometer (EDS) were used to analyze the black and white appearance barcodes in microstructure and composition. Figure 5 depicts pictures of a sample laser marked Data Matrix symbol with 300X magnification.

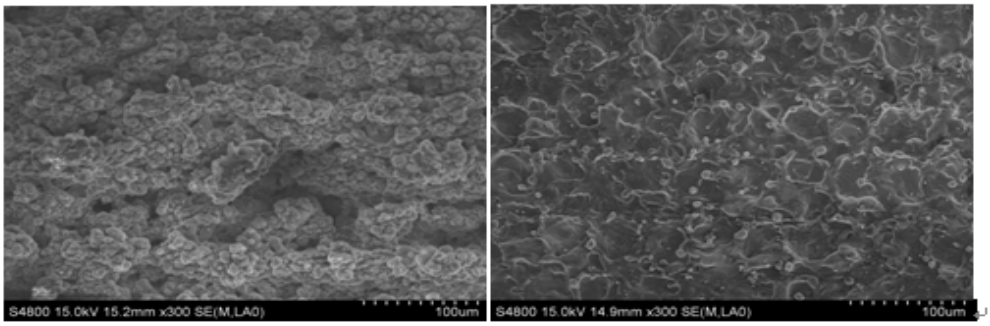

Fig 5 SEM photographs (300X) of the high (left) and (right) low energy density

Fig.5 (left) is the black appearance symbol SEM photograph. The barcode was created by using the vector step of 1 μm, the inter-step time of 50μs, laser Q frequency of 13KHz, and laser Q release time of 31μs. The laser line power density is 70.434 w/m. The Fig.5 (right) is the white appearance symbol SEM photograph. The barcode was created by using the vector step of 5 μm, the inter-step time of 29μs, laser Q frequency of 10KHz ,and laser Q release time of 13μs. The laser line power density is 3.544 w/m. whereas those surface EDS analysis results are shown in Table 4.

Table 4 EDS analysis of barcode module (mass fraction) %

Elements	high energy density	low energy density
O	32.73	7.31
Al	29.80	78.99
Si	0.44	
Fe	0.28	

The remaining mass fraction is carbon created by instrument background.

The Fig 5 shows two different microstructures. The lower laser energy's resultant has an obvious compact structure than the higher laser energy. The spherical tissue can be easily observed in Fig 5 (right). Al_2O_3 clusters like a string of pearls in the aluminum oxide [11]. Based on the EDS results in Table 4 and Fig. 5, it can be assumed the resultant that low-power laser created is mainly aluminum and its' oxide. The aluminum, its' oxide and compact structure give the symbol white appearance.

The situation becomes more complicated when the laser working in high-energy. First the higher laser energy's resultant has much higher oxidation than the lower laser energy, as shown in Table 4. When the aluminum alloy contains less iron and silicon elements, the silicon can be emerged into the body, and the iron can become the needle-like Al_3Fe phase. It can be a ternary compound when iron and silicon elements have enough contents. The ternary compound is the bone-like α ($Al_{12}Fe_3Si$) phase when the iron elements have the many contents than silicon and the β ($Al_9Si_2Fe_2$) phase appears in the condition that the silicon elements have the many contents than iron [12]. Table 1 shows that the iron elements have the many contents than silicon but the EDS result gives the completely opposite percentage of the mass fraction as shown in Table 4. This indicates the resultant present complex morphology when the laser in high-power energy marking. The higher laser energy's resultant shows the larger pores' structure than the lower laser energy as shown in Fig 5 (left). It can be assumed the resultant that high-power laser created is the complex oxides of aluminum ferrosilicon. The complex oxide and larger pores' structure gives the symbol black appearance.

In summation, the laser of the different energy interacts with the surface metal and forming a different resultant. The microstructure and micro-components of formations that created by the interaction can affect the barcodes grade level significantly and determine the barcodes grade level.

Conclusions

The experiment results and analyses show that Data Matrix symbols produced with a laser on aluminum alloy give good quality based on the laser Parameters, the composition and microstructure of the resultant that form by laser-material.

(1). An accurate range of the laser parameters were given to create higher grade Data Matrix two-dimensional barcodes on aluminum alloy surfaces.

(2). By analyzing the higher and the lower power density processing module SEM images and EDS data, it was found that the resultant that form by laser and the materials interaction effect the barcode grade in microstructure and micro-components.

This research provides a better understanding and knowledge on the laser direct-part marking on aluminum alloy and also given a useful range of laser parameters that can help direct-part marking technology apply in industrial applications.

Acknowledgements

The financial support of the Shandong Province Foundation for Excellent Young and Middle-aged scientists of (No: BS2010ZZ007) is grateful.

References

[1] R. C. Palmer: *The Bar Code Book* (Helmers Publishing Press, Peterborough NH 2001)
[2] Information on http://www.ohio.edu/industrialtech/aidc/activities/research.cfm
[3] NASA: *Application of Data of Data Matrix Identification Symbols to Aerospace Parts Using Direct Part Marking Methods/Techniques* (NASA Press, Washington DC 2002)
[4] T. J. McKee: Electro technology, Vol. 7 (1996). P. 27
[5] J. Qi, K. L. Wang, Y. M. Zhu: Materials Processing Technology, Vol. 139 (2003), p.273
[6] C. Leone, S. Genna: Materials Processing Technology, Vol. 210 (2010), p.1297
[7] J. David Porter: Manufacturing Science and Engineering, Vol. 129 (2007), p.583
[8] J. David Porter: Journal of Intelligent Manufacturing, Vol. 17 (2006), p.133
[9] H. Hayakawa: First International Symposium on Laser Precision Micro fabrication, Vol. 4088 (2000), p.363
[10] ISO: *ISO/IEC 16022:2000 Information technology -- Automatic identification and data capture techniques -- Bar code print quality test specification -- Two-dimensional symbols* (ISO Press, Geneva, Switzerland 2004)
[11] Z. T. Huang: *Catalysis* (Chemical Industry Press, Beijing 2006) , In Chinese
[12] J. H. Li: *Metal Metallographic Map* (Mechanical Industry Press, Beijing 2006) , In Chinese

Advanced Materials Research Vols. 314-316 (2011) pp 48-52

doi:10.4028/www.scientific.net/AMR.314-316.48

Curvature Testing the Residual Stresses in 3%TiO_2-Al_2O_3 Coatings by Thermal Spraying Technology

MEI Fang[1, a], GONG Manfeng [1,b]

[1] Institute of physical science and technology, Zhanjiang Normal University, Zhanjiang 524048

[a]meif@sina.com, [b]gongmanfeng@163.com

Keywords: 3%TiO_2 -Al_2O_3 coatings, Stainless steel, Residual stress, Curvature method, Thermal spraying technology

Abstract: Plasma thermal spraying technique was adopted to deposit five groups of different thickness 3% TiO_2-Al_2O_3 coatings on 329-Stainless steel. A curvature method was applied to study the residual stresses. Results showed that the deformations corresponding to 3% TiO_2-Al_2O_3/329-SS systems were serious. The residual stress changed with the ξ (ratio of coatings' thickness to substrate's thickness) value and weren't constants for the coatings' thickness 52-306 μm. No regardless of using the Stoney' or Tomanov' formula to calculate the residual stresses, which decreased with the ratio ξ value increased, and the thinner coatings were, the greater the residual stresses were. The coatings' residual stresses changed with the ξ value at an exponent relation. The coatings' thickness affects greatly on their residual stresses, especially for the intrinsic stresses. When the coatings thickness changes from 52 to 306 μm, the residual stresses were always compressive stresses. The maximums residual stresses were caused when the ξ value is 0.115 (the minimum value), and the details were -584.96 MPa and -482.78 MPa by two difference formulas, respectively.

Introduction

The thermal spray process is one of the most versatile hard facing techniques available for the application of coating materials used to protect components from abrasive wear, adhesive wear, erosive wear or surface fatigue and corrosion [1]. Thermal barrier coatings (TBCs) are currently applied on gas turbine blades and diesel engine components. TBC concept provides a means of raising the operating temperature by enabling the underlying metallic components to operate at lower temperature due to the temperature gradient across the thick ceramic coating, and thus permit performance increases without requiring major alloy development [2]. TBCs are known for the high hardness and remarkable tribological properties, making them suitable for industrial applications [3].

However, the work carried out so far did not consider yet an important aspect of thermal spraying technology, which is surface residual stress, an essential parameter in industrial design, significantly affecting the fatigue life of coated parts [4]. For this reason, research work dealing with the characterisation of residual stresses in thermally sprayed coatings is of significant relevance. The numerous methods available for the characterisation of residual stresses (including, for instance, hole drilling [5], curvature methods[6], neutron diffraction[7], Raman spectroscopy[8], use of synchrotron radiation [9], X-ray diffraction methods[10], layer removal techniques[11], etc.). It is one of the most efficient motheds for testing surface residual stress by curvature motheds, which are widely accepted in the academia and engineering fields [12]. The advantages of the curvature method are simple and valid, and that don't destroy the specimen in the testing process. However the disadvantage is that the curvature method can only obtain the average residual stress, which distributes in the coating. In recent years, it was reported that the application range was expanded and the disadvantage were improved by combining curvature method and others testing approaches, for instance, combining the curvature with the X-ray diffraction [13], synchrotron radiation [14], layer removal techniques [11], and finite element method [15], etc. It can not only study the relationship of residual stress change with coating thickness, but also improve greatly the measurement accuracy, that improves the measurement magnitude to km.

For alumina coatings, residual stress limits the thickness of the deposit achieved by causing adhesion loss between the deposit and its base material, interlaminar debonding, crack formation and buckling. Residual stresses are known to play an important role in coating durability. This paper aims at performing such characterisation by combining experimental and analytical approaches. The residual stress and its dependence on deposit thickness were characterized. The in-situ curvature measurements were adopted in the present study, and were coupled to analytical model, based on the Stoney-Tomanov theory [16,17].

Experimental

Substrate material preparation. The 329-stainless steel (329-SS, thickness is 0.450 -0.470 mm) metallic substrates adopted here were strips (70 mm × 8 mm), which were processed by a line cutting technology. The 304-SS (thickness is 3 mm) were processed similarly to be the single face deposited holder by line a cutting technology, having the top-layer and the sub-layer and a rectangle open slot (120 mm×60 mm) in top-layer. The strip specimen were fixed carefully by nuts before depositing coatings, Fig.1 was the sketch of installing specimens before depositing coatings.

Coating material preparation. The single-face ceramic coating (3%TiO_2- Al_2O_3) processes were carried by a plasma thermal spraying techniques, and the main processes were divided into five stages, such as specimen surface pretreatment, preheat, spraying underlayer powders, spraying work-layer powders, coatings aftertreatment. Thermal spraying technology parameters of the pressure, flow (oxygen gas, acetylene gas and nitrogen gas) are shown in table 1.

Table 1. Thermal spraying technology parameters.

Gas types	Pressure/(MPa)	Flow/(m^3/h)	Spraying distance/(mm)	Nozzle length/(mm)
acetylene	0.05-0.1	-1.8		
oxygen	0.3-0.6	-1.2	-180	150-300
nitrogen	0.5-0.6	60-75		

There were 10 substrate specimens, applied 329-SS material. They were divided into 5 groups (5 specimens in one group) to spraying, and the same group specimen, the same coatings thickness. The 3% TiO_2-Al_2O_3 residual stress final specimen are shown in Fig.2 after thermal spraying.

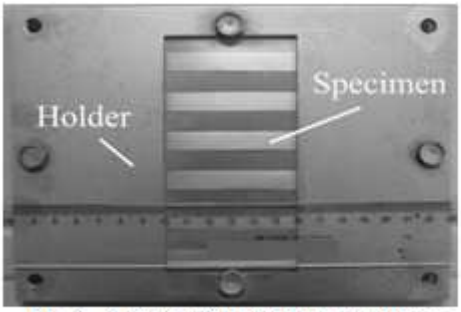

Fig.1. Sketch of installing specimens before depositing coatings.

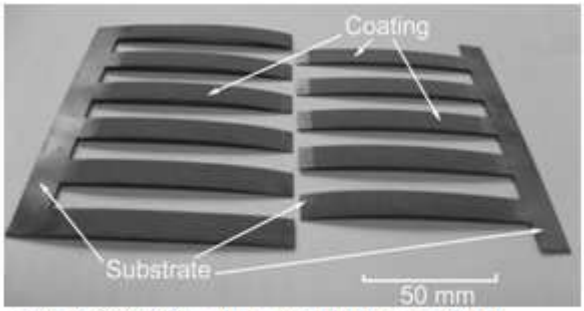

Fig.2. 3% TiO_2-Al_2O_3 residual stress final specimen

Curvature method. The coating and substrate systems curve under residual stress. Tension residual stress in coatings protrudes the systems to the substrate direction when the coefficient of thermal expansion of coating material is greater than that of substrate material ($\alpha_{co}>\alpha_o$), and compressive residual stress protrudes the systems to the coating direction at $\alpha_{co}<\alpha_o$. The situation in this paper corresponded to the latter because studying the ceramic coatings and metallic substrate systems.

When the thickness of coating is very thin and less than that of substrate so far, the residual stress in substrate can be ignored. The residual stress in coating caused by some factors, such as phase transition and plastic deformation and so on is small at present and the thermal residual stress is main, that is ascribed to the difference of the physical properties between coatings with substrate material. Once the specimens bended under residual stress, their curvature radius, chord length and arch-high satisfied the definite relation.Tomanov [17] introduced the following formula to calculate the coating's residual stress,

$$\sigma_{co}^{res} = \frac{4E_oH^3 f}{3a^2(1-\mu_o)(H+h)h} \quad (1)$$

Where E_o (GPa) is the elastic modulus of substrate material, h and H (mm) are the thickness of coating and substrate, respectively. μ_o is the Possio' ratio of substrate material. the ξ is the ratio between the coating thicknesses h with the substrate thickness H. Here assuming E_o = 400 GPa, u_o = 0.30. The formula (1) can be come down to the following Stoney′s formula [16], when the thickness of coating is smaller so far than that of substrate.

$$\sigma_{co}^{res} \approx \frac{E_oH^2}{6Rh} \quad (2)$$

There are three essential conditions causing the thermal residual stress in the coating and substrate systems, firstly, the interface between coating and substrate bond well. Secondly, the temperature changes corresponding from start to finish spraying. Thirdly, the differences should lie corresponding to the thermal physical properties. The shear stress generates between the interfaces of coating with substrate if providing these three conditions. So the coating and substrate systems bend, and the main theory of curvature method is to calculate the residual stress by testing the curvature radius.

Results and discussion

Residual stress results. The coating and substrate system (3% TiO_2-Al_2O_3 / 329-SS) deformed seriously. Table 2 shows the residual stress results of thermal spraying 3% TiO_2-Al_2O_3 / 329-SS by curvature method.

Table 2. Residual stress results of thermal spraying 3% TiO_2-Al_2O_3 coatings by curvature method.

Coating thickness h/(mm)	Substrate thickness H/(mm)	Coating substrate ratioξ	Chord length a/(mm)	Arch-high f/(mm)	Curvature radius R/(mm)	Residual stress σ_{co}^{res} /(MPa)	
						Tomanov′formula	Stoney′formula
0.172	0.463	0.371	59.94	2.01	222.74	-292.72	-297.08
0.180	0.450	0.400	59.90	2.20	202.86	-283.95	-294.17
0.107	0.465	0.230	59.90	1.45	309.44	-381.73	-347.48
0.156	0.466	0.335	59.84	1.95	229.04	-326.78	-322.77
0.052	0.451	0.115	59.70	1.03	431.60	-584.96	-482.78
0.126	0.460	0.274	59.94	1.71	261.40	-362.29	-341.53
0.149	0.464	0.321	59.92	1.94	230.27	-340.89	-333.26
0.201	0.458	0.439	59.98	2.45	182.42	-284.65	-303.08
0.265	0.460	0.576	59.94	2.76	161.34	-224.40	-261.72
0.080	0.464	0.172	59.78	1.22	366.48	-450.67	-391.00
0.120	0.458	0.262	59.90	1.55	287.73	-346.01	-323.14
0.180	0.462	0.389	59.90	2.11	211.07	-289.92	-298.13
0.285	0.465	0.613	59.84	3.12	141.90	-236.31	-282.05
0.306	0.464	0.659	59.70	3.24	135.88	-222.23	-272.90
0.160	0.464	0.345	59.94	2.04	219.50	-327.02	-325.44

The 3% TiO_2-Al_2O_3 / 329-SS system deformed, and their deformed arch-high and chord length, changed with the Coatings substrate ratio ξ value, weren't constants for the coatings' thickness 52-306 μm, corresponding to the table data. The residual stresses in 3% TiO_2-Al_2O_3 coatings were compressive stresses. The maximums residual stresses, emerging at ξ=0.115 (the minimum value among the table 2), were -584.96 MPa and -482.78 MPa by two difference formulas, respectively.

Influence of the ξ value to residual stress. Fig.3 shows the relationships of arch-high and curvature radius changing with the ξ value in 3% TiO_2-Al_2O_3/329-SS systems. The arch-high f increased with the ratio ξ value increased, but the curvature radius R decreased with that. The thicker coating was, the more serious the deformation was.

The curvature radius R changed with the coatings substrate ratio ξ value, and two parameters had the exponent relation, which corresponded to the following formula by mathematic fitting.

$$R(\xi) = 542.798 \exp(-\frac{\xi}{0.224}) + 110.170 \quad (3)$$

But the arch-high f changed linearly with the coatings' substrate ratio ξ. the following formula was given by mathematic fitting.

$$f(\xi) = 0.5532 + 4.0843\xi \quad (4)$$

Fig.4 shows the relationships between the residual stress and the ξ value in 3% TiO_2-Al_2O_3 / 329-SS systems. Similarly, the residual stress changed with the ξ value and weren't constants for the coatings' thickness 52-306 μm. No regardless of adopting the Stoney' formula or Tomanov' formula, the residual stresses decreased with the ratio ξ value increased, and the thinner coatings were, the greater the residual stresses were.

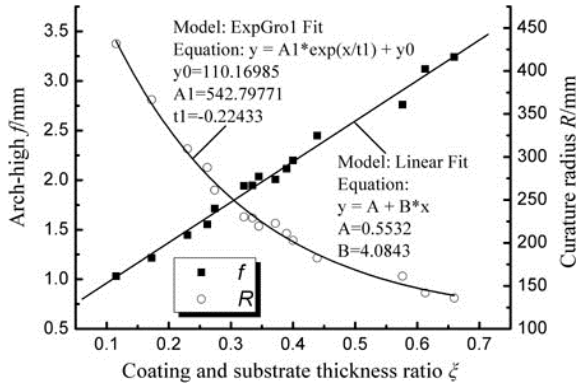

Fig.3. Relationships of the arch-high and the curvature radius changing with the ξ value in 3% TiO_2-Al_2O_3 coatings.

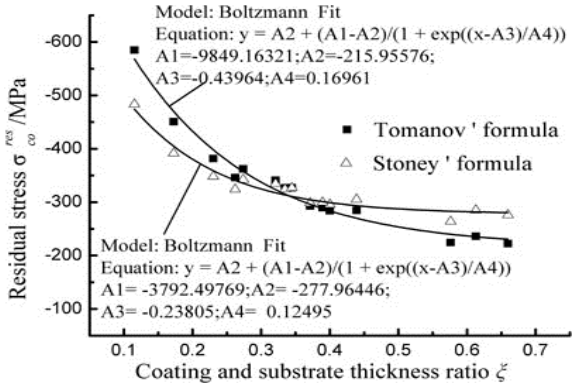

Fig.4. Relationships between the residual stress and the ξ value in 3% TiO_2-Al_2O_3 coatings.

Here, the fitting results of residual stresses were given by combining the Stoney' formula and Tomanov' formula. According to the Stoney' formula, the fitting relation was

$$\sigma_{co}^{res}(\xi) = -277.964 + (277.964 - 3792.498)/[1 + \exp(\frac{\xi + 0.238}{0.125})] \quad (5)$$

However, the fitting relation was shown as following formula by the Tomanov' formula.

$$\sigma_{co}^{res}(\xi) = -215.956 + (215.956 - 9849.163)/[1 + \exp(\frac{\xi + 0.440}{0.170})] \quad (6)$$

It was concluded that the coatings' residual stresses changed with the ξ value and two parameters always had the exponent relation.

Conclusions

The residual stresses in the 3% TiO_2-Al_2O_3/329-SS systems were succeeded to be tested by curvature method, and the residual stresses were compressive stresses. The maximums residual stresses were caused when the ξ value is 0.115 (the minimum value), and the details were -584.96 MPa and -482.78 MPa by two difference formulas, respectively.

The deformations corresponding to 3% TiO_2-Al_2O_3/ 329-SS systems were serious, that proclaimed that the residual stresses in the systems were great. The residual stress changed with the ξ value and weren't constants for the coatings' thickness 52-306 μm. No regardless of using the Stoney' or Tomanov' formula to calculate the residual stresses, which decreased with the ratio ξ value increased, and the thinner coatings were, the greater the residual stresses were. The coatings' residual stresses changed with the ξ value at an exponent relation.

Acknowledgements

This research was funded by the National Natural Science Foundation of China under the contracts 50772089, the National Natural Science Foundation of Zhanjiang normal university under the contracts ZL0903 and Program of Zhanjiang financial compe- titiveness distribution under the contracts 201004. The authors would like to thank Professor Shengru Qiao and Zhong Li for their help in residual stress and coating thickness measurements, respectively.

References

[1] J. Stokes, L. Looney: Surface and Coatings Technology Vol. 177–178 (2004), p. 18
[2] M. Lugovya, V. Slyunyayeva, V. Teixeirab: Surf. Coat. Technol Vol. 184 (2004), p. 331
[3] G. Bolelli, L. Lusvarghi, M. Barletta: Surface and Coatings Technology Vol. 202 (2008), p. 4810
[4] J.A. Marin de Camargo, H.J. Cornelis: Surf. Coat. Technol Vol. 201 (2007), p. 9448
[5]G. Montay, A. Cherouat, J. Lu: Surface and Coatings Technology Vol. 155(2002), p.152
[6] Y. T. Yu, W. Z Yuan, D. Y Qiao: Journal of Mechanical Engineering Vol. 43(2007), p. 78
[7] R. Ahmed, V. Stoica, J. R. Santisteban: Materials Sci. and Eng. A Vol. 498(2008), p. 191
[8] H. Wu, Y.G. Meng, C. J. Su: Journal of Mechanical Strength Vol. 29(2007), p.233
[9] H. Lu, X. S. Liu, Z. Zhu: Journal of Mechanical Engineering Vol. 21 (2008), p. 91
[10] C. Quaeyhegens, G. Knuyt, L. M. Stals: Surf. Coat. Technol Vol. 74-75(1995), p. 104
[11]E. Heyen, O. Bauer: International Zeitschrift Fur-metallographic Vol., 1(1911), p.16
[12] B. A. Lyashenko, A. V. Ruthovskii, E. B. Soroka: Strength of materials Vol. 33(2001), p. 344
[13] C. Mendibide, P. Steyer, C. Esnouf: Surface and Coatings Technology Vol. 200(2005), p. 165
[14] M. F. Doerner, D. S. Gardner, W. D. Nix: J. Mater. Res. Vol. 1(1986), p. 845
[15] E. Celik, O. Sarikaya: Materials Science and Engineering A Vol. 379(2004), p. 11
[16] G. G. Stoney: Proc. Roy. Soc., London, Ser. A Vol. 82(1909), p. 172
[17] A. T. Tomanov, Methods for Testing, Evaluation and Investigation of Engineering Materials (Moscow Publications, Mashinostroenie 1974)

Advanced Materials Research Vols. 314-316 (2011) pp 53-57

doi:10.4028/www.scientific.net/AMR.314-316.53

Surface Properties of TiN Films on AZ 31 Magnesium Alloys Deposited by Magnetron Sputtering technique

Xiangrong Zhu[1,2, a], Naici Bing[1,b], Zhongling Wei[2,3,c] and Qiurong Chen[2,3,d]

[1]School of Urban Development and Environmental Engineering, Shanghai Second Polytechnic University, Shanghai 201209, China

[2]Jiaxing Engineering Technology Centre of Light Alloy Metals, Chinese Academy of Sciences, Jiaxing 314051, Zhejiang, China.

[3]Shanghai Institute of Microsystem and Information Technology, Chinese Academy of Sciences, Shanghai 200050, China

[a]zhuxiangrong71@126.com, [b]ncbing@eed.sspu.cn,

[c]zlwei@mail.sim.ac.cn, [d]qrchen@mail.sim.ac.cn

Keywords: Magnesium alloy, Magnetron sputtering, Surface properties, TIN films.

Abstract. TiN films were deposited on the AZ 31 magnesium alloy substrates by d.c. magnetron sputtering technique. The surface properties of the films were investigated. The scanning electronic microscope observations reveal the dense structure characteristics of as-deposited TiN films. Under 200°C heat treatment for 30 minutes or 4 times' heat cycles at 85°C for one hour, no structural defects such as cracks are observed on the surface of the films. Adhesion experiment further demonstrates the stability of the film and the strong combination between the film and the substrate. Nano-indentation experiment shows that the average micro-hardness of TiN film reaches 23.85 Gpa. Finally, the corrosion experiments in simulated body fluid initially reveal the degradation property of TiN film.

Introduction

On the one hand, magnesium alloys have been widely used in industrial field as excellent light metal structural materials [1-3]. On the other hand, due to non-toxic properties, magnesium alloys are bringing forth wonderful expectations on the application of medical field [4, 5]. However, conventional magnesium alloys usually present poor surface properties such as poor corrosion resistance and low temperature stability, which would greatly limit their further application [6-8]. Thus the surface modification of magnesium alloy should be considered.

Multiple approaches are explored to the surface modification of magnesium alloy, including magnetron sputtering [1], microarc oxidation [2], cathodic arc deposition [7], etc. Of these approaches, magnetron sputtering is convenient and economy. The films deposited by magnetron sputtering usually present good uniformity. Due to high hardness and non-toxic properties, TiN film becomes an attractive choice for surface modification of magnesium alloy. Many studies on structure and mechanics properties of TiN film deposited on magnesium alloys have been reported. However, reports about detailed surface properties of TiN film on magnesium alloy are few.

In this paper, the surface properties of TiN films on AZ31 magnesium deposited by d.c.magnetron sputtering are investigated in detail, including temperature stability, adhesion property, surface micro-hardness and corrosion in simulated body fluid.

Experimental

AZ 31 is one kind of widely used wrought magnesium alloys. In this paper, five 1 cm × 1 cm AZ 31 magnesium alloy chips about 2 mm high were used as substrates of the samples, which were provided with by Jiaxing Engineering Technology Centre of Light Alloys Metals, Chinese Academy of Sciences. The chips were firstly polished by one mechanical polishing machine using corundum abrasive and then cleaned by one ultrasonic cleaner. The dried chips were fixed onto the sample

holder in the cavity of the magnetron sputtering equipment. The base pressure of the cavity was 5×10^{-4} Pa. The sputtering atmosphere was mixed with 1:1 Ar and N_2 and the working pressure remained 0.5 Pa. The sputtering target was 99.95% TiN ceramic disc. During the sputtering, the substrates were not heated. The d.c. sputtering power and time reached 120 W and 50 minutes, respectively.

The samples were marked with TiN 1#, TiN 2#, TiN3#, TiN4# and TiN 5#, respectively, for characterizations of different properties. Firstly for each as-deposited sample, the surface morphology was observed by one scanning electronic microscope (SEM). Then TiN 1# and TiN 2# samples were used for heat stability experiment. For TiN 1#, the heat treatment technique 1 was that the sample was kept in the oven under 200°C for 30 minutes and then removed from the oven and cooled in the air. For TiN 2#, the heat treatment technique 2 was that the sample was kept in the oven under 85°C for one hour and then removed from the oven and cooled for 15 minutes in the air. These steps were repeated for 3 times. For the samples after the above heat treatment techniques, the surface morphology was observed by SEM.

Secondly, the adhesion experiment was conducted on TiN 3# sample. The surface of the TiN film was manually ripped by one medical cleavage knife into 8×8 grids. One piece of 3M tape was tightly adhered onto the surface of the film and then manually torn off from the surface of the film. The surface morphology of TiN 4# film before or after adhesion experiment was observed by one optical microscope.

Thirdly, the TiN 4# sample was used for characterizing the surface micro-hardness of TiN film by one nano-indenter.

Finally, the TiN 5# sample was put into one bottle of Hank's simulated body fluid (SBF) for the study of corrosion behavior. The composition of SBF was NaCl (8.00g) + KCl (0.40g) + $CaCl_2$ (0.14g) + $NaHCO_3$ (0.35g) + $MgCl_2 \cdot 6H_2O$ (0.1g) + $MgSO_4 \cdot 7H_2O$ (0.06g) + KH_2PO_4(0.06g) + $Na_2HPO_4 \cdot 12H_2O$ (0.06g) + H_2O (1L) [4]. After 7 days' corrosion, the sample was removed from the bottle and washed by cleaning solution mixed with CrO_3 and $AgNO_3$ [4]. The surface morphology of the corrosion sample was also observed by SEM.

Results and discussion

All the as-deposited TiN films on the substrates look golden. X-ray diffraction patterns of the films present typical TiN polycrystalline structure.

Fig. 1 exhibits the surface morphologies of TiN 1# film before and after heat treatment under technique 1. The SEM displays that the as-deposited film is composed of uniformly distributed grains and the surface seems dense. After heat treatment under 200°C for 30 minutes, the grains become a bit larger. Although the film was cooled in the air, no defect such as cracks is observed on the surface and the surface keeps dense.

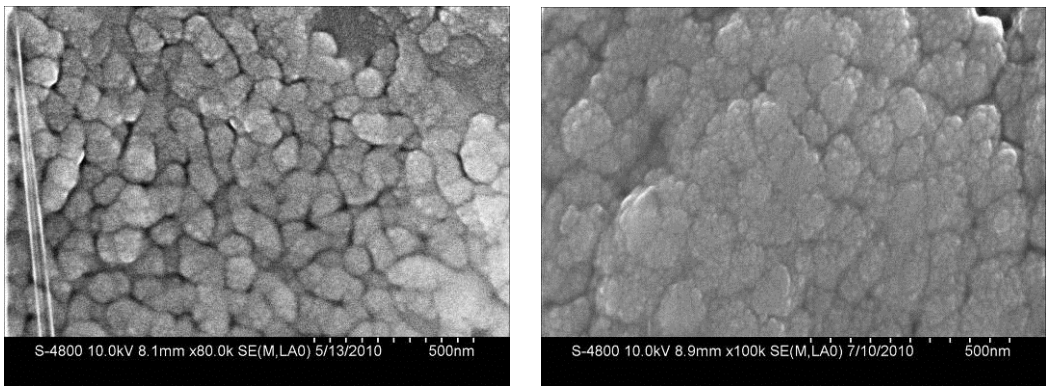

Fig. 1 The surface morphology images of TiN 1# film observed by SEM (Left: as-deposited , right: heated under technique1)

The surface morphologies of TiN 2# film before and after heat treatment under technique 2 are shown by Fig. 2. The as-deposited TiN 2# film presents similar surface morphology characteristics to as-deposited TiN 1# film. After heat treatment under technique 2, little change of the size of grains is presented in Fig. 2, implying that low heat treatment temperature under 85°C would not change the distribution and size of grains. Furthermore, no defects such as cracks are observed on the surface of the heated film, which keeps dense.

From the above heat treatment experiment results, it could be deduced that TiN film presents certain stability whether it is heated under 200°C for 30 minutes or it suffers from 4 times' heat cycles under 85°C for one hour.

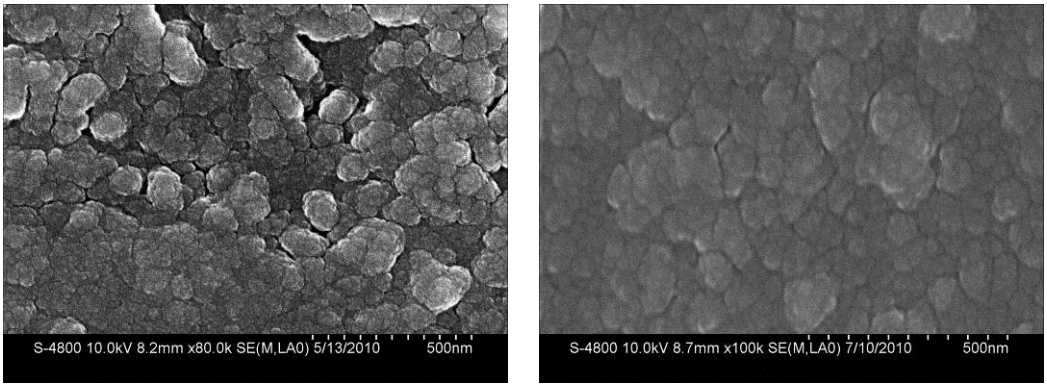

Fig. 2 The surface morphology images of TiN 2# film observed by SEM (Left: as-deposited , right: heated under technique2)

Fig. 3 presents the surface morphologies of TiN 3# film before and after adhesion experiment. The magnification rate of the optical microscope is 8 ×. Before adhesion experiment, no tape is covered on the surface of the sample and the surface is clean. When the adhesion experiment is carried out, the piece of 3M tape is tightly sticked onto the surface of the film and then removed from the surface manually. As shown in Fig. 3, little change of the 8 × 8 grids is observed for the sample before and after adhesion experiment except that some contamination is remained on the surface of the film. This result further demonstrates the stable structure characteristics for TiN film and reveals the firm combination between the TiN film and the magnesium alloy substrate.

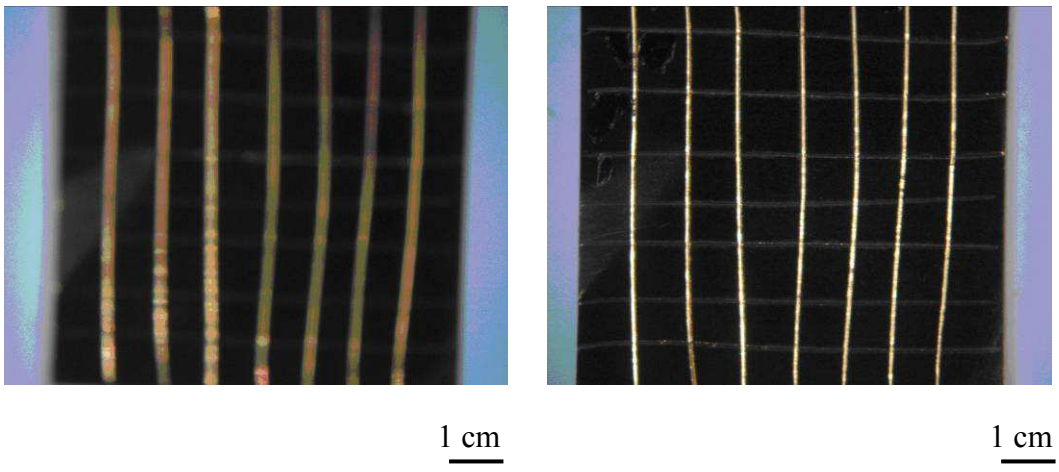

Fig. 3 The surface morphology images of TiN 3 # film observed by one optical microscope (Left: before adhesion experiment, right: after adhesion experiment)

The nano-indentation data of TiN 4# film are listed in Table 1. Before the nano-indentation experiment, the cross-profile of the film was observation by SEM. From the profile morphology, the thickness of the film is estimated as 4-5 μm. Thus the indentation depth was chosen as 500 nm. For investigating the micro-hardness properties of the whole surface of TiN film, 15 indentation points were chosen. From Table. 1, the micro-hardness varies from 19.25 Gpa to 32.74 Gpa. The worse uniformity of micro-hardness on the surface might result from the nano-sized effect. The arithmetic mean of the hardness of the 15 points is calculated as 23.85 Gpa, which is similar to those results reported by other literatures [9, 10] and accords with the fact of hard TiN.

Table 1 Surface micro-hardness data of TiN 4 # film measured by nano-indenter

Point Number	1	2	3	4	5	6	7	8
Hardness (Gpa)	19.25	25.25	27.03	23.35	19.12	17.88	26.04	27.56
Point Number	9	10	11	12	13	14	15	
Hardness (Gpa)	25.58	19.66	20.05	26.33	24.77	32.74	22.41	

Fig. 4 shows the surface morphologies of TiN 5# film before and after corrosion experiment in SBF. After 7 days' corrosion in SBF, the dense film was destroyed, as observed by SEM. Lots of holes and corrosion products appear on the surface of the sample. The corrosion behavior should be strongly related to the surface quality of the samples [11, 12].

The corrosion or degradation experiment is vital to the clinical application for the surface-modified magnesium alloy. Here, the study of corrosion behavior of TiN film on magnesium alloy substrates is initial and the detailed corrosion or degradation mechanism should be further explored.

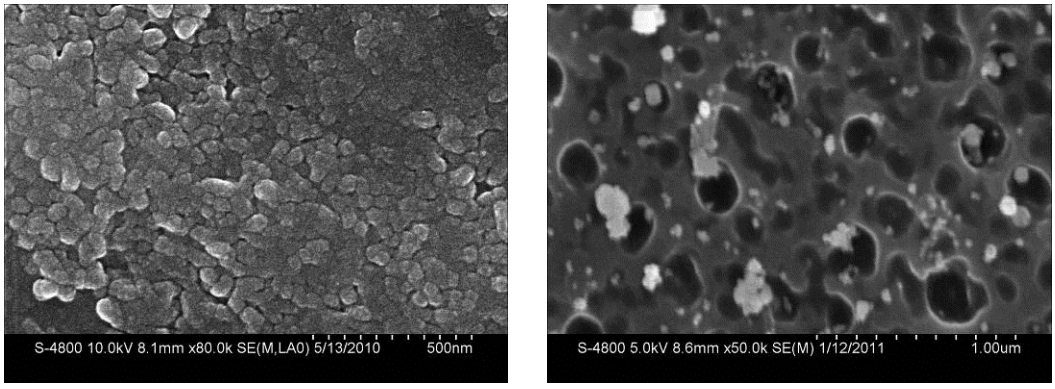

Fig. 4 The surface morphology images of TiN 5 # film observed by SEM (Left: as-deposited, right: after corrosion experiment in SBF)

Conclusions

The as-deposited TiN films on AZ 31 magnesium alloy substrates prepared by d.c. magnetron present dense structure characteristics. Under 200°C heat treatment for 30 minutes or 4 times heat treatment at 85°C for one hour, no structural defects such as cracks are observed on the surface of the films, which reveals heat stability of the films. Adhesion experiment further demonstrates the stability of the film and the strong combination between the film and the substrate. Nano-indentation experiment shows that the average micro-hardness of TiN film reaches 23.85 Gpa. Finally, the corrosion experiments in simulated body fluid initially reveal the degradation property of TiN film.

Acknowledgements

This work was financially supported by Shanghai Fundamental Key Project under contract number 08JC1421600 and Jiaxing Engineering Technology Centre of Light Alloy Metals, Chinese Academy of Sciences.

References

[1] S.K. Wu, S.C. Yen and T.S. Chou: Surface & Coatings Technology Vol. 200 (2006), p. 2769

[2] Y. Liu, Z.L. Wei, F.W. Yang and Z. Zhang: Journal of Alloys and Compounds Vol. 509 (2011), p. 6440

[3] G.S. Wu, X.Q. Zeng , G.Y. Li, S.S. Yao and X.M. Wang: Materials Letters Vol. 60 (2006), p. 674

[4] J. Zhang, Y. Zong, G. Yuan, J.C. Chang, P.H. Fu and W.J. Ding: The Chinese Journal of Nonferrous Metals, Vol.20 (2010), p. 1989

[5] J.X. Yang, F. Cui, In Seop. Lee and X.M. Wang: Surface & Coatings Technology Vol. 205 (2010), p. s182

[6] G.S. Wu, X.M. Wang, K.J. Ding, Y.Y. Zhou and X.Q. Zeng: Materials Characterization Vol. 60 (2009), p. 803

[7] H. Altun and H. Sinici: Materials Characterization Vol. 59 (2008), p. 266

[8] J. Zhang, D. Yang and X. Ou: Trans. Nonferrous Met. Soc. China Vol. 18 (2008), p. s312

[9] Harish C. Barshiliaa, Anjana Jainb and K.S. Rajam: Vacuum Vol. 72 (2004), p. 241

[10] L. Yu, S. Dong, J. Xu and G. Li: Acta Physica Sinica Vol. 57 (2008), p. 7063

[11] H. Altun, S. Sen: Surface & Coatings Technology Vol. 197 (2005), p. 193

[12] H. Hoche, C. Rosenkranz, A. Delp, M.M. Lohrengel, E. Broszeit and C. Berger: Surface & Coatings Technology Vol. 193 (2005), p. 178

Advanced Materials Research Vols. 314-316 (2011) pp 58-61

doi:10.4028/www.scientific.net/AMR.314-316.58

The Effect of Particle Concentration and Magnetic field on Tribological Behavior of Magneto-Rheological Fluid

Wan Li Song[1, a], Chul Hee Lee[1, b], Seung Bok Choi[1,c] and Myeong Woo Cho[1,d]

[1]Department of Mechanical Engineering, Inha University, Incheon 402-751, Korea

[a]feihusong2009@hotmail.com, [b]chulhee@inha.ac.kr, [c]seungbok@inha.ac.kr,

[d]chomwnet@inha.ac.kr,

Keywords: Magneto-Rheological Fluid, Magnetic Field, Particle Concentration, Tribology, Wear.

Abstract. In this paper, the effect of particle concentration and magnetic field on the tribological behavior of magneto-rheological (MR) fluid is investigated using a pin-on-disc tribometer. The wear loss and friction coefficient are measured to study the friction and wear properties of MR fluid. The morphology of the worn pin is also observed by scanning electron microscope (SEM) in order to analyze the wear mechanism. The results obtained in this work show that the wear loss and friction coefficient decrease with increasing particle concentration under the magnetic field. Furthermore, it is demonstrated that the magnetic field has a significant effect on improving tribological properties of MR fluid, especially the one with high particle concentration. The predominant wear mechanism of the MR fluid has been identified as abrasive wear.

Introduction

Magneto-rheological (MR) fluid is a smart material which is composed of micro-sized polarizable particles dispersed in a base fluid. Compared to electro-rheological (ER) fluid, MR fluid has some technology advantages of lower voltage, higher control effect and better stability with regard to contaminants [1]. Thereby, tribological characteristics of MR fluid are increasingly investigated due to their practical application in sliding parts, such as automotive and MR polishing. In recent years, the tribological behavior of an MR fluid without magnetic field activation has been studied using different experimental configuration [2, 3], and their researches showed that MR fluid was a better lubricant than the ER fluid and the dominant wear mechanism was abrasion under boundary lubrication conditions. Nevertheless, MR fluids are characterized by rheological properties under the magnetic field and have been widely used in the industry. Therefore, the most significative studies were referred to their magnetic properties, and the magnetic field usually reduced the wear rate and friction coefficient [4]. In view of studying the effect of particle concentration under magnetic field, the volume concentrations of MR particles selected in the present study are 10 vol. %, 20 vol. % and 30 vol. %, respectively. Main of this work is to investigate the effect of particle concentration and magnetic field on tribological behavior of MR fluid. In order to achieve this work, a pin-on-disk tribometer is designed and manufactured. The wear lose has been identified with respect to the particle concentration as well as sliding distances.

Preparation of MR Fluid

The MR particles used in the study are iron powder (RMS Technology Corp. Korea), and the average diameter and density of the iron particles are 1-5 μm and 7.8 g/cm^3, respectively. The base oils selected are paraffin (PA) oil (RMS Technology Corp. Korea). In order to prepare the MR fluid, the iron particles are dispersed in base oil through sonication and stirring of magnetic force for 15 minutes at room temperature (rotating speed R=500 rpm/min). The volume concentrations of MR particles are 10 vol. %, 20 vol. % and 30 vol. %, respectively. The MR characterizations are performed at 25°C at a controlled shear rate sweep and shear stress sweep, as shown in Table 1.

Table 1. Properties of MR fluid

Volume fraction [vol. %]	Density [g/cm^3]	Viscosity [Pa·s]
10	1.626	0.016±0.001
20	2.309	0.081±0.003
30	2.708	0.169±0.003

Experimental Setup and Test

Pin-on-disc tests are carried out in the tribometer shown in Fig. 1 to investigate the effect of particle concentration and magnetic field on tribological behavior of MR fluid. The magnetic induction produced by circular electromagnet is measured by a gaussmeter, and the magnetic induction can be altered in a range of 0-20 Gs in this experiment. The material of specimens in the experiment is steel (SM45C) with a hardness of 557 HB, which is always extensively used in the modern industry. The pin specimen has a diameter of 5 mm and a length of 30 mm, and the diameter and the thickness of the disc specimen are 60 mm and 8 mm, respectively.

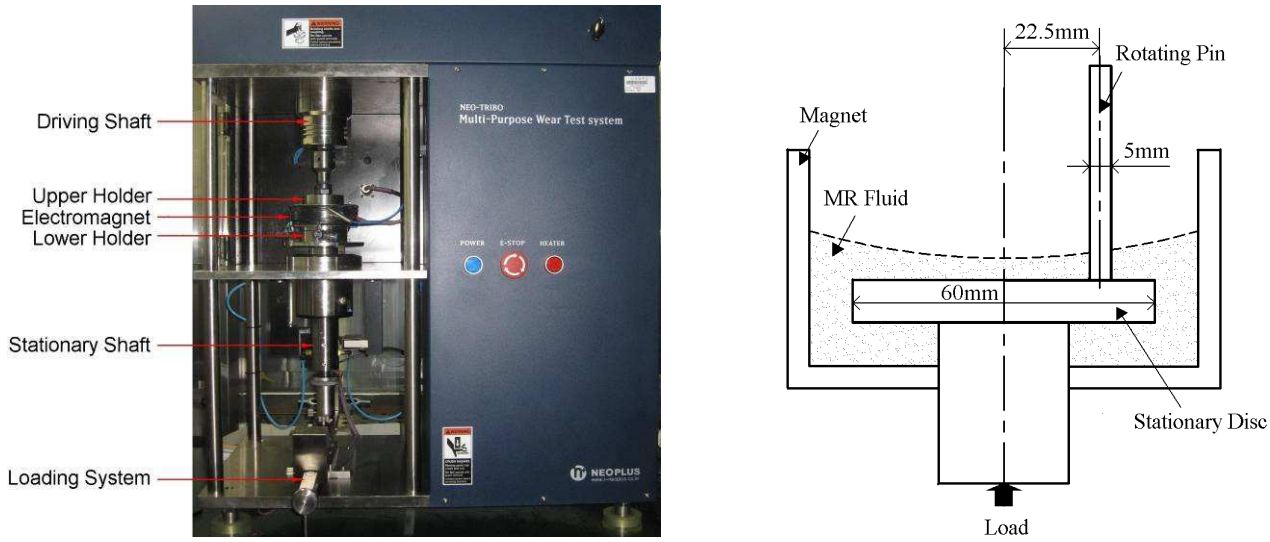

Fig. 1. The tribometer with an electromagnet.

The normal load for the tests is 30 N and the sliding velocity is 0.3 m/s. All of tests are performed at a temperature of 20-25°C and a humidity of 28-41%. The sliding distance is 1800 m for all of the tests, and the magnetic field is held to be constant at 10 Gs. The MR fluid is changed after each test in order to ensure the same fluid function. The removal rate is calculated by measuring the length loss of pin, and the friction coefficient is measured by the tribometer. After each test, the specimens are cleaned rigorously including wiping with alcohol and acetone. The worn surface of the pins and discs is observed by SEM in order to understand the wear mechanism.

Results and Discussion

Wear rate and friction coefficient. The wear loss and friction coefficient for different MR particle concentrations in the absence of a magnetic field are shown in Fig. 2. It can be seen that the wear loss increases with increasing MR particle concentrations in Fig. 2(a), and the slope of wear loss to sliding distance is the greatest for the particle concentration of 30 vol. %. From Fig. 2(b), the friction coefficient represents an increasing trend by increasing particle concentration. This is in accordance with observations made by Wong et al [2]. Moreover, the larger amplitude of fluctuation can also be seen. These phenomenons indicate that the MR fluid with high particle concentration has a higher friction and worse wear effect because of more trapped MR particles between the contact interfaces.

Fig. 3 shows the effect of magnetic field on wear loss and friction coefficient for different MR particle concentration. In Fig. 3(a) the wear loss increases with increasing particle concentration without the magnetic field. When the magnetic field is applied, the wear loss appears to be unchanged for the MR particle concentration of 10 vol. %. Nevertheless, the wear loss strongly decreases as the particle concentration increased. It is clear that the friction coefficient in Fig. 3(b) represents the same changing trend as the wear loss. It is indicated that applied magnetic field effectively improves the lubricating property of MR fluid, and the higher the particle concentration the better evident the improved effect.

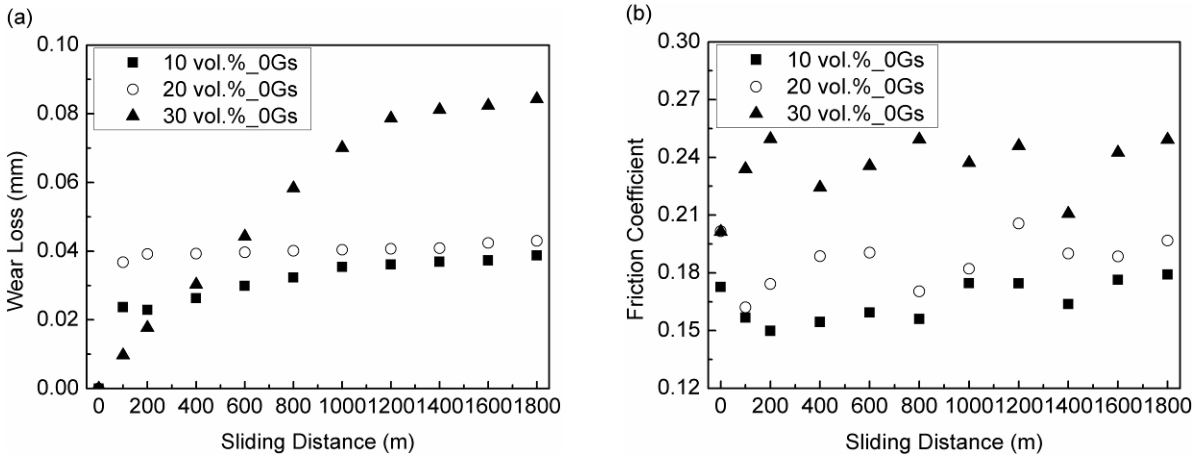

Fig. 2. (a) Wear loss and (b) friction coefficient for different MR particle concentrations without magnetic field.

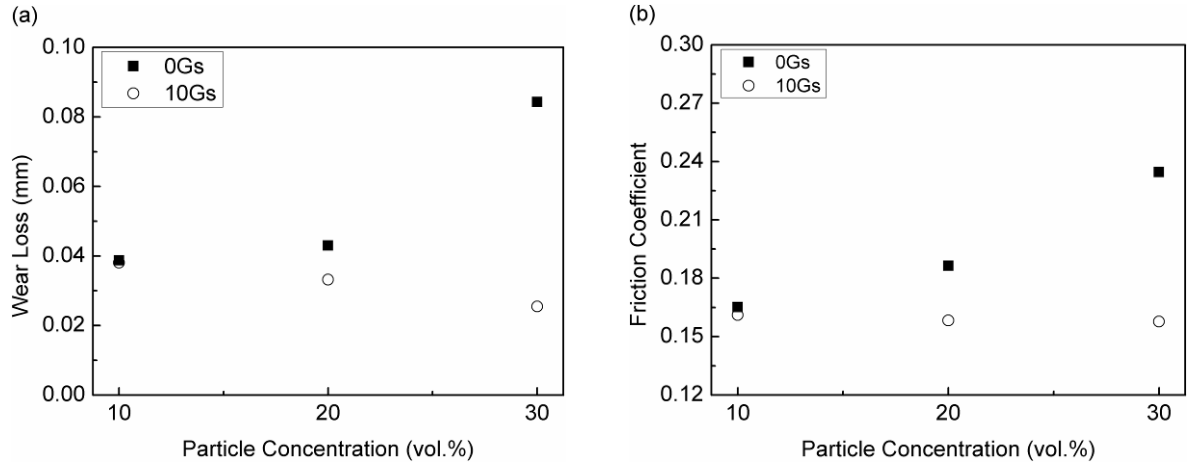

Fig. 3. (a) Wear loss and (b) friction coefficient for different MR particle concentrations with and without magnetic field.

Morphology of the surfaces. Fig. 4 shows the SEM topography of the worn pins after the test for different particle concentration and magnetic field. In all of the SEM micrographs, the arrows are shown to indicate the sliding direction after the experiment. The worn surfaces in Figs. 4(a), (b) and (c) are lubricated by MR fluids with 10 vol. %, 20 vol. % and 30 vol. % particle concentrations, respectively. As shown in Fig. 4(a), there appears to be many ribbon-like ridges with lips rearing off in the plastic contact area, and micron debris is being generated. However, in Figs. 4(b) and (c), experiments produced some deep narrow groove and small flakes breaking out of the sides of the deep grooves on the worn surfaces. This is because that more MR particles are trapped into the contact surfaces with increasing particle concentration, then deeper grooves are generated on the surfaces due to shearing and cutting. It indicates that the MR particles acting abrasive material and the abrasive wear is the predominant wear mechanism, and the MR fluid with high particle concentration reveals a worse wear behavior.

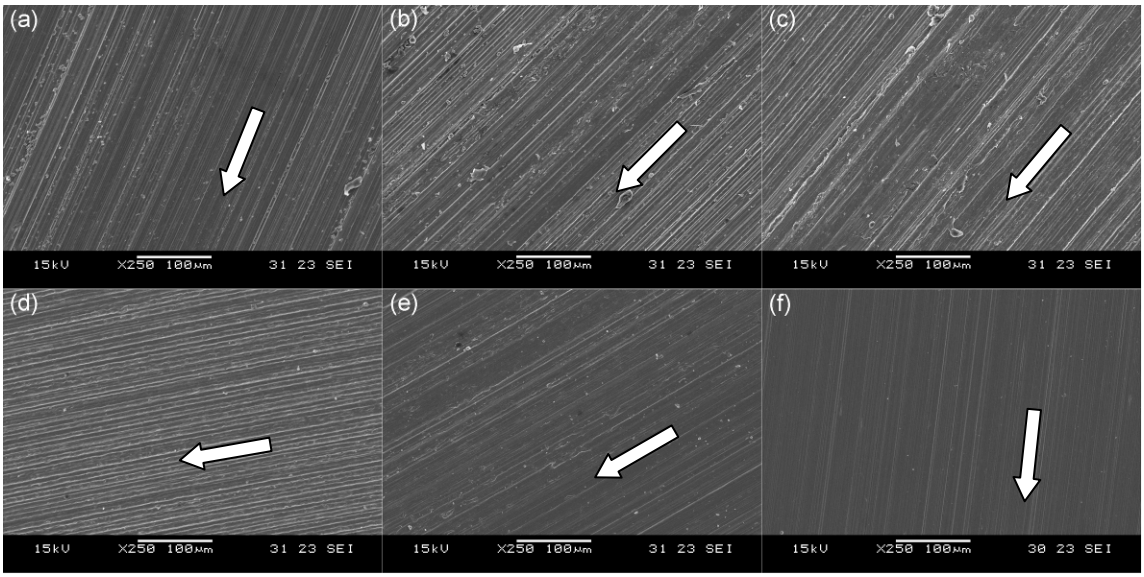

Fig. 4. SEM topography of the worn pins for different particle concentration and magnetic field: (a) 10 vol. %, 0Gs; (b) 20 vol. %, 0Gs; (c) 30 vol. %, 0Gs; (d) 10 vol. %, 10Gs; (e) 20 vol. %, 10Gs; (f) 30 vol. %, 10Gs

Figs. 4(d), (e) and (f) represent the worn surfaces lubricated by MR fluid with 10 vol. %, 20 vol. % and 30 vol. % particle concentrations under magnetic field. It can be seen that the surface features in Fig. 4(d) are the same as the one in Fig. 4(a). However, the average width and depth of the grooves appear to be decreased in Figs. 4(e) and (f). It indicates that the magnetic field has a significant effect on improving tribological properties of MR fluid, especially the one with high particle concentration.

Conclusions

In this work, the effect of particle concentration and magnetic field on tribological behavior of MR fluid has been investigated using the tribometer. In the absence of magnetic field, the MR fluid with high particle concentration has worse friction and wear properties than the one with low particle concentration. However, the wear loss and friction coefficient decrease dramatically when the magnetic field is applied. By observing the worn surfaces using SEM, it indicates that MR particles play an important role in the wear process, and the abrasive wear is the predominant wear mechanism. Moreover, the magnetic field has a significant effect on improving tribological properties of MR fluid with high particle concentration. It is finally remarked that the tribological characteristics of MR fluid under several different temperatures will be undertaken as a second step of this work.

Acknowledgements

This work was supported by the Ministry of Knowledge Economy (MKE) and the Korea Industrial Technology Foundation (KOTEF) through the Human Resource Training Project for Strategic Technology.

References

[1] A.G. Olabi and A. Grunwald: Mater. Design Vol. 28 (2007), p. 2658-2664

[2] P.L. Wong, W.A. Bullough, C. Feng and S. Lingard: Wear Vol. 247 (2001), p. 33-40

[3] J.W. Sohn, S.B. Choi, C.H. Lee and M.W. Cho: Adv. Mater. Res. Vol. 79-82 (2009), p. 83-86

[4] W.L. Song, S.B. Choi, J.Y. Choi and C.H. Lee: Tribol. T. DOI: 10.1080/10402004.2011.584365 (2010)

Advanced Materials Research Vols. 314-316 (2011) pp 62-65

doi:10.4028/www.scientific.net/AMR.314-316.62

Application of multi-layer composite membrane in tricone bit bearing

Yaling Qiu[1,a], Shibin Li[1,b] ,Wei He [1,c], Chuanjun Han [1,d]

[1]School of Mechanical Engineering, Southwest Petroleum University, Chengdu 610500, China

[a]qiuyaling@126.com, [b]libin031@126.com,[c]xuezhu9@sina.com,[d]hanchuanjun@126.com

Keywords: Magnetron sputtering, Abrasion test, Multi-layer composite membrane, TiN, WC/C, TiAlN+WC/C

Abstract. Composite membranes of TiN, WC/C and TiAlN+WC are successfully prepared by means of magnetron sputtering. An analysis of the membranes' hardness, surface topography and chemical composition indicates that the composite membrane have a greater hardness, and are compact in structure and uniform in texture. A abrasion test is conducted by applying the three membranes respectively to tricone bit bearings, and then a comparison made between them and non-membrane tricone bit bearing leads to the finding that tricone bit bearing with TiAlN+WC/C composite membrane has the highest abrasion resistance, with a dramatic increase of 30%~40%.

Introduction

With the development of economy, the need for oil is increasing day by day, and deep well oil production is becoming more and more difficult. Against this background, there appears an increasingly higher demand for the performance and operation of oil drilling equipment. In terms of this, tricone bit is a rock-breaking tool which is applied to rocks directly. While working, it rotates together with the drill stem, with each roller cone rotates around its claw. Tricone bit drills deeper and deeper into the ground by striking, crushing and shearing and finally breaking strata rock while rotating. Yet its operational life span is greatly shortened because of the complexity of geological conditions as well as impact load, high temperature, high pressure and overload in the course of drilling. According to years of experience, the main reason for its short life is the wear-out failure of the bearing, too fast, too early, which greatly shortens the normal operational life span of the tricone bit, and seriously hinders the oil drilling industry from improving its efficiency.

To ensure a longer operational life span for the tricone bit against all those unfavorable conditions, it is critical to improve the operational life span and also improve the abrasion resistance performance of the shaft and bearing. In recent years, extensive research has been conducted on composite membrane, and such multi-layer composite membrane as TiN, WC/C and TiAlN+WC/C have found their wide application with its superiority in super-hardness and abrasion resistance property. Multi-layer composite membrane is a kind of nanoscale sedimentary coating, not only with higher hardness but also high toughness, greater capability against corrosion and abrasion. Because of the increase of sedimentary interface of multi-layer, and residual stress is lesser in process of sedimentation, its ability of resistance to crack expansion has obviously enhanced [1-4]. Therefore, it is extremely significant apply multi-layer composite membrane to tricone bit bearings so as to improve the overall operational life span of tricone bit.

Test preparation

Cone rotates around claw when tricone bit is drilling, and the interface of claws and cone constitute a sliding friction surface. A abrasion test is carried out between cone and a lantern ring fixed with coated composite membrane on its claw, and the structure of cone bit is show in Fig.1 (1-lantern ring, 2-cone，3-claw). Fig.2 shows the assembly diagram shape design, with no change in its matching surface with claw in order to install and fix the cone easily in abrasion test. After many prior trials, in order to ensure the effectiveness of the membrane, test preparation the experimental results, in trails the material of lantern ring (Fig. 3) is Cr12MoV, and the material of cone specimen is 20CrNiMo which is in practical use.

In the test, tricone bit bearing test specimens were made respectively coated with TiN, WC/C and TiAlN+WC/C composite membrane. In order to learn more accurately about abrasion resistance after coating, a comparison test is made between the coated tricone bearing specimens and bearing without any membrane of membrane. The thickness of the three specimens is unified coating 5μm, and abrasion resistance performance is evaluated in terms of abrasion time by comparing different membranes whose abrasion are measured at a unified 5μm.

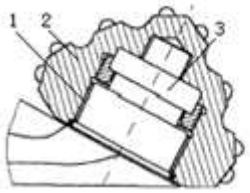

Fig. 1 Structural drawing of tricone bit

Fig. 2 Assembly diagram

Sputtering coating principle

Sputtering coating means that electron gets enough charge energy in electric field, and then it collides with argon atom when shooting its way to the matrix, which decomposed into an Ar^+ and an electron, with Ar^+ accelerating toward the target and bombarding its surface with great energy, which makes the negative target sputter, with the electron flying to its matrix. Among the sputter particles, the neutral target atoms deposit on the matrix and form a membrane. The secondary electron resulting from the collision takes circular motion under the effect of electric and magnetic fields in the course of its shooting to the matrix [5, 6]. Along with the increase of collision times, the electron gradually reduces its energy and moves away from the target surface. When the electron runs out of its energy, it deposits on the matrix under the effect of electric fields. By this time, the electron is very low in energy, and can only impart a small amount of energy to the matrix while getting deposited on the matrix, causing a lower temperature of the matrix. This kind of low temperature magnetron sputtering method avoids high temperature effect in chemical deposition that makes matrix organization crystal bulky, which causes brittle phase, and generates such negative effects as its poor performance.

Membrane preparation

The specimens were ground and polished before coating, then cleaned for 10 minutes with ultrasonic wave in acetone and anhydrous alcohol respectively to enhance the binding force between membranes and specimens. Before depositing the membrane, the furnace was vulcanized until the degree of vacuum meets 6×10^{-3}Pa, impressed negative bias at –800V, then Ar gas ventilated in for ion bombardment cleaning for 5 minutes.

Preparation of TiN membrane. Open Ti arc target 50A for Ti ion bombardment cleaning. Then deposit pure Ti for 10 minutes as transition layer, and then N_2 ventilated for preparation of the TiN membrane, with a temperature of 430℃ and preparation time of 30 minutes.

Preparation of WC/C membrane. Open C and W electric arc target 50A, deposit WC/C membrane by bombarding Ar gas against the target materials at 250 ℃, with a preparation time of 30 minutes**.**

Preparation of TiAlN+WC/C composite membrane. Open Ti arc target 50A for Ti ion bombardment cleaning, then deposit pure Ti for 10 minutes as transition layer. Then open Al magnetic control target 50A at the same time and ventilate N_2 to deposit TiAlN membrane, with a temperature of 430 ℃, and the time of 30 minutes. Upon TiAlN membrane coated, the WC/C coating starts. Because specimens are exposed to direct contact with air during the process of changing target, Ar gas is to be ventilated for ion bombardment cleaning for 3 minutes. The preparation time for WC/C is 30 minutes and the temperature is 430 ℃.

Specimen membrane detection

This is to test the hardness, structure, membrane thickness, structure phase and binding force of composite membrane by means of microhardness instrument, microscopic analyzer, scanning electron microscope (SEM), energy spectrum curve watcher, X-ray apparatus and adhesion scratch test machine. The findings of SEM and energy spectrum curve watcher indicate that, by applying magnetron sputtering, whether TiN, WC/C composite membrane or TiAlN+WC/C multi-layer composite membrane, they are all compact and uniform in texture, and smooth on surface, among which TiN and TiAlN composite membrane and the pseudo diffusion layer of matrix surface ensure higher binding strength between the membrane and matrix. The findings of microhardness instrument show that the surface hardness of composite membrane bearing coated with TiN, WC/C and TiAlN+WC/C are respectively 1300HV, 2300HV, 3000HV, all harder than the surface with no membrane coating, among which, the surface hardness of multi-layer composite membrane bearing coated with TiAlN+WC/C is 30% to 40% greater than the bearing surface without coating.

Abrasion test

Install lantern ring coated respectively with TiN, WC/C, TiAlN+WC/C and the lantern ring without any coating on claw (Fig. 4). Then conduct abrasion test by first installing the coated lantern ring on claw, then fitting with the specimens of cone, and then installing them on the abrasion test machine (Fig. 5). Fig. 6 shows the test specimen after the abrasion test. Firstly, apply the abrasion test on the lantern ring coated with TiN membrane, with the abrasion test time being 10 hours for the first time, then, take out the specimens and measure their membrane by using SEM, and then decide the next time for abrasion according to the measurement of the surplus membrane thickness. With the surplus membrane thickness reducing, the times for next abrasion gradually shortens, and when the coating is completely worn off, add abrasion periods for each time and thus the total abrasion time of lantern ring coated with TiN is about 12 hours. By applying this method, abrasion test is conducted on specimens coated with WC/C, TiAlN + WC/C membranes, and finally the abrasion time for specimen of WC membrane is about 13 hours, specimen of TiAlN+WC/C composite membrane about 14.5 hours, the specimen without any membrane only about 10.5 hours. A comparison of the four specimens in terms of their abrasion time leads to the conclusion that Nano-coated specimens performs better than that without any membrane, and among which the specimen coated with TiAlN+WC/C composite membrane lasts the longest in the abrasion test, 30% to 40% longer than the specimen without coating.

Fig. 3 Lantern ring Fig. 4 Claw-fixed lantern ring Fig. 5 Abrasion test machine Fig. 6 Worn parts

Test results analysis

A comparison of abrasion test between specimens with TiN, WC/C, TiAlN+WC/C membranes and that with no membrane can lead to the following findings:

(1) As Fig.7 shows, with the same amount of abrasion extent, abrasion resistance time for any coated specimen is longer than that without coating.

(2) As Fig.7 shows, with the same amount of abrasion extent, the three membranes of TiN, WC/C, TiAlN+WC/C exhibit different property, with WC/C membrane superior to TiN membrane in abrasion resistance, and specimen with TiAlN+WC/C composite membrane the longest abrasion resistance time.

(3) As Fig.7 shows, with the same amount of abrasion extent, there is a dramatic improvement of 30% to 40% in abrasion resistance performance for lantern ring with TiAlN+WC/C composite membrane against the one without membrane.

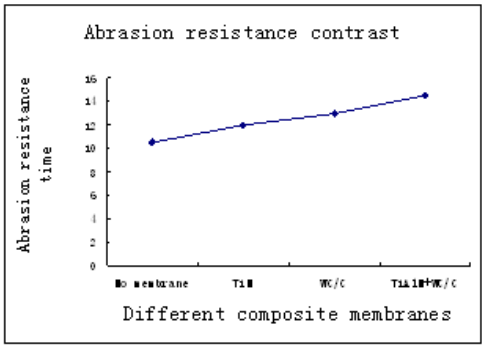

Fig.7 Abrasion resistance contrast

Conclusion

The application of TiAlN+WC/C composite membrane technology to cone bit bearing can effectively reduce the abrasion of bearings, lengthen the operational life span of the bearings, thus lengthen the normal working hours of cone bit. The research findings have been put into production, waiting for on-the-spot trial in oil field. The successful application of the technology is of great significance to a bright future: reduce the times of changing bits, improve the drilling efficiency, reduce the drilling cost and improve production efficiency.

Acknowledgements

This work was supported by the Sichuan Technology Foundation (2009GZ0026)

References

[1] X.D.Lin, X.D.Song, G.S.Fu. Arc ion coating and medium frequency magnetron sputtering Preparation TiAlN composite membrane. [J]. in Chinese. China surface engineering, 2008, (21): 40-44.

[2] L.Lu, T.Jiang, J.Yan. Effect of composition and hardness of TiAlN/TiN membrane organization on Matrix of negative bias [J]. in Chinese. Materials heat treatment technology, 2009, (12): 78-81.

[3] Y.Liu, B.Liu, S.L.Liu, Study on organization structure and performance of TiAlN membrane preparation by Magnetron sputtering [J]. in Chinese. Hard metal, 2009, (12): 218-221.

[4] X.D.Lin, X.D.Song, G.S.Fu. Study on TiAlN membrane preparation by Arc ion coating and medium frequency magnetron sputtering [J]. in Chinese. Special annual of casting and non-ferrous alloy in 2008, 2008: 274-277.

[5] W.G.Tang. Study on multi-layer composite membrane of TiN/TiAlN and preparation [D]. in Chinese. Master theses, Lan Zhou University.

[6] Y.J.Guo. Study on magnetron sputtering coating technology and material mechanics performance of Bearings [D]. in Chinese.Ph.D. Thesis, Harbin engineering university.

Advanced Materials Research Vols. 314-316 (2011) pp 66-69

doi:10.4028/www.scientific.net/AMR.314-316.66

Experimental Study on Hot Bending of 22MnB5 Steel

R.Q. Guo[1], L. Ying[1], P. Hu[2,a], W. Guo[3], X.Q. Han[1], Z.H. Meng[1]

[1]School of Automotive Engineering, Faculty of Vehicle Engineering and Mechanics, Dalian University of Technology, Dalian, China 116024

[2]State Key Laboratory of Structural Analysis for Industrial Equipment, Dalian University of Technology, Dalian, China 116024

[3]College of materials Science and Engineering, Jilin University, Changchun, China 130025

[a]pinghu@dlut.edu.cn

Keywords: Hot Forming, 22MnB5, Bending Property, V_Shaped Test, Optimal Temperature Zone

Abstract. Special V-shaped heat bending test was designed for 22MnB5 hot forming steel of different thicknesses. Blanks after heating 5 min at around 950℃ to austenize fully were bended at different temperature conditions, and simultaneously the spring-back behavior and microstructure features of heat bending specimens were investigated. The result shows that 600-650℃ temperature zone is optimal for bending forming and martensite texture transforming. Real hot forming anti-collision beams were produced at 600-650℃ and comparison bending test was conducted to reveal more qualified mechanics at this temperature zone.

Introduction

For growing energy shortage nowadays, it is an inevitable trend of developing fuel-efficient vehicles and eco-car. Studies have shown that lightweight is the most effective measure to achieve that goal and reducing vehicle mass by 10% can save fuel by 3%~7%[1,2]. In the project of Ultra-light Steel Auto Body-Advanced Vehicle Technology Program (ULSAB-AVC) of International Iron and Steel Institute (IISI), the body in white is lightweight by 30% for applying hot forming parts[3].With increasing use of hot forming parts, the hot stamping technology is developed rapidly, through which stamping forming and quenching are achieved simultaneously. Nowadays, A pillar, B pillar, C pillar, door and roof reinforcements, bumpers and etc, are typical vehicle components formed by hot stamping[4,5]. In hot stamping process, complicated thermal-mechanical-transformation coupled relations and multi-scale problems are involved besides nonlinear friction problems of thermal boundary. And there are lots of thermal parameters affecting mechanical properties of the hot forming components. Substantially, the hot stamping is a process of metal sheet bending so that bending properties of metal sheet influence its hot forming formability significantly. On the basis of that reason, special V-shaped heat bending test is designed, bending formability at different temperatures is investigated, and optimal bending forming temperature zone is obtained, which presents guidance function on actual hot stamping process. At the same time, real anti-collision beams are hot stamped according to above research. In the end, pure bending test is conducted on the anti-collision beam for comparison, which shows its higher bending strength and impact resistance at the optimal temperature zone.

Basic Material Characteristics of 22MnB5

In the paper, a new kind of 22MnB5 hot forming steel is investigated focused on three thicknesses samples, 1.2mm, 1.6mm and 2.0mm. Its composition is as shown in Table1. A small amount of boron added enhances the quenching hardenability of C-Mn steel and its strength. As shown in Fig.1, microstructures of original 22MnB5 are ferrite, pearlite and a small amount of carbide while strip-shaped martensite is the main microstructure of quenched samples.

Table1 Composition of 22MnB5 (Mass %)

22MnB5	C	Mn	B	P	Cr	Si	Al	S
Max	0.240	1.290	0.0037	0.016	0.210	0.240	0.050	0.006
Min	0.225	1.240	0.0034	0.013	0.163	0.180	0.023	0.002

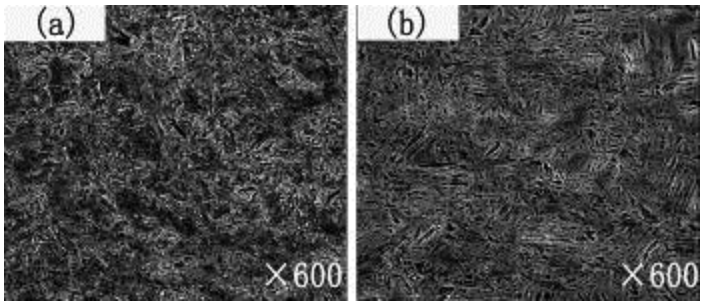

Fig.1 Microstructures of (a) original samples (b) quenched samples

Through typical tensile experiment, relative mechanic properties are shown in Table2. It shows that yield and tensile strength of quenched samples, around 1000Mpa and 1500Mpa, are 3 times as high as the original and the former elongation is just 7%, much less than 32%, the original elongation. Besides, hardening exponent (N value) decreases from 0.21 to 0.11 after quenching which explains that 22MnB5 formability after quenching is so poor that hot stamping is must introduced.

Table2 Mechanical properties of no-quenching and quenching 22MnB5

22MnB5	Yield Strength (Mpa)	Tensile Strength (Mpa)	Yield Ratio	Elongation (%)	N Value
Original	300	500	0.62	32	0.21
Quenched	1000	1500	0.65	7	0.11

Special V-Shaped Heat Bending

It's known that hot forming process is introduced to stamp 22MnB5 and quench it at the same time for ultra-high strength parts. The optimal stamping temperature zone (OTZ), a key parameter of hot stamping, significantly affects blank formability and mechanical properties of hot forming parts. To get the OTZ, special V-shaped heat bending is designed imitating the real hot stamping, see Fig.2(a).

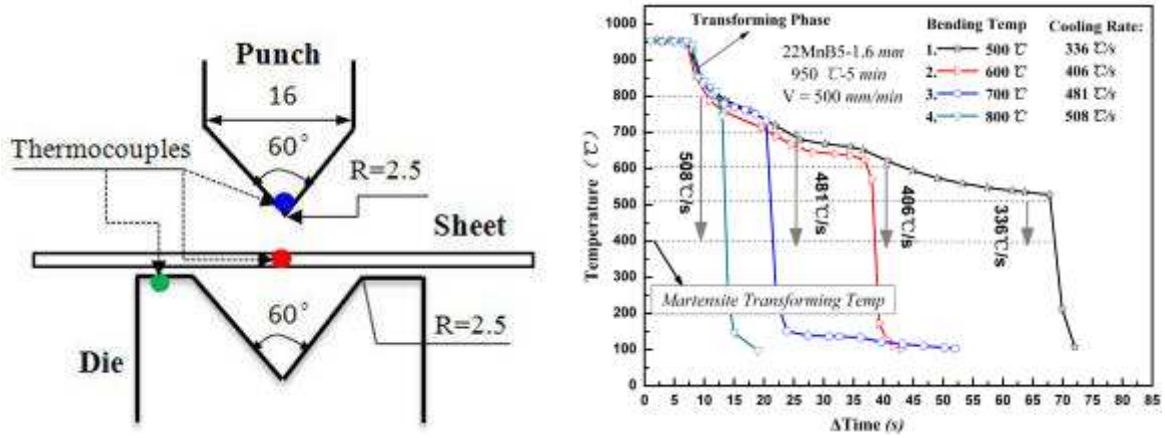

(a) (b)

Fig.2 (a) Special V-shaped Bending (b) Correlation of temperature and time in V-shaped bending

The temperature acquisition system of V-shaped test is shown in Fig.2(a): three thermocouples are individually placed in the sheet middle, the punch head and the die surface. The sheet is transformed to V-shaped die quickly, after staying 5 min in the furnace at around 950℃ to austenize fully. When the sheet temperature reaches the set temperature such as 500℃,600℃,700℃ and 800℃, the universal tensile testing machine is started to stamp at 500 mm/min speed and V-shaped heat bending

parts are formed. Also samples of 1.2mm, 1.6mm and 2.0mm are involved. The temperature-time curve of 1.6mm sheet is shown in Fig.2(b). It's found cooling rate reaches 508℃/s when stamping at 800℃, and it decreases to 336℃/s at 500℃, which will affect martensite forming and mechanical attributes obviously. Meanwhile spring-back angles of specimens are also measured, which is shown in Fig.3(e). It shows that the spring-back angle is the smallest when bending at around 600-650℃, which explains that 22MnB5 has better plasticity and formability at that temperature zone. It's a little different from the standpoint, "22MnB5 has better stamping formability at 650 to 750℃ " in [6]. Also, microstructures of heat bending specimens are analyzed. As found in Fig.3, strip-shaped martensite is hard to find when bending at 500℃; strip-shaped martensite is filled with the microstructure of sheets stamped at 600℃ and 700℃ and its texture is more fine than that of sheets formed at 800℃, although whose main microstructure is also martensite. From the microstructure, it's also verified that 22MnB5 has better plasticity and formability at 600-650℃ due to more fine martensite texture.

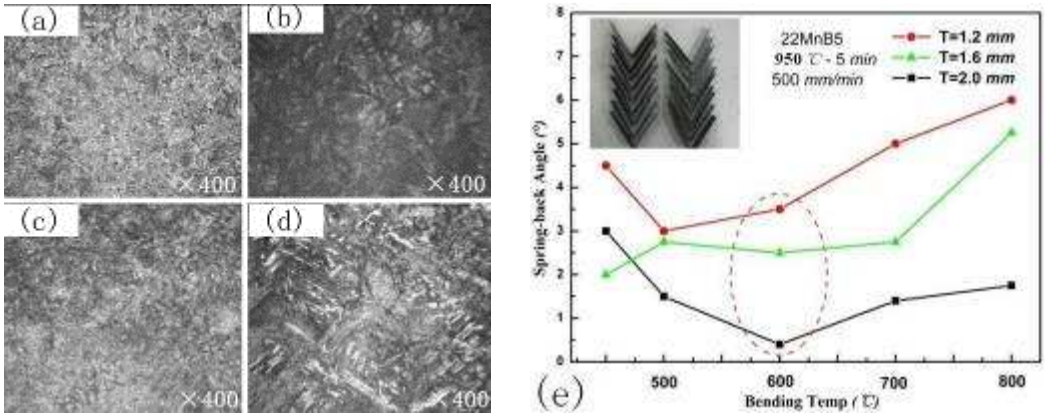

Fig.3 Microstructure of sheets bended at (a)500℃ (b)600℃ (c)700℃ (d)800℃ (e) Correlation of bending-temperature and spring-back angle

Bending Characteristic Comparison of Hot Forming Components

Comparison test is conducted focused on the OTZ. Real anti-collision beams are hot stamped at around 600-650℃ and 800℃, based on 1.6mm blank, as shown in Fig.4(a).

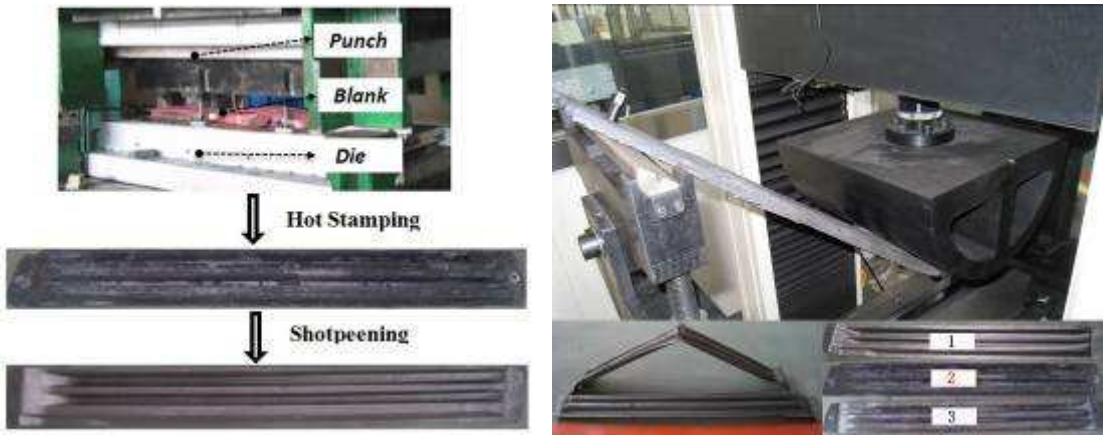

(a) (b)

Fig.4 (a) Hot stamping for the beams (b) the pure bending test

Then pure bending test is conducted on the hot stamping beams, including cold stamping ones, shown in Fig.4(b). As shown in Fig.5(a), the deformation-load curve peak of beams formed at 600-650℃ is slightly higher than that of beams stamped at around 800℃, and through 300mm deformation the

former beam is intact but obvious cracks are developed in the latter beam as shown in Fig.5(b), through which the result, 600-650℃ is the OTZ, of the V-shaped heat bending test is demonstrated again. Besides, the bending strength of cold stamping beams, 44 Mpa, is only one third of hot stamping ones', 115 Mpa. The maximum bending load of hot forming specimens is as high as 11000 N, but that of cold stamping ones is only 5000 N. It reveals that hot stamping significantly enhances bending strength, energy absorption capability and passive safety of auto parts.

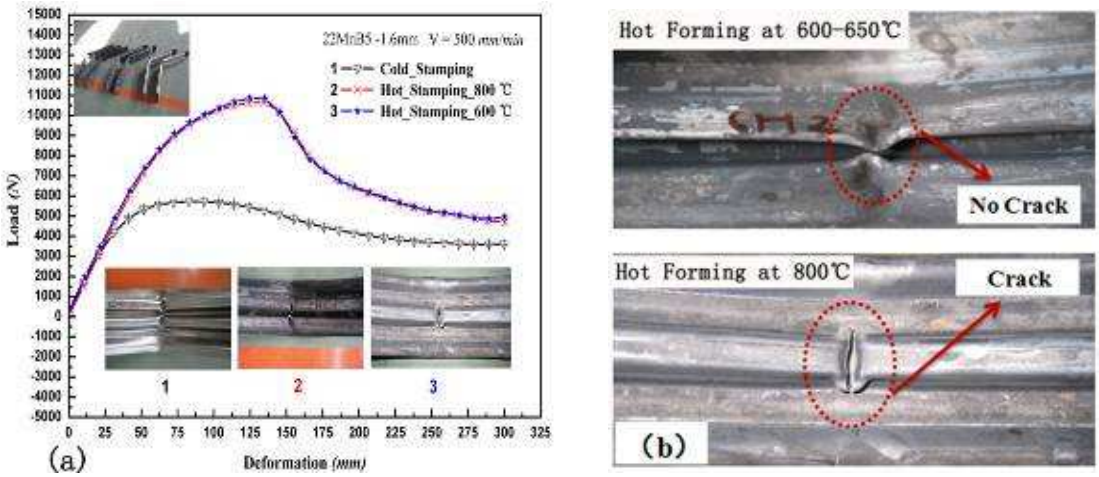

Fig.5 (a) Correlation of deformation and load (b) comparison of the bending result

Conclusions

Hot forming technology enhances component strength significantly to make vehicle more lightweight and safe. The temperature zone, 600-650℃, is optimal for 22MnB5 bending forming due to more fine martensite texture and smaller spring-back amount. The real hot forming component bending test also shows that anti-collision beams formed at 600-650℃ has more qualified mechanical characteristics.

Acknowledgment

This work was supported by the Key Project of the National Natural Science Foundation of China (No. 10932003), "863" Project of China (No. 2009AA04Z101), and "973" National Basic Research Project of China (No. 2010CB832700).

References

[1] Jens Kondratiuk, Patrick Kuhn, Eckhard Labrenz, Christine Bischoff: Surface and Coatings Technology Vol. 205(17-18)(2011), p.4141.

[2] Senuma T: ISIJ International Vol. 41(6) (2001), p.520.

[3] Li Wang, Xiongfei Yang, Jiangxin Lu: Iron and Steel Vol. 41(9)(2006),p.1. In Chinese

[4] Weili Xu, Shurong Guan, Jian Ai and Aihui Luo: World Iron and Steel Vol. 9(2) (2009),p.33. In Chinese.

[5] Myoung-Gyu Lee, Sung-Joon Kim, Heung Nam Han, Woo Chang Jeong: International Journal of Mechanical Sciences Vol.51(11-12)(2009), p.888.

[6] Ping Hu, Ning Ma, Wei Guo, Guozhe Shen and Wenhua Wu. "Researching Progress of hot Stamping Technique for Auto Body Load-carrying Parts with Extra-High Strength," in Mechanics and Engineering Application Conference Proceedings, Shanghai, 2010. In Chinese.

Advanced Materials Research Vols. 314-316 (2011) pp 70-73

doi:10.4028/www.scientific.net/AMR.314-316.70

Microstructure and Property of Cold Sprayed Copper Coating

Yuliang Liu [1, a], Zebin Bao [2,b], Tianying Xiong [2,c]

[1]School of Materials Science and Engineering, Henan University of Science and Technology, Luoyang, China

[2]Institute of Metal Research, Chinese Academy of Sciences, Shenyang, China

[a]purelandliu@126.com, [b]zbbao@imr.ac.cn, [c]tyxiong@imr.ac.cn

Keywords: cold spray, copper, coating, microstructure, microhardness

Abstract. Cold spray is a new surface engineering technology. In this paper, pure copper particles were sprayed on the Al substrate by this method and the copper coating was deposited sucessfully on the surface of the substrate. The microstructure of the coating and the interface between the coating and the substrate were observed by optical and scanning electron microscopes, and the phase was identified by XRD for the pure copper particles and the coating. The microhardness of the coating is measured. The results show that mechanical bonding is the main mechanism for the interface between the coating and the substrate, and there is a few metallurgical bonding for the interface; the coating is dense and its porosity is less than 0.4%; XRD results indicate that there is no oxidation occurred during the spray process. The microhardness of the coating is about 160Hv, which is higher than that of the as-casted copper.

Introduction

Cold spraying is an emerging coating technology. A coating is formed by plastic deformation of sprayed particles in a solid state during impact in cold spraying. The temperature of spray particles prior to impact is much lower than their melting point and spray materials experience little microstructure change, oxidation or decomposition [1,2]. Most metals including Cu, Al, Ni, Fe, Ti and their alloys can be deposited by cold spraying [1-5], and even cermets [3] or ceramic particles [4] can be embedded into a metal substrate to form a thin layer coating. In this paper, pure copper particles were sprayed on the Al substrate by the cold spray process using optimal processing parameters, and the microstructure of the coating and the interface between the coating and the substrate were investigated in order to understand the formation mechanism of the coating.

Experimentals

Commercially pure copper particles (99.9%) are used for the spray process. Al substrate was cut into φ25mm×5mm. The chemical compositions of the copper particles and the Al substrate are shown in Table 1.

The copper particles were sieved to the range of 40-50μm for the spray process. The surface of the substrate was ground with SiC paper up to 800 grit, cleaned ultrasonically using anhydrous alcohol, dried and then pilled with alumina before coating deposition. The carrier gas for the process was air The optimal parameters for the processing are shown in Table 2, and the distance between the substrate and the nozzole is 30mm, preheating temperature is 583K, gas pressure is 2.1MPa. The morphology the copper particles is observed by S360 SEM, and the microstructure of the coating and the interface between the coating and the substrate are investigated by JSM-6301F SEM. Phase analysis of the copper particles and the coating is carried out by the D/max2400 XRD, with Cu K_α radiation and step mode 4°/min. The microhardness of the coating is measured by FM-700 microhardness tester with load 200g and loading time 15s.

Table 1 Chemical compositions of the copper particles and Al substrate/(wt%)

Materials	C	Si	Pb	Mn	Fe	Al	Cu
Copper particles	-	-	0.05	-	0.02	-	balance
Al substrate	-	0.35	-	0.2	0.9	balance	-

Table 2 The optimal parameters for the cold spray processing

Items	Operating gas	Spray distance [mm]	Gas temperature [K]	Pressure [MPa]
Parameter	air	30	583	2.1

Results and Discussion

XRD results

Fig. 1 shows the XRD patterns of the copper particles and the coating. It is indicated from the Fig. 1(a) that no copper oxide exists in the copper particles. The Fig. 1(b) indicates that there is no oxide in the coating too, which indicates that no oxidation occurred during the spray process, and this is one of the advantages of the cold spray compared with the thermal spraying process when the sprayed materials are easily oxidized.

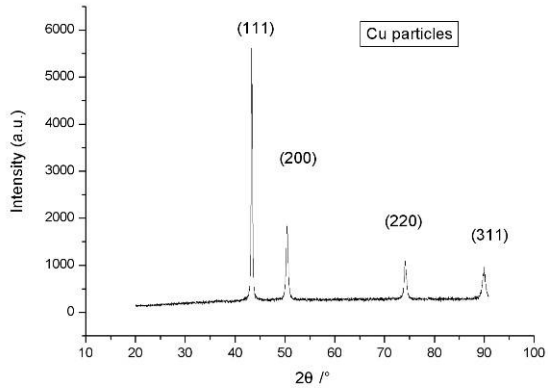

Fig. 1(a) XRD pattern of the Cu particles

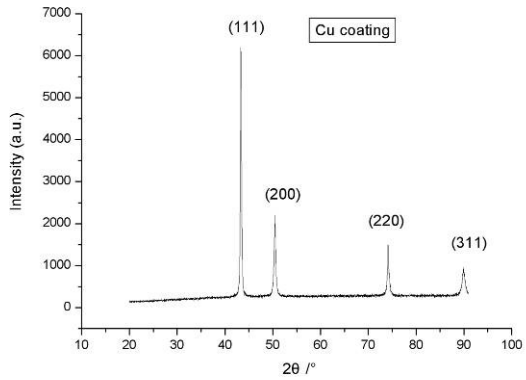

(b) XRD pattern of the coating

Microstructure and bonding mechanism of the coating

Fig. 2 shows the morphology of the copper particles before spraying. It is found that most of the particles are spherical, and some of them are irregular. Fig 3 shows the optical metallograph of the coating and the interface between the coating and substrate. It is found that the coating is dense and no obvious pore exists in the coating. It is calculated that the porosity of the coating is less than 0.4%. There are no defects existing on the interface between the coating and the substrate.

The particles were deformed severely during the cold spraying process, and new and fresh surfaces, where metallurgical bonding may be induced, are created in the deformed particles. It is thought that the kinetic energy of the particles will be transformed into deformation energy and heat energy at the impacting moment (-10^{-8}s)[6]. The more powerful the kinetic energy of the particles are, the more overwhelming the impacting force is, and the more deformed the particles and the substrate are, the stronger the bonding strength of the coating and the substrate is. When the velocity of the particles is above the threshhold velocity, the particles can be deformed severely and bonded with the substrate. This kind of bonding is similar to that of explosive forming and welding, i.e. metallurgical bonding. The arrow in the Fig. 4 shows the metallurgical bonding area in the coating.

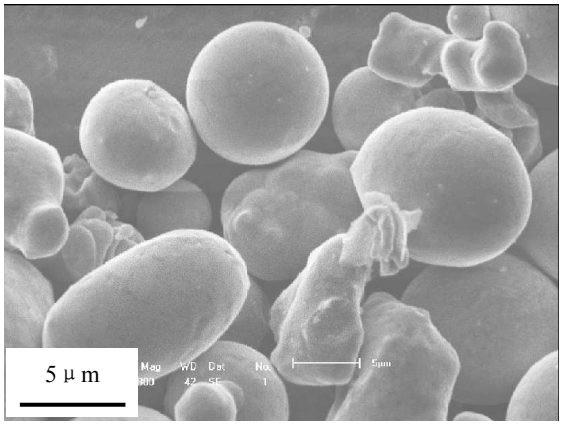

Fig. 2 SEM morphology of the copper particles

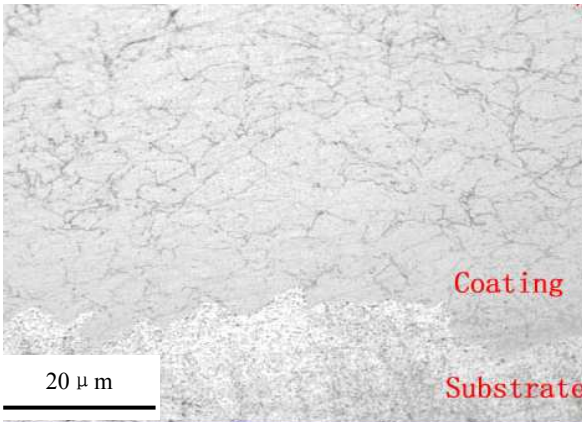

Fig. 3 Metallograph of the cross-sectional microstructure of the coating and the substrate

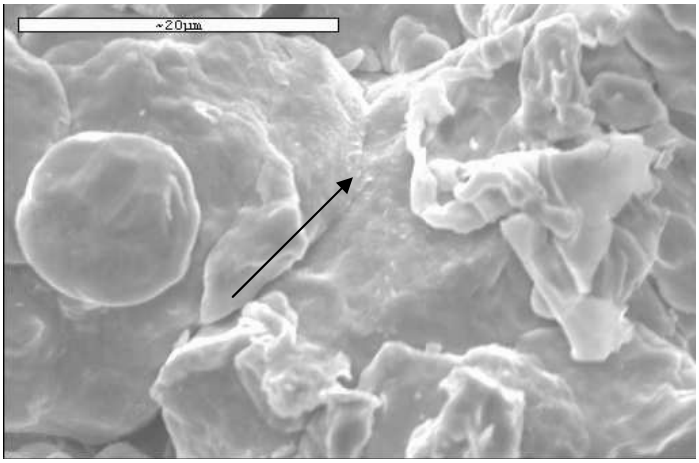

Fig. 4 SEM micrograph of the metallurgical bonding area (indicated by the arrow)

Microhardness of the coating

Table 3 shows the microhardness of the coating, and the microhardness of the as-casted copper is given for comparison. The average value of the microhardness of the coating is about 160, and that of the as-casted copper is about 92. The microhardness of the coating is 80% higher than that of the

Table 3 The microhardness of the coating and as-casted copper

Sample No.	Microhardness($HV_{0.2}$)			Average value
1	163	162	162	162.3
2	164	159	157	160.0
3	162	169	158	163.0
as-casted copper	83	96	96	91.7

as-casted copper. The particles were deformed severely during the cold spray process, and cold work harding and internal stress were induced onto the particles, which is the main reason for the increasement of the microhardness of the coating.

Conclusions

1. There is no oxidation occurred during the cold spraying process
2. The dense coating is deposited on the substrate. Mechanical bonding is the main mechanism for the interface between the coating and the substrate. Metallurgical bonding exists among the particles of the coating.
3. The microhardness of the coating is about 160Hv, which is higher than that of the bulk copper.

Acknowledgements

Part of the work is financially supported by the Doctoral Foundation of Henan University of Science and Technology.

References

[1] A.P. Alkimov, V.F. Kosarev, A.N. Papyrin, Dokl. Akad. Nauk SSSR 318 (1990) 1062
[2] C. Borchers, F. Gartner, T. Stoltenhoff, H. Assadi, H. Kreye, J. Appl. Phys. , Vol. 93 (2003), p. 10064.
[3] R.S. Lima, J. Karthikeyan, C.M. Kay, J. Lindemann, C.C. Berndt, Thin Solid Films, Vol. 416 (2002), p. 129
[4] J. Vlcek, L. Gimeno, H. Huber, E. Lugscheider, Thermal spray 2003: advancing the science and applying the technology, Orlando, Florida, USA, 5-8 May, 2003, in: B.R. Marple, C. Moreau (Eds.), Proceedings of the 2003 International Thermal Spray Conference, ASM International, OH, 2003, p. 37.
[5] T.H. Van Steenkiste, J.R. Smith, R.E. Teets, et. al. , Surf. Coat. Technol. Vol. 111 (1999), p. 62
[6] A. Alkhimov, Proceedings of International Thermal Spray Conference(ITSC-2002), Essen, Germany, 2002: 165-170

Advanced Materials Research Vols. 314-316 (2011) pp 74-77

doi:10.4028/www.scientific.net/AMR.314-316.74

Tribological properties of FeCrNi/CBN composite coating with spraying high Velocity arc

liu cunxiang[1,a], zhang junhui[2,b], wang zhaofeng[3,c]

[1]College of Science, Henan Agricultural University, Zhengzhou. Henan 450002, China;

[2]Henan Institute of Engineering, Zhengzhou. Henan 451191, China;

[3]Henan Vocational College, Zhengzhou. Henan 450046, China

[a]liucunxiang@henau.edu.cn, [b]junhui8802@yahoo.com.cn, [c]wang-z-feng@sohu.com

Keywords: high velocity arc spraying; composite coating; tribological characteristic

Abstract: The Tribological properties of FeCrNi/CBN composite coating with spraying high velocity arc is studied. Images and components and cross-section microstructure of coatings are analyzed by the means of SEM, and EDS etc. This research indicates that FeCrNi/CBN composite coatings have typical layered structure characteristic and high bond strength and hardness. Friction coefficient of coatings at room and high temperatures have "Run-up" period. With the increase of temperature, friction coefficient of coatings becomes low and wearing capacity of coatings becomes high. The adding of CBN powder highly improved the wearing capacity of coatings.

Introduction

High-velocity arc spraying technique (HVAS)is a new kind of thermal spraying technique.It processes many advantages. Jet velocity of melt drop is high. Distribution of melt drops atomized is homogeneous.Bond strength of coating is high. Porosity of coating is low[1]. In recent years, High-velocity arc spraying technique is being widely researched and applied. The quality of coating with this technique can be improved. The high economic benefit and social benefit have been achieved with use of this technique[2]. Currently, flux-cored wire was used in high-velocity arc spraying. It has the following advantages compared with solid-cored wire.

1）It has short cycle of production, cost low. So It is suitable for high velocity arc spraying. At present, flux-cored wire composite material, nano material and new alloy material be used as spraying materials. It is difficult to made solid-cored wire with above materials. But it is easy to put above material in flux-cored wire.

2）Chemical composition of flux-cored wire is adjusted easily. Some kinds of special characteristics coating can be achieved. And coating quality can be controlled conveniently. Compared with solid-cored wire, the problem that high hardness metal hard to be wiredrawed can be solved by use of flux-cored wire. Some insulating materials possessing special chemical elements only be used in coating as flux-cored wire. The powder not being alloyed is mounted in fused base surface of workpiece in coating as hard phase. The other metal droplet which has been alloyed fully becomes into solidified microstructure quickly. The metal droplet deposited can be re-melted with use of releasing heat to come from reaction of some unique metal elements. The performance of coating with flux-cored wire is excellent. The bond strength is enhanced greatly. The porosity is controlled efficiently. Oxide film is formed homogeneously. Stability of coating is improved[3-4].

Flux-cored wire(FeCrNi/CBN) was made by author in order to obtain coating of high hardness and wearing capacity. The FeCrNi/CBN composited coating was made successfully by high velocity arc spraying. Cross-section microstructure, thermal shock resistance, micro-hardness and wearing capacity is researched.

Test materials and methods

Flux-cored wire preparation Making flux-cored wires includes following steps:mixing powder according to certain proportion,rolling and wiredrawing wire, packaging and so on. 10mm × 0.4mmSPCC cold rolling steel strip was rolled as U-shaped section by forming roller. The powder were filled in U-shaped sedtion strip. The flux-cored wire is drawn into Φ2.5mm. The component of powders in flux-cored wire includes: CNB about 43%,Cr24%,Ni about 30%, a small amount of rare-earth metal. The filling rate of flux-cored wire with powder is 30%.

High-speed arc spraying process The coatings were produced by ZPG-400A type electric supply and QDIII-250V type HAVS gun. The parameters of spraying were the same for all coatings, i.e.voltage 32V,current 150-210A.The distance between workpiece and nozzle of gun is 180-250mm. Atomizing pressure is 0.45-0.5MPa. The thickness of coating is typically 300-400 μm.

Bond strength of coating and thermal shock resistance determined The bond strength of coating was determined by the method of dual sample test according to the ASTMC633-79 standard on material stretch test machine. The coating thickness is between 0.3mm-0.4mm. Each thickness of coating was messured wth five times.The average bond strength value is as the one of the coating.The thermal shock resistance of coating was determined with the qualitative analysis. The sample is as the same as one for the bond strength. Three groups of the samples were heated at three points of temperature (650℃, 700℃ , 750℃)in warm furance for 15 minutes. The samples were put into normal temperature water for cooling rapidly after which were removed from the furance.The action was reacted 15 times.Coating surface was observed whether or not the phenomenon of peeling,shedding, oxidative decoloration exist.

Coating micohardness measurement Coating micohardness measured by HX-500 durometec.Under 150g load and 30s residence time. They in the perpendicular direciton of coating substrate was measured according to 40 μm internal in order to observe the hardness distribution rules.

Determining the wear ing capacity of coating measurement The wearing capcity of coating is completed on MM-200 abrasion tester. Coating surface of sample is prepared as bottom wheel.03-0.4mm coating thickness was accomplished by grinding . Uper wheel is acted as the comparison pair of bottom one made up of number 45 steel quenched from 800° C. The weight difference of two wheels was measured by abrasion tester worked on 1000rings.

Coating micostructure analysis The sample was prepared, whose thickness of coating is about 0.6mm,which was made up of number 45 steel and whose finish size is 25mm×16mm×5mm.One piece of the sample in cross-section was prepared for observing. Cross- sectional microstructure was obersived by MODELL PME OLYMPUS optical microscope. Coating surface morphology was studied by Quanta200 scanning electron microscope(SEM).The chemical composition of coating section was analysised by Genesis 60s energy spectrometer.

Results and analysis

Bond strenth and thermal shock resistance The average bond strenth of coating is 30.5Mpa.The composite coatings of FeCrNi/CBN have high bond strenth. Because they have the following reasons:One is that the coefficient of thermal expansion of coating is low, so the internal stress of coating is small. One is that the room plasticity is improved by the mothod of adding element[5]. Last one is that the bond strenth of coating is improved with use of the exothermic reaction of Ni. Ni can form solid solution and compounded with Fe and Cr. Those effects can protect fresh surface against oxidization and to promote the reaction between droplet and substrate. Micro-area diffusion layer appears in the interface.

Tab.1 Bonding strength of FeCrNi/CBN coating(Mpa)

Test sample	1	2	3	4	5	average data
Data	30.9	30.8	30.6	30.2	30	30.5

Tab.2 Shock-resistance of FeCrNi/CBN coating

Test sample	650^0C 15times thermal shock	700^0C 15 times thermal shock	750^0C 15 times thermal shock
1	nothing	nothing	Color yellow and microcrack
2	nothing	nothing	Color a little yellow
3	nothing	nothing	Color blue

The result of thermal shock resistance are shown in table 2. It is easy to find that macro-defects between coatings and substrate haven't appear obviously in the conditions of fifteen times according to the order 650℃, 700℃ and 750℃. It shows a excellentlly thermal shock resistance.

The microhardness of coatings The transverse distribution of the microhardness on cross section of coatings in the perpendicular direction of substrate is shown in Fig 1 . It is easy to find that the averge microhardness of coating is 2-3 times of substrate's from Fig 1. There are some areas whose microhardness is very high., because they have hard phase element of CBN.The microhardness is relatively high also in certain areas. It is in conformity with dispersive distribution of oxide. In individual area of coating the microhardness is low. It shows that deficiency such as pore space exists in the coating. In addition , It is shown that microhardness changes gently from substrate to coating from Fig 1. It is benefit to improve bearing capacity of coatings and to decrease residual internal stress between coating and substrate.

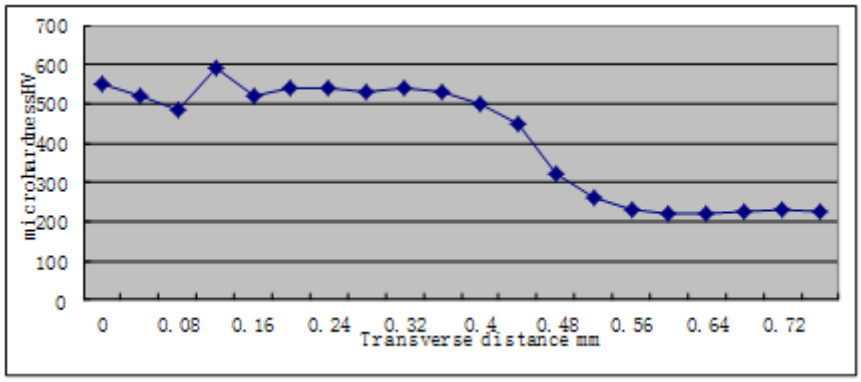

Fig.1 Hardness profile of FeCrNi/CBN coating along T direction

The wearing capacity of coatings the test results of wearing capacity of FeCrNi/CBN composite coatings are shown in Table 3. It is easy to find that wearing capacity of coating is good because there are hard phase elements of CBN which dispersively distribute. The hardness elements of coating in contact with wear material during the friction and wearing protect efficiently soft substrate and controll abatement of surface of workpiece, reduce abrasion loss of coating. Thereby, the coatings possesses good wearing capacity.

Tab.3 Wearing capacity of FeCrNi/CBN coating

coatings	Original weight(g)	Weight worn(g)	Weight loss(mg)	Wear resistance	Average
sample1	66.3907	66.0875	303.2	6.3532	6.4240
wheel1	64.7623	62.8360	1926.3	1	
sample2	64.6201	64.3125	307.6	6.2893	
wheel2	75.1439	73.2093	1934.6	1	
sample3	69.2715	68.9779	293.6	6.6297	
wheel3	72.8216	70.8751	1946.5	1	

Coating microstructure Fig 2 shows the micrograph of the cross section of FeCrNi/CBN composite coatings. The typical lamella structue of coatings were shown by Fig 2. Organization of coating is dersification and it has not bulky pore space. Some irregular flat particles are found for example A point in coatings. The observing results of SEM and EDS are shown in Fig 3 and Table 4, It indicates that particles are CBN. Element distribution map in the region is shown in Fig 4 through observing the region arrounding the CBN particles . Table 4 shows the chemical compositions of FeCrNi/CBN composite coatings. Through analysis, It indicates that metal of around CBN surface is melted in spraying process. CBN as a core surrounded by melted metal powder hits against the suface of substrate.Dense coatings is formed in process of coating expansion.

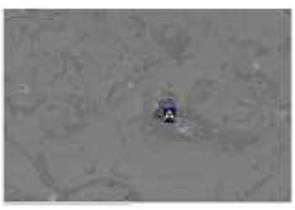

Fig.2 Structure of FeCrNi/CBN coating

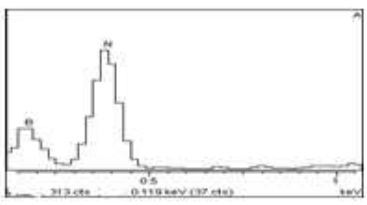

Fig.3 EDS spectra of FeCrNi/CBN coating

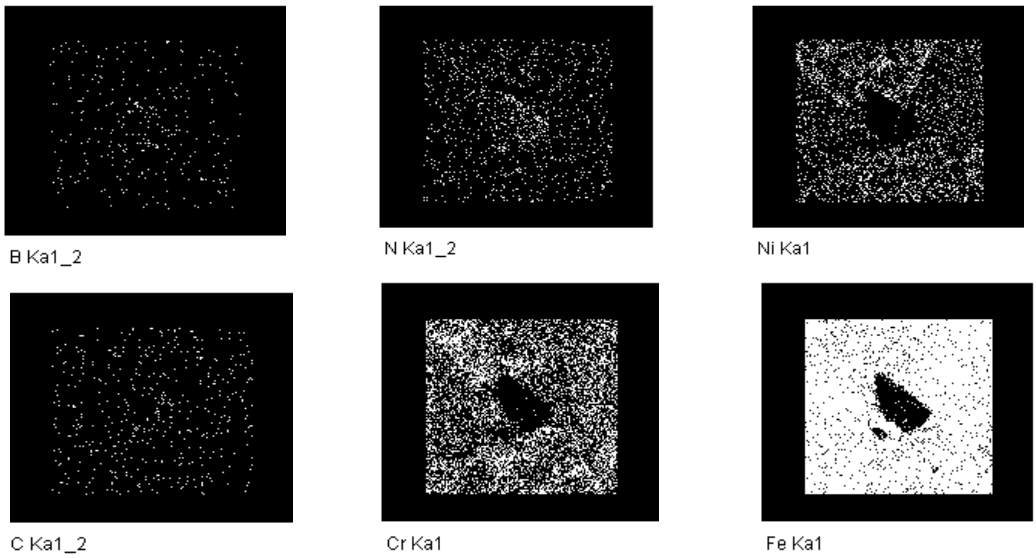

Fig.4 The face composite of FeCrNi/CBN coatings distribution element distribution map of the region

Tab.4 Chemical compositions of FeCrNi/CBN coatings by EDS (w(x))

Elements	B	N	C	Ni	Cr	Fe
w(x)	17.42	22.56	3.28	21.36	16.32	margin

Conclusion

(1) The FeCrNi/CBN composite coatings by HVAS have characteristics of high bond strength and compactness.
(2) The bond strength of FeCrNi/CBN composite coatings by HVAS is 30.5 Mpa. It has excellently thermal shock resistance.
(3) The results of the microhardness of the coatings indicate that the average hardness is high. Microhardness changes gently from substrate to coating . It is benefit to improve bearing capacity of coating and to decrease residual internal stress between coating and substrate.
(4) The results of dynamics performance experiments of coating indicate that synthesize dynamics performance of FeCrNi/CBN composite coatings is good. The typical lamella structure of coating was shown.
(5) The FeCrNi/CBN composite coatings have excellent wearing capacity. It can be used as wearing surface of workpiece in order to reduce loss by wearing.

Acknowledgements

Corresponding Author: Wang Zhaofeng. Tel：+86- 0371-63558132;Fax:+ 86-0371-63558132;E-mail: wang-z-feng@sohu.com

References

[1] Zhu Shaohua Xu Binshi, The Theory and Technology of Surface Engineering [M].Beijing. Defense Industry Press, 1999:259-268.
[2] Wen Jinlin. The Application of Arc Spraying Technology [J].Journal of Surface Engineering, 1994 (2). 16-31
[3] Tian Zhiling, Pan Chuan Liang Dongtu. Flux-cored Wires [M].Beijing. Metallurgical Industry Press, 1999:1-8.
[4] Xu Weipu, Xu Binshi. HVAS Iron Aluminium Core Silk Material Research and Performance Analysis [J]. Journal of Hubei Automobile Industry Institute.2004 (3) : 15-18.
[5] Sun Yangshan, Guo Jun, Zhang Lining etc. Effects of Ce and Cr on Room Temperature Mechanical Properties of Fe_3Al [J].Acta Metallurgica Sinica. 1991,27 (4) : A255-260

Advanced Materials Research Vols. 314-316 (2011) pp 78-81

doi:10.4028/www.scientific.net/AMR.314-316.78

Simulation of the Effect of Process Parameters on Particle Velocity in Cold Spray Using Laval Nozzle with Nine Holes

Chuanshao Liu[a], Yaohui Jin[b] and Jianxin Zheng[c]

Henan Polytechnic University, Jiaozuo 454003,P.R.China

[a]lcs@hpu.edu.cn, [b]jinyaohui130@163.com, [c]zhengjx@hpu.edu.cn

Keywords: Cold spray; Simulation; Laval nozzle with nine holes; Particle velocity.

Abstract. Simulations of the supersonic flow field inside and outside of the Laval nozzle with single hole and nine holes were carried out based on the computational fluid dynamics method. The effects of different standoff distance and particle diameter on impact velocity of Cu particle spraying from single hole and nine holes were investigated firstly. The results show that the particle velocity obtained with the nine holes nozzle is higher than that of the single hole nozzle under the same standoff distance, and the smaller the standoff distance, the higher the particle velocity may be obtained with the nine holes, and the higher particle velocity may be obtained with smaller particle diameter for particles with diameters of 1 ~ 15 μm. Furthermore the effects of different spraying pressure and temperature on particle velocity of Cu particle spraying from the nine holes nozzle were also studied. And the simulations indicate that the higher the spraying pressure and temperature may make the particle spraying with greater velocity.

Introduction

The standoff distance (SoD) between the nozzle and the substrate is one of the important parameters in the cold spray process, and which influences the particle impact velocity directly. Many scholars have focused on this problem. Pattison [1] found that a bow shock was formed at the impingement zone between the supersonic jet and the substrate when the SoD was small, and the bow shock was detrimental to the process performance as it reduced the particle impact velocity. His study also showed that the deposition efficiency was closely related to the SoD, and the bow shock reduced deposition efficiencies by as much as 40% under the SoD is less than 60mm when using a custom-made helium nozzle, operating at 2.0 MPa and 20^{o}C. Alkhimov [2] found that the thickness of the compressed layer which formed between the bow shock and substrate depended on SoD when spraying air and helium, and the smaller the SoD, the thicker the compressed layer. His research also showed that aluminum particles less than 5μm in diameter could be decelerated obviously in the compressed layer. Gilmore [3] and Dykhuizen [4] also found that the particles less than 5μm in diameter could be decelerated and even deflected away from the substrate by the bow shock.

The Laval nozzle with nine holes was used in this study in order to reduce the adverse effects of bow shock on particle impact velocity so as to obtain the better spraying effects under the same conditions of the nozzle exit area compared with the Laval nozzle with single hole.

Theoretical Models

Mathematical model. Compressible flow is a very complex and comprehensive phenomenon, and the actual flow of the nozzle is non-constant isentropic flow in the actual conditions. The flow inside of the nozzle is considered as a steady isentropic flow in theory so as to simplify the simulation. The governing equations used to describe the process are as follows [5].

Continuity equation: $\frac{\partial \rho}{\partial t} + \nabla \bullet (\rho u) = 0$;

Momentum equation: $\frac{\partial}{\partial t}(\rho u) + \nabla \bullet (\rho u u) = -\nabla p + \nabla \bullet \bar{\bar{\tau}}$;

Energy equation: $\frac{\partial e}{\partial t} + \nabla \bullet [(e + p)u] = \phi_D + \nabla \bullet (k \nabla T)$;

Equation of state: $p=\rho RT$

Where u, p, and T represent the flow velocity, pressure and temperature; ρ, $\bar{\bar{\tau}}$, and k represent the flow density, viscous stress tensor and thermal conductivity, respectively; e, φ_D are the stagnation internal energy per unit volume and viscous dissipation, respectively.

Particles can be considered as discrete phase in the continual gas flow, and the acceleration of a spherical particle by the gas flow can be expressed by the following equation when the interaction between the particles and gravity is ignored [6]:

$$\frac{du_p}{dt} = \frac{3C_D \rho}{4 d_p \rho_p}(u - u_p)\left|u - u_p\right|$$

Where u_p, d_p, ρ_p represent particle velocity, diameter and density; C_D is drag coefficient and expressed for a smooth spherical particle by $C_D = a_1 + a_2 / R_e + a_3 / R_e$ and a_1, a_2, and a_3 are constants, R_e is the Reynolds number and defined by: $R_e = \rho d_p \left|u_p - u\right| / \mu$ and μ is the fluid dynamic viscosity and this equation can be practically applied to a R_e<50000.

Geometrical model. The jet flow region in cold spray process is made up of the internal flow of the nozzle and free jet flow region. Due to the use of nine holes nozzle, a three-dimensional model is built up in this study. Fig.1 shows the exit section diagram of the nine holes nozzle, and there are eight small holes with diameter of 1.67 mm uniformly distributed and a center hole with diameter of 2.6mm in the circular face with diameter of 6.4mm. The distance L (as shown in Fig.1) between the small hole and center hole is 2.25mm, the total area of the nine holes equals the exit area of the single hole with diameter of 5.4mm. Other dimensions of the Laval nozzle with nine holes are identical to the single hole nozzle, Fig.2 shows the section diagram of the Laval nozzle with single hole and computational domain, and its main dimensions are shown in table 1.

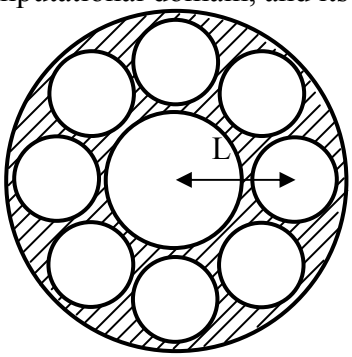

Fig.1 Exit section diagram of the Laval nozzle with nine holes

Table 1 Main dimensions of the Laval nozzle with single hole

Inlet diameter(mm)	8
Convergent length(mm)	23
Divergent length(mm)	40
Throat diameter(mm)	2.7
Exit diameter(mm)	5.4
SoD(mm)	20

Boundary conditions and solving method

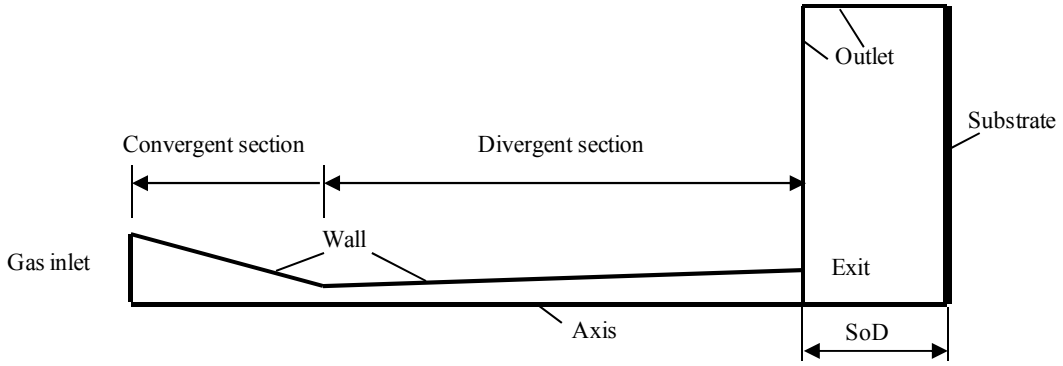

Fig.2 Section diagram of Laval nozzle with single hole and computational domain

Gas inlet as shown in Fig.2 is selected for the pressure inlet boundary condition, and outlet is selected for the pressure outlet boundary condition which is atmosphere pressure and room temperature. And the air is selected as the accelerating gas.

The standard k-ε turbulence model is utilized to disperse turbulence flow of gas, and standard wall functions are used to deal with the near wall region. Second-order upwind discretization scheme is used for governing equations. The computation of discrete phase follows the continuous phase flow field.

Results and discussion

Effect of SoD on particle velocity. The impact velocities of Cu particles with diameter of 2μm sprayed by the Laval nozzle with the single hole and the nine holes are shown in Fig.3 with different SoD when spraying pressure P is 2.5MPa and spraying temperature T is 700K. It is seen clearly that the particle velocities obtained by the Laval nozzle with nine holes is higher than that of by the Laval nozzle with the single hole in the same simulation conditions. And the smaller the SoD, the higher the particle velocity may be obtained by the Laval nozzle with nine holes. It is also seen that the optimum SoD is 40mm when the Laval nozzle with single hole operates at P=2.5MPa and T=700K.

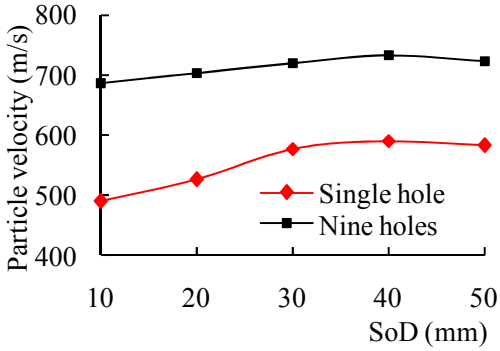

Fig.3 Effect of SoD on particle velocity

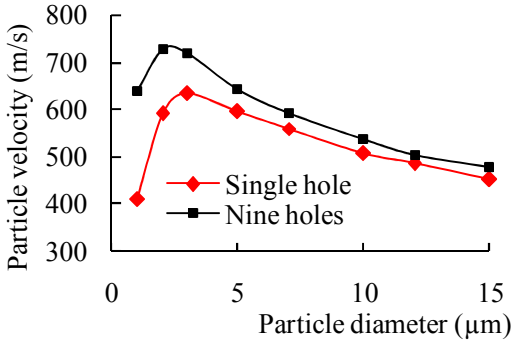

Fig.4 Effect of particle diameter on particle velocity

When using the Laval nozzle with single hole, a series of compress waves are produced by the supersonic gas flow due to sharp compression before the substrate. And the shock wave will occur when the compression waves stacking with each other. Supersonic gas flow becomes subsonic gas flow when it goes through the shock wave, and the pressure, density, temperature of the gas flow rises sharply, while Mach number drops rapidly. The particle velocity decreases continuously owing to shock wave's effect. The intensity of shock wave before the substrate also increases consequently with the decreasing of SoD, so does the influence on particle velocity.

The gas flow tends towards stability, and so is the particle velocity when using the Laval nozzle with nine holes.

Effect of particle diameter on particle velocity. Fig. 4 shows the effect of particle diameter on particle velocity when the Cu particles pass through the Laval gun to the substrate at the simulation conditions of SoD=40mm, P=2.5MPa and T=700K. It is seen clearly that the higher particle velocity may be obtained with the smaller particle using different Laval nozzle, while the particle velocity obtained by the Laval nozzle with nine holes is higher than that of the Laval nozzle with single hole at the same conditions.

The particle velocity decreases rapidly by the effect of shock wave before the substrate because the small particle has much low mass, low inertia and influenced by the gas easily. While using the Laval nozzle with nine holes, particle velocity has a little change as the intensity of shock wave is diminished. The greater particle has higher weight, higher inertia and can not be accelerated easily by the gas, so the variation of the particle velocity is not apparent by the effect of shock wave before the substrate. Therefore the Laval nozzle with nine holes is appropriate for the small particles.

Effect of pressure on particle velocity. Fig. 5 shows the effect of pressure on particle velocity when the Cu particles pass through the Laval gun with nine hole to the substrate at the simulation conditions of SoD=40mm, T=700K and the diameter of the Cu particle is 2μm. The distance x as shown in Fig.5

is from nozzle inlet to the substrate. It is seen clearly that the particle velocity has a little change and tends towards stability between the exit of nozzle and the substrate. With the increment of spray pressure, the particle velocity also has little change inside of the nozzle and small increase outside of the nozzle. Therefore there is little effect of the pressure on particle velocity.

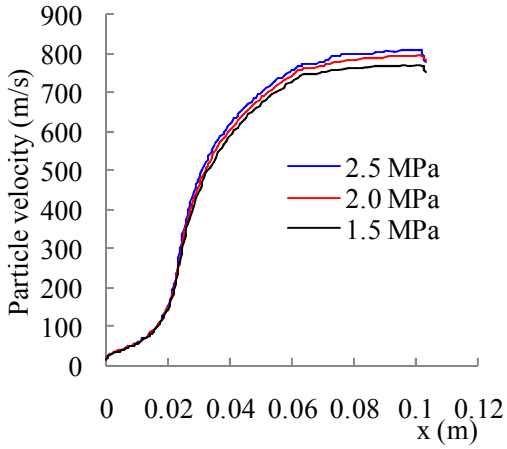

Fig.5 Effect of pressure on particle velocity

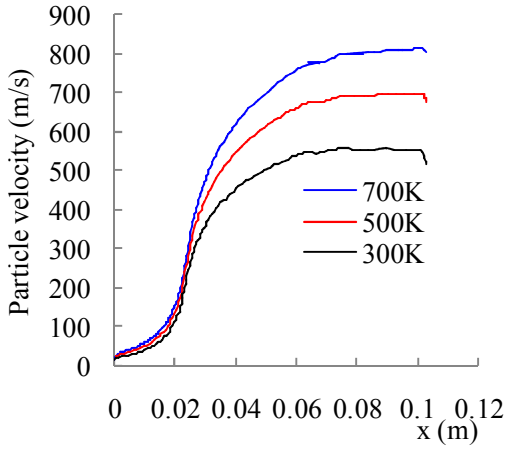

Fig.6 Effect of temperature on particle velocity

Effect of temperature on particle velocity. Fig. 6 shows the effect of temperature on particle velocity when the Cu particles pass through the Laval gun with nine hole to the substrate at the simulation conditions of SoD=40mm, *P*=2.5 MPa and the diameter of the Cu particle is 2μm. It is seen clearly that the effect of the spray temperature on particle velocity is large, and the higher the temperature, the higher the particle velocity. Furthermore, the massive plastic deformation occurs easier in both the incident particles and the substrate with the higher temperature.

Conclusions

(1) The particle velocity obtained by the Laval nozzle with nine holes is higher than that with the single hole at the same standoff distance, and the smaller the standoff distance, the higher the particle velocity may be obtained by the Laval nozzle with nine holes.

(2) The higher particle velocity may be obtained with smaller particles using the Laval nozzle with nine holes at the same conditions.

(3) The higher the spraying pressure and temperature may make the particle spraying with greater velocity using the Laval nozzle with nine holes.

References

[1] J. Pattison, S. Celotto, A. Khan. Surface & Coating Technology, Vol. 202 (2008), p. 1443-1454.

[2] A. P. Alkhimov, S. V. Klinkov, et al. Journal of Applied Mechanics Technical Physics, Vol. 38, No. 2 (1997), p. 324-330.

[3] D. L. Gilmore, R. C. Dykhuizen, et al. Journal of Thermal Spray Technology, Vol. 8, No. 4 (1999), p. 576-582.

[4] R. C. Dykhuizen, M. F. Smith. Journal of Thermal Spray Technology, Vol. 7, No. 2 (1998), p. 205-212.

[5] Hidemasa Takana, Kazuhiro Ogawa, Tetsuo Shoji. Powder Technology, Vol. 185 (2008), p. 116-123.

[6] Wen-Ya Li, Hanlin Liao, G. Douchy. Materials and Design, Vol. 28 (2007), p. 2129-2137.

Advanced Materials Research Vols. 314-316 (2011) pp 82-85

doi:10.4028/www.scientific.net/AMR.314-316.82

Synthesis and Properties of Poly-Acrylate Emulsion Modified by Organ Silicone

Yuxin Liu [a], Yaohui Lv [b], Shu Zhang, Fujia Xu , and Binshi Xu

Science and Technology on Remanufacturing Laboratory, Academy of Armored Forces Engineering, Beijing, 100072, China

[a] lyxinbgd@163.com, [b] yaohui.lv@163.com

Keywords: acrylosilane emulsion; vinyltriethoxy silane; modification; properties; water absorption

Abstract: An acrylate emulsion was modified by vinyltriethoxy silane (VTES, trade name A-151) to synthesize the acrylosilane emulsion with high properties. The effect of the amount of A-151 on the properties pf the emulsion was investigated. It found that adding 6 % of A-151, the fraction extensibility of the emulsion film could be increased to 530 % and its water absorption was reduced to 4.2 % while adding 10 % of A-151. On the other side, the particle size and distribution of the emulsion were analyzed by Scanning Electron Microscopy (SEM) and Malvern Particle Size Analyzer (PSA) respectively. The measuring results showed that the particle diameter of the modified emulsion could be between 100 and 700 nanometers, and the properties of the emulsion could be apparently improved by adding A-151 into the system of emulsion polymerization.

Introduction

Acrylosilane emulsion has become an excellent film former because of its resistance to temperature, climate, water and hardness. It shows great promise in construction and decorates for the future [1]. With the development of the theories and technologies of polymerization and environment friendly emulsions, modifications of acrylate emulsions become more and more important. In the past decade, many authors reported various strategies, for example, Gan Meng-yu et al [2-5] studied the preparation methods and the characteristics of acrylosilance emulsions; and STOFFR J et al [6-8] researched the structure and properties of acrylosilance emulsions. Although modifications had been successful in controlling the particles size and their distribution and polymerization [9], some problems still existed in the preparation, for example, hydrolysis and polycondensation of the bulky alkoxy in the alkoxy silane bring on bad store stability of emulsions.

In this paper, copolymerizing the two polar monomers of acrylate and alkoxy silane for composing an acrylosilane emulsion with excellent properties was proposed. Using an alkoxy silane, vinyltriethoxy silane (VTES, trade name A-151), as functional monomer, it has bulky alkoxy substituents, so that its hydrolysis reactivity was reduced and the stability of the emulsion in the polymerization process was raised. When the film was dry, hydrolysis and polycondensation of the alkoxy silane could form firm solid-gridding (-si-o-si-) framework that could enduce with water and adhesion resistance on the film. The water absorption of the emulsion film was reduced. The prepared emulsion had excellent properties, so it could be used to make exterior wall coating and waterborne rust-based coating.

Experimental

Materials. Methyl methacrylate(MMA), butyl acrylate(BA), acrylic acid(AA), sodium dodecyl sulfate(SDS), octyl phenolic divinyl oxide(OP-10), vinyl trioxyhemoglobin silane(A-151), were selected from commercial grades available in Chinese company. A water soluble initiator potassium persulfate (KPS) was used. Each of these chemicals was used without further purification. The water used in all experiments was purified by distillation.

The specific formulation is listed in table 1.

Table 1 Experimental formulation

Materials	MMA	BA	AA	A-151	SDS	OP-10	KPS	H_2O
Weight (g)	40	44	4	5.6	1	3	0.4	110

Synthesis of the acrylosilane emulsion. The emulsion was synthesized in a 500ml four-necked, round-bottomed flask equipped with a mechanical stirrer, condensation tube and thermometer. First, 4g emulsifier and 100g deionized water were put into the flask and heated in a water bath at 75～80℃, the mixture was stirred in order to emulsify completely. Then 0.4g of the initiator and all the monomers were added slowly over 3～4h, then the reaction was allowed to proceed more than 2h to improve the conversion of the monomers. At last, the emulsion was cooled to ambient temperature and its pH value was adjusted to 7～8 by adding aqua ammonia.

Testing of the acrylosiane emulsion. The Scanning Electron Microscopy (SEM) and MAF-5001 Malvern Particle Size Analyzer were used to test the particles diameters and distribution of the acrylosilance emulsion.

Results and discussion

Influence of alkoxy silane monomers. For the coating prepared from the acrylosilance emulsion, the alkoxy silane group in the polymer chain could be hydrolysed to alkoxy alcohol in the process of filming [10]. The properties of the coating film were improved, such as the water resistance, adhesion and fraction-extensibility. A-151 was selected as a functional monomer to study its influence on the properties of the coating film. When the amount of A-151 increased, the fraction-extensibility increased and the water absorption of the coating film decreased, which showed as Figure 1 and Figure 2.

The rising curve in Fig. 1 meant that with the addition amount of A-151 increasing, the fraction-extensibility of the coating film was raised. When the amount of A-151 increased from 1% to 6 %, the fraction-extensibility of the film increased from 440 % to 530 %, but the amount of A-151 was above 6 %, the fraction-extensibility of the coating film was dropped.

Figure 2 showed that the water absorption rate of the film decreased with the adding amount of A-151increased, adding A-151 from 1% to 10%, the water absorption decreased from 15.6 % to 4.2% that meant there was a good way to improve the water resistance of the coating film. The reason was that the A-151 as a function monomer was hydrophobic; there were reactive vinyl andalkoxy in the A-151. Vinyl took part in the reaction with orylic acid ester. On the base of polymer, hydrolysis and polycondensation of the alkoxy in the alkoxy silane, brought on solid-gridding framework, which enhanced the water resistance of the film [11]. So it could be used for water proofing materials.

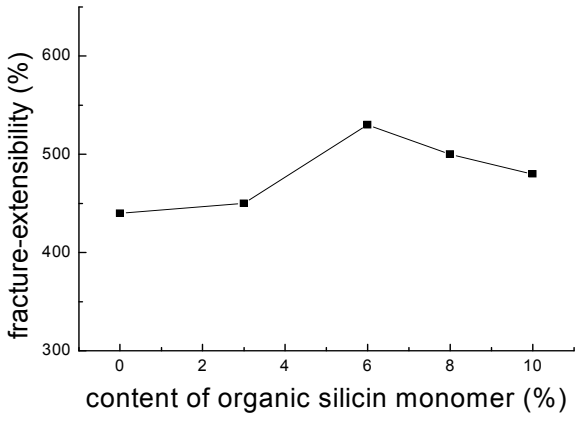

Fig1 Variety of fracture-extensibility on emulsion film

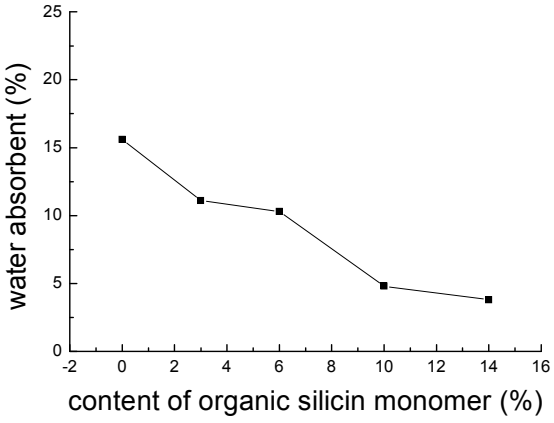

Fig2 Effect of organic silicon monomer content on film water absorbent

Increasing A-151 up to 14%, the water resistance could be improved effectively. Nothing the curves in the Figure 1 and Figure 2, it could be found that the optimal amount of A-151 is at 6% and 8%.

Analysis of Malvern Particle Size Analyzer（PSA）. The emulsion particle size was related to the stability and even film. The smaller diameter of emulsion could improve its wetness on the pigment, endued the coating polish, increased the pervasion of the coating to the base, and enhanced the ornament purpose of the coating. The narrow distribution of the particles could raise the store stability and properties of the emulsion.

The acrylosilan emulsion was analyzed its particle size with MAF-5001 Malvern Particle Size Analyzer (PSA). The results were presented as Figure 3.

According to Figure 3, the diameters of the acrylosiane emulsion particles were between 100 and 700 nanometers, and more over the distribution of the particles were even, the average diameter of the emulsion particles was 300 nanometers.

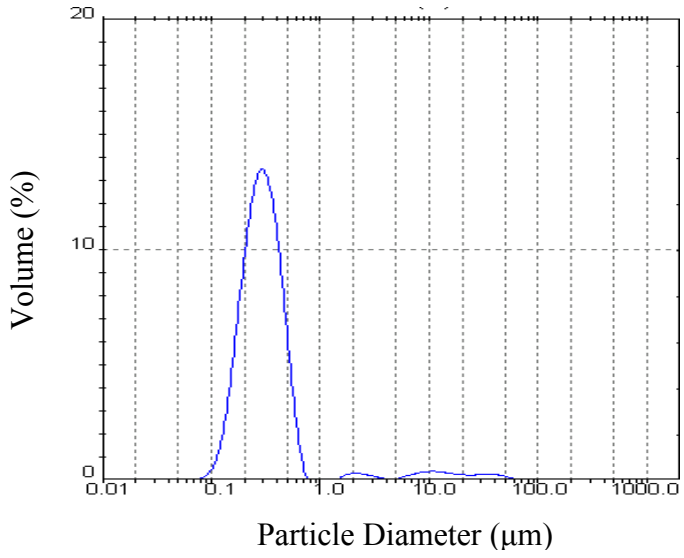

Fig 3 Particle Diameter of silicone-acrylate emulsion

Analysis of Scanning Electron Microscopy (SEM). Figure 4 showed that the picture of Scanning Electron Microscopy about the acrylosilane emulsion film. The picture was 300 times and 3000 times the real size of the emulsion particles, moreover the distribution of the particles was even. But there were some smaller particles partially except these good distribution ones. This was because that the particles became into cores constantly throughout the whole process of polymerization, the new particles were born again and again from the beginning to the end, at last there were some particles that still could not become cores and preserved in productions.

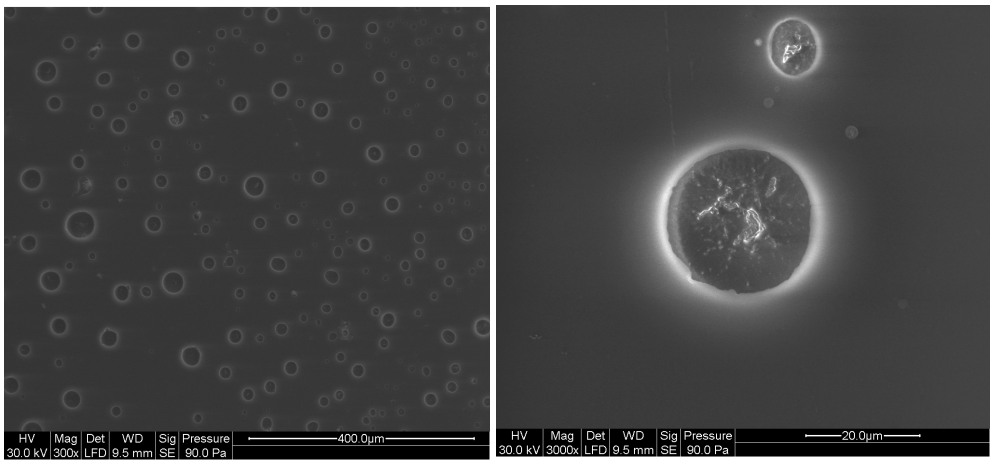

Fig.4 SEM spectra of silicone-acrylate emulsion

The micro shape of the acrylosilane emulsion in Figure 4 was regulation, the reason was that the two polar monomers, the function monomer (vinyltriethoxy silane) and the initiator were added slowly at the same time. The polymerization proceeds in the circumstance of weak acid, the hydrolysis and polycondensation reactions were restrained to reduce the diameter of particles, and eventually came to the even distribution of particles in narrow scope, of course the properties of the emulsion could be improved.

Conclusions

A novel acrylosilane emulsion was synthesized with acrylate monomers and vinyltriethoxy silane (trade name A-151). The main advantages of A-151 lay in its ability to improve the fraction extensibility and water resistance of the emulsion film. A-151 could restrain its hydrolysis and polycondensation reaction efficiently to reduce the diameters of particles in the scope of 100 and 700 nm with good distribution of particle size. The results showed that the modification with A-151 was an efficient method to improve properties of the emulsion. The prepared acrylosilane emulsion used as environment friendly exterior wall coatings and rust-based paintings. So it was expected to find applications widely in the coatings industry where high-performance materials were required, and it showed great promise for the future.

Acknowledgements

This work was financially supported by the Natural Science Foundation of China (50675223), and the Natural Science Foundation of Beijing Municipality (2012004).

References

[1] Ming J C, Fred D O and Eric R P.: Coat Techn., Vol. 69(1997). P. 43.
[2] Mengyu Gan, En Yue and Jianbing Hong: Pant & Coatings Industry (in Chinese), Vol. 38(2008). P. 8-10.
[3] Guofang Gu: Henan Chemical Industry (in Chinese), Vol. 5 (2002). P. 18-21.
[4] Xinya Zhang, Renhua Lan and Huanqin Chen: Fine Chemicals (in Chinese), Vol. 5 (2004). P. 383-385.
[5] Yuxin Liu and Sheng Meng: Chemistry and Adhesion (in Chinese), Vol. 29 (2007). P. 257-261.
[6] STOFFRJ. BONET: Journal of Polymer Science Polymer Chemistry Edition, Vol. 18 (1980). P. 2641-2648.
[7] Zhibao Qing and Aiqing Zhang: Journal of South-central university for Nationalities (in Chinese), Vol. 22 (2003). P. 20-24.
[8] Dongqing Wei, Baolian Zhang and Guoxiang Cheng: Paint& Coatings Industry (in Chinese), Vol. 36 (2006). P. 4-7.
[9] M. J. Chen, A. CHABES and F. D. Osterholtz: Surface Coating International, Vol. 79 (1996). P. 539-542.
[10] Larpent C and Tadros T F: Colloid Pdymer Sci, Vol. 269 (1991). P. 1171-1176.
[11] Jing Chen, Huaping Su and Zhonghua Li: Silicone material (in Chinese), Vol. 19 (2005). P. 12-14.

Advanced Materials Research Vols. 314-316 (2011) pp 86-93

doi:10.4028/www.scientific.net/AMR.314-316.86

Application of Taquchi Method in the Optimization of PTA Hardfacing Process

Hung-Shyong Chen [1, a], Jeng-Nan Lee [1], Huang-Kuang Kung [1]

[1] Department of Mechanical Engineering, Cheng Shiu University, Kaohsiung, Taiwan, R.O.C

[a] e-mail: hschen@csu.edu.tw

Keywords: PTA, Hardfacing layer, Wear-resistant plate, Dilution rate, Wear, Taguchi method.

AbstractThe application of Taquchi method in the optimization of PTA hardfacing process for the wear-resistant plate has been studied in this paper. The operation current, powder feeding rate, torch moving rate and torch moving distance are the four factors evaluated in this research. Taguchi methodology is applied to make the association of these factors in optimization and through the observation of microstructure, hardness, wear-resistance and dilution rate to evaluate the effects of these factors on the hardfacing layer of the wear-resistant plate. By the microstructure observation, the more sturdy and compact of the Cr-C dendrite structure, the better the hardness and wear-resistance of the hardfacing layer is. The torch moving distance is the major factor of the surface hardness, and the torch moving rate for the wear, the working current for the dilution rate.

Introduction

According to Crook [1], the principle of the hardfacing process is to weld a layer of wear-resistant and/or corrosion-resistant material on the surface of raw material by metallurgical bonding, due to the large thickness variation, it easy to appear cracks penetrated hardfacing layer through the plate width direction, the welding area is also limit in flux cored wire. Hsu et al. [2], evaluated the hardfacing methods, and found the PTA has best filling rate and dilution rate, and least of welding defects.

Compared to flux cored wire welding, PTA has the advantages of low dilution rate, easy automation, suitable materials and wide range of selection, the first proposed is in 1960s from AWS[3], many scholars have completed the related studies of this processing technology [4~17]. Based on the above, this study is to apply PTA hardfacing process for the wear-resistant plate production to improve the manufacturing efficiency.

Experimental Procedures

The process factors working current (A), powder feeding rate (B), torch moving rate(C) and torch moving distance (D) are selected to evaluate the effects on the hardfacing process quality. Taguchi methodology is used to design the process factors based on the objectives of high carbon ferrochrome distribution rate, high hardness, wear-resistant and low dilution rate, and to establish the optimization process factor configuration for the wear-resistant plate production.

Specimen Preparation

Low-carbon steel with 0.3% carbon content is used as a base and the dimension is 400mm×200mm×4mm. Due to the thermal stress effect, the base may produce a flexural distortion when the input heat is too high. To avoid this phenomenon, the Chen's patent [18] is used to control the plasma torch moving height. After the welding, first visual check the hardfacing layers if there is any crack through the base or the whole plate distortion. Then hammer the hardfacing layer to check whether it was false welding to preliminarily determine the welding quality for the following tests.

Taguchi Methodology

From the Taguchi methodology, the control factors are working current (A), powder feeding rate (B), torch moving rate (C) and torch moving distance (D). Each factor has three levels for analytical testing. The orthogonal array L_9 (3^4) (with specimen No.) and the levels are given in Tables 1 and 2.

Table 1 Orthogonal array $L_9(3^4)$

EXP (Specimen No.)	A	B	C	D
1	1	1	1	1
2	1	2	2	2
3	1	3	3	3
4	2	1	2	3
5	2	2	3	1
6	2	3	1	2
7	3	1	3	2
8	3	2	1	3
9	3	3	2	1

Table 2 Levels of control factors

Parameter	Description	Level 1	Level 2	Level 3
A	Working current(A)	150	180	200
B	Powder feeding rate (g/min)	40	45	50
C	Torch moving rate (mm/min)	1000	900	800
D	Torch moving distance (mm)	20	25	30

Microstructure Observation

After polishing the specimens, the microstructure and the chromium carbide distribution of the hardfacing layer can be observed and analyzed by microscope. The hardfacing layer's components were also analyzed by using Scanning Electron Microscopy (SEM) and Energy Dispersive Spectrometer (EDS).

Analysis of Surface Hardness

The objective surface hardness of the hardfacing layer is HRc58~64. The average hardness of hardfacing layer can be obtained by 9 spots measurement. Also, the cross-sectional hardness distribution of the hardfacing layer, and the hardness of chromium carbide particles are analyzed.

Analysis of Wear

The abrasion test is according to ASTM G65-94 [19], the specimen size is 76×25×3.1~12.7(mm). The overall thickness of the specimen used in this experiment is about 9mm (base for 4mm, hardfacing layer for 5mm). Before the test, the specimens need to go through milling and polishing process according to the standard specification. The testing parameters are shown in Table 3.

Table 3 The parameters of abrasion test

Press load	130±3N (about 12.85kgf ≤ F ≤ 13.65kgf)
Sand flow rate	300~400g/min
Rubber wheel speed	200±10rpm
Wheel revolutions	2000 (The B test method in ASTM G65-94)
Abrasive material	Quartz sand (AFS 50-70 TESTING SAND)

Analysis of Dilution Rate

According to the reference [17], the elemental composition method is used to calculate the dilution rate. A higher dilution rate means that more key alloy in the hardfacing layer was diluted to the base metal, which will reduce the hardfacing layer wear resistance. Therefore, the manufacturing process would always try to control the dilution rate as low as possible. The Scanning Electron Microscopy

(SEM & EDS) is used to analyze the Fe content (%) of the hardfacing layer. From the reference [6] shows that in the PTA manufacturing process, the gradient change of elements concentration only happened around the interface between the hardfacing layer and the base within a very narrow range (about the number of 10μm). Therefore, the analysis position is between the half thickness and the surface of the hardfacing layer. The dilution rate D is defined by the following formula:

$$Dilution\ rate\ (\mathrm{D}) = \frac{hardfacing\ \ layer\,(\mathrm{Fe\%}) - original\ \ welding\ \ materials\,(\mathrm{Fe\%})}{Base\,(\mathrm{Fe\%}) - original\ \ welding\ \ materials\,(\mathrm{Fe\%})} \times 100\% \quad (1)$$

Results and Discussion

The Taguchi methodology used to analysis the wear-resistant plate includes surface hardness, wear rate, and dilution rate. The microstructures were also observed to compare the structure and the distribution of chromium carbide Cr-C of specimens No.1 to No.9.

Microstructure Observation

From the microstructure images, the Fe-C base appears to be in gray-black color and the Cr-C is in bright white color with needle or granular constituent, which are shown in Fig. 1 and Fig. 2. The Cr-C dendrite structure precipitated in No.2, No.3, No.5, No.9 specimens are more sturdy and compact, with Cr-C distribution rates about 35~50%. Contrarily, the dendrite structure in No.1, No.4, No.7, No.8 specimens are more slender and sparse, the Cr-C distribution rates are about 31~35%.

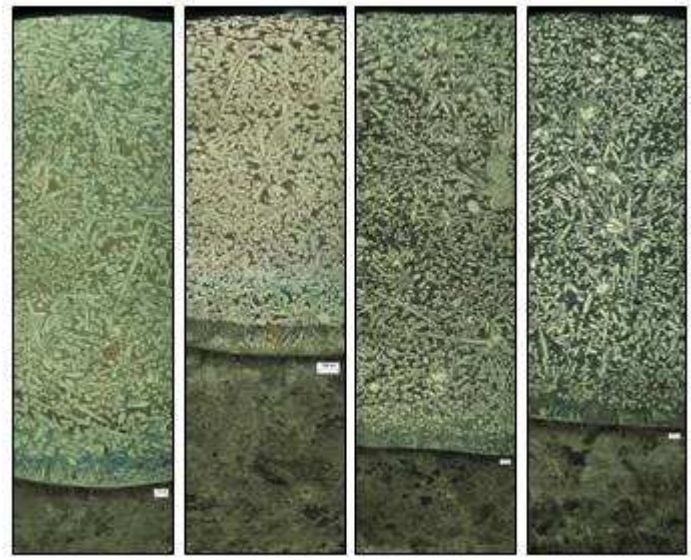

No.2 No.3 No.5 No.9

Fig. 1 The specimens' microstructures (X50)

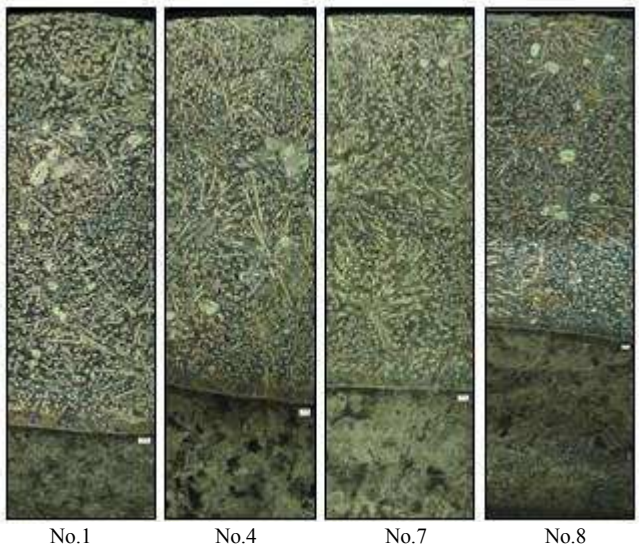

No.1 No.4 No.7 No.8

Fig. 2 The specimens' microstructures (X50)

While producing hardfacing layer of specimen No.6, the PTA's spark plug was blocked which effects on powder feeding rate. A second welding was made on it therefore the structure has double hardfacing layers. From the specimens' microstructure profile, hardfacing layer A (the second welding) has gas holes and cracks and the indentations on the surface, as shown in Fig. 3. The Cr-C composition is about 61%, according to the EDS analysis, the Fe content of the interface between hardfacing layer A (the second welding) and layer B (the first welding) is about 30~40%, and increased to 50~60% of the interface between layer B and the base. The reason of this phenomenon was that the Cr-C segregation quantity is higher near the surface of hardfacing layer B. After the second welding, the Cr-C in the surface combined with the powder material to produce a compact with lower Fe content Cr-C layer. Although the microstructure of hardfacing layer B is similar to the other hardfacing layer, with the distribution rate of Cr-C around 32%, the quality of the hardfacing, which has become more sloppy with gas hole due to different powder feeding rate, also the layer height was only half of other specimens. As a result, the relationship between the powder feeding rate, layer thickness, and dilution rate can be verified.

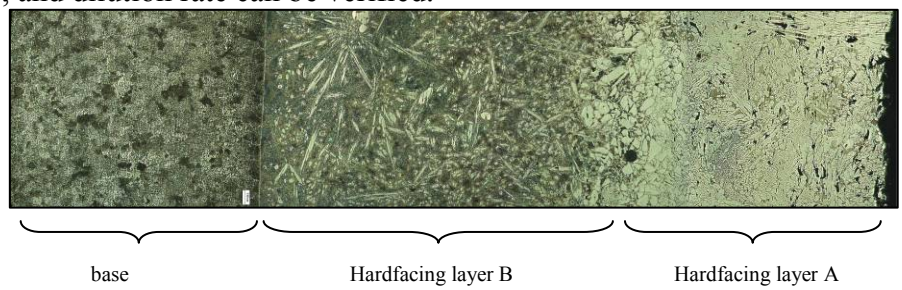

Fig. 3 The microstructure of specimen No.6

The EDS composition analysis of specimen No.1 (sampling location is between the 1/2 hardfacing layer to the surface) is shown in Fig. 4 for example.

Element	Weight %	Atomic %
C K	8.94	30.39
Si K	1.37	2.00
Cr K	37.12	29.15
Mn K	0.87	0.65
Fe K	51.70	37.81
Totals	100.00	

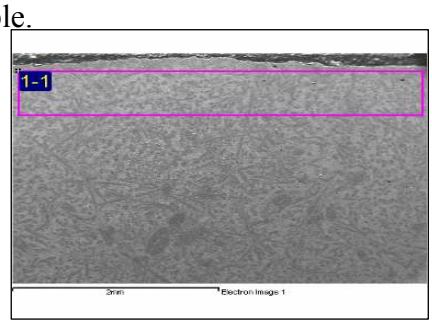

Fig. 4 The EDS composition analysis of specimen No.1

In order to analyze the heat-affected zone of the hardness layer, the cross-sectional hardness distribution was studied and found that the heat-affected zone of the base is not more than 0.2mm away from the interface, as shown in Fig. 5. The cross-sectional hardness distribution curves appeared to be beating, which should be caused by the chromium carbide micro-structures.

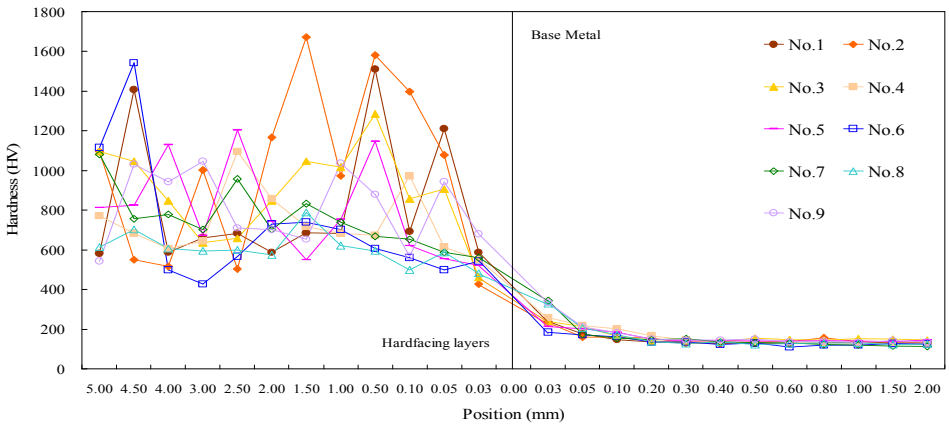

Fig. 5 Cross-sectional hardness distribution of hardfacing layers

Analysis of Surface Hardness

The results of surface hardness are shown in Fig 6. For hardfacing layer, the surface has higher hardness is the better, so the analysis characteristic is "The Larger the Better". By calculating the S/N ratio, categorizing the response tables and graphs, through the variance analysis, to evaluate the contributions of these factors. In Table 4, Torch moving distance (factor D) affects most on the surface hardness. From the main effects plots, the optimized process factors of surface hardness are A3, B1, C3, D1, which are shown in Fig. 7, with the surface hardness up to HRc 59.

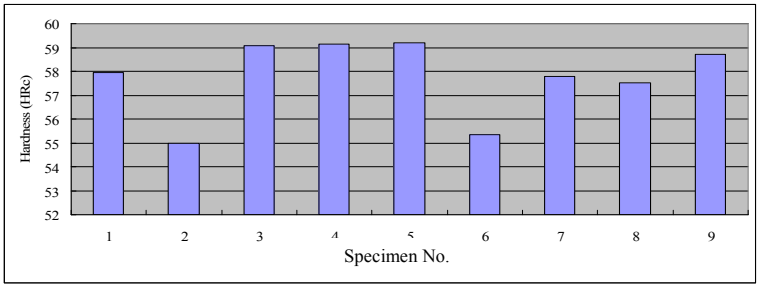

Fig. 6 Results of the surface hardness

Table 4 Factor response table of HRc hardness

Factors / level	A	B	C	D
1	35.15	35.29	35.09	35.35
2	35.23	35.13	35.19	34.95
3	35.25	35.21	35.36	35.33
Delta	0.10	0.16	0.27	0.39
Rank	4	3	2	1

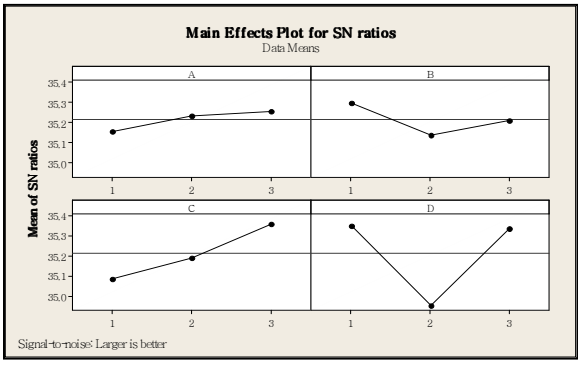

Fig. 7 Factor response graphs of the surface hardness

Analysis of Wear

The layer has fewer wear is better performance, so the analysis characteristic is "The Smaller the Better". The results of wear performance are shown in Fig 8, and prove that the wear-resistance performance of hardfacing layer is 4~5 times higher than the original low-cost steel. In table 5, Torch moving rate (factor C) affects the wear most. From the main effects plots, the optimized process factors of surface hardness are A3, B1, C2, D1, which are shown in Fig. 9.

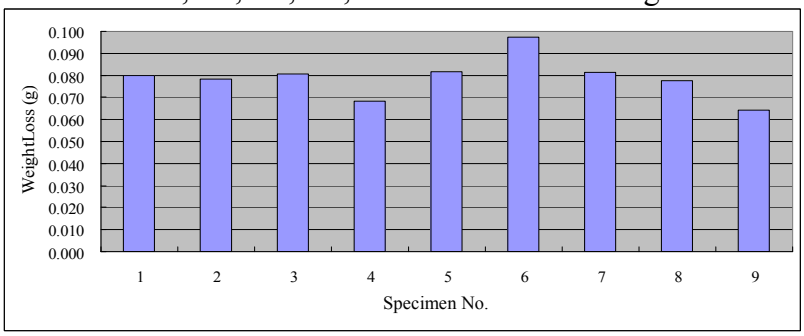

Fig. 8 Results of the wear

Table 5 Factor response of wear

Factors / level	A	B	C	D
1	21.94	22.32	21.42	22.49
2	21.75	21.97	23.08	21.35
3	22.59	21.99	21.77	22.44
Delta	0.84	0.34	1.66	1.14
Rank	3	4	1	2

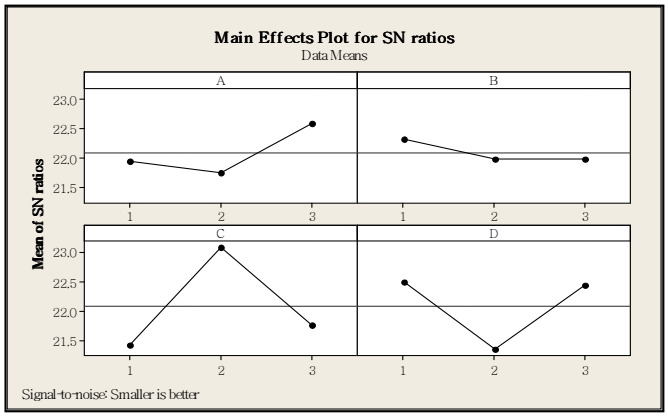

Fig. 9 Factor response graphs of wear

Analysis of Dilution Rate

The analytic location is between the 1/2 thickness of the hardfacing layer and its surface, and the dilution rate of the hardfacing layers is defined by formula (1). The results of dilution rate are shown in Fig. 10 and lower dilution rate means better quality, so the analysis characteristic is "The Smaller the Better". In table 6, Working current (factor A) affects the most on the dilution rate. From the main effects plots, the optimized process factors of surface hardness are A1, B3, C3, D3, which are shown in Fig. 11, with the dilution rate is about 19%.

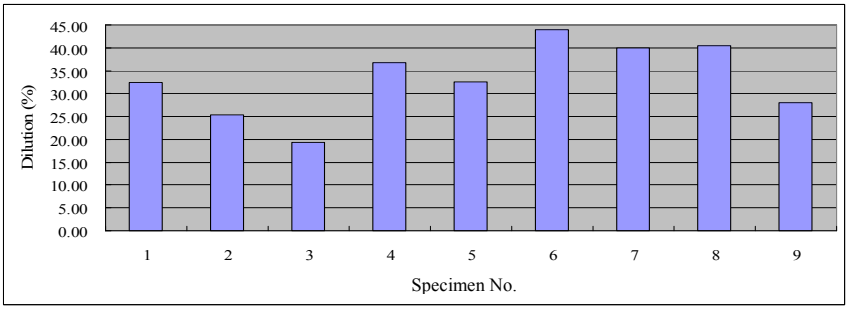

Fig. 10 Results of the dilution rate

Table 6 Factor response table of dilution rate

Factors / level	A	B	C	D
1	-28.03	-31.20	-31.74	-29.81
2	-31.48	-30.17	-29.47	-31.01
3	-31.05	-29.19	-29.35	-29.73
Delta	3.44	2.01	2.39	1.28
Rank	1	3	2	4

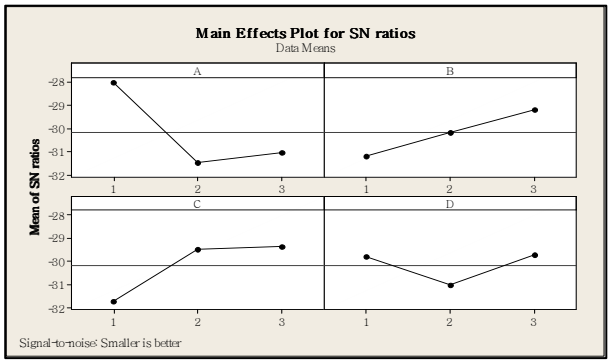

Fig. 11 Factor response graphs of dilution rate

The Optimum Factor Combinations

The analytic results of the S/N ratio give the optimum combinations of the PTA process factors in the tests. In order to further understand how the control factors contribute in different circumstances by variance analysis, the optimum factor combinations were summarized in Table 7 for reference.

Table 7 The optimum factor combinations in the PTA hardfacing process of wear-resistant plate

Parmeter / Optimum combination / Test	Wroking current (Amp)	Power feeding rate (g/min)	Torch moving rate (mm/min)	Torch moving distance (mm)
HRc hardness	A_3:200	B_1:40	C_3:800	D_1:20
Wear	A_3:200	B_1:40	C_2:900	D_1:20
Dilution rate	A_1:180	B_3:50	C_3:800	D_3:30

Conclusions

1. By the observation of the microstructure, the more sturdy and compact the Cr-C dendrite structure , the better the hardness and wear-resistance the hardfacing layers is. Through the cross-sectional hardness distribution analysis, even the thickness of low-carbon steel is only 4 mm; the depth of heat-affected zone can be controlled within 0.2mm by using PTA to produce wear-resistant plate.
2. With the control factors, working current (200A), powder feeding rate (40g/min), torch moving rate (800mm/min), and torch moving distance (20mm), give the optimization of the surface hardness, and the major factor of the surface hardness is the torch moving distance.
3. Under the ASTM G65 test, the process factors configuration, working current (200A), powder feeding rate (40g/min), torch moving rate (900mm/min) and torch moving distance (20mm), give the optimum wear performance, and the major factor of the wear is the torch moving rate.
4. According to formula (1) and Taguchi methodology, with the control factors working current (180A), powder feeding rate (50g/min), torch moving rate (800mm/min) and torch moving distance (30mm), give the optimization of the dilution rate, and the major factor of the dilution rate is the working current.
5. From the microstructure observation of the specimen No.6 (with second welding), the hardfacing layer microstructure becomes more compact, although the gas hole and crack happens more easily. This second welding process may be able to repair or fill the hardfacing layer. More study need to re-evaluate the hardfacing layers' quality with second welding in the PTA process. If the second welding is a successful application, it may not only reduce the cost for expensive alloys, but also can contribute to environmental protection.

Acknowledgements

The authors wish to thank the Ministry of Education, Republic of China, for the financial support under Grant 98E-30-135. Most experiments were conducted with technical supports of Engineering Research and Technology Center (ERTC) of Cheng Shiu University.

References

[1] P. Crook, “Friction and wear of hardfacing alloys”, ASTM Handbook, Friction, Lubrication and Wear Technology, Vol. 18, 1992, pp.758-765.

[2] W. S. Hsu, L. D. Wu, “the Technology and Applications of PTA hardfacing process”, Machinery Monthly, Vol. 21, No. 12, 1995/12, pp.222-228.

[3] AWS, “Plasma Arc Metalworking Process”, 1967.

[4] A. Hasui, E. Kasahara and H. Taguchi, “Studies on Plasma Welding”, Trans. National Research Institute for Metals, 1969, pp.65-72.

[5] R. F. Arnodly, “Bulk Process Welding”, Welding Journal, 42(11), 1963, pp.855-861.

[6] G. H. Reynolds, Kachelmeier, E. J., “Adding powdered metal filler speeds deposition rate”, Metal Construction and British Welding Journal, 10(9), 1978, pp.426-434.

[7] H. Y. Wang, W. B. Xu, K. Zhao, X. B. Qi, Z. G. Cheng, Z. J. Dong, L. Z. Li,“Effective Method of Plasma Arc Powder surfacing to Achieve both High Deposition Rate and Low Ratio of Dilution”, Welding, Vo.6, 2002, pp.27-29.

[8] C. Y. Su, C. B. Chou, “the Principle and Applications of Plasma Spray Technology”, Machinery Monthly, Vol. 21, No. 12, 1995/12, pp.177-190.

[9] T. K. Kao,“the Hardfacing Application in the Steel Plant”, Technology and Training , Vol.21, No.6, 1996/12, pp.37-42.

[10] R. L. Deuis, C. Subramanian and J. M. Yellup, “Metal-matrix Composite Coating by PTA Surfacing”, Composites Sci. Tech., 58, 1998, pp.299-309.

[11] M. Hur, T. H. Hwang, W. T. Ju, C. M. Lee and S. H. Hong, “Numerical Analysis and Experiments on Transferred Plasma Torches for Finding Appropriate Operating Conditions and Electrode Configuration for a Waste Melting Process”, Thin Solid Films, 390, 2001, pp.186-191.

[12] L. Bourithis, A. Milonas and G. D. Papadimitriou, “Plasma Transferred Arc Surface Alloying of a Construction Steel to Produce a Metal Matrix Composite Tool Steel with TiC as Reinforcing Particles”, Surface Coat. Tech., 165, 2003, pp.286-295.

[13] L. Bourithis and G. D. Papadimitrio, “Synthesizing a Class "M" High Speed Steel on the Surface of a Plain Steel Using the Plasma Transferred Arc (PTA) Alloying Technique: Microstructural and Wear Properties”, Mater. Sci. Eng. A, 361, 2003, pp.165-172.

[14] Y. Liu, Q. Y. Li, “Measures for Improving Quality of Forgeable Piece for Gear Shaft”, Hot Working Technology, No. 12, 2004, pp.48-51.

[15] Y. C. Yen, “Microstructural Feature and Erosion Wear Behavior of PTA-overlayed NbC on Pure Ti”, Master Thesis, Department of Materials Science and Engineering, National Cheng Kung University, Taiwan, R.O.C, 2004.

[16] D. Y. He, B. Y. Fu, J. M. Jiang, X. Y. Li, Z. H. Wang, Z. X. Li,“Abrasive Resistance of Arc Sprayed Coatings with a WC Ceramic Phase”, Tribology, Vol. 27, No.2, Mar. 2007, pp.116-120.

[17] R.V. Sharples, “The Plasma Transferred Arc (PTA) Weld Surfacing Process”, The Welding Institute of U.K., Sept. 1985.

[18] H. S. Chen, H. S. Ho, H. K. Kung, J. C. Hsiung, “An improvement of hardfacing gap control mechanism of Plasma Transferred Arc welding process with constant power rate”, Taiwan Patent M 346477, 2008.

[19] ASTM G65-94(Reapproved 2000),“Standard Test Method for Measuring Abrasion Using the Dry Sand/Rubber Wheel Apparatus”, Annual book of ASTM standards, American Society for Testing and Materials (ASTM), Vol. 03.02, 2000, pp.249-260.

Advanced Materials Research Vols. 314-316 (2011) pp 94-97

doi:10.4028/www.scientific.net/AMR.314-316.94

A new processing way for helicoid reflective mirror

Shaolei Hu [1,2,a], Yongjun Xie[1,b], and Xin Zhao[1,2,c]

[1.] State Key Laboratory of Transient Optics and Photonics, Xi'an Institute of Optics and Precision Mechanics, Chinese Academy of Science (CAS), Xi'an, 710119, China

[2.] Graduate University of Chinese Academy of Sciences, Beijing 100049, China

[a] hushaolei0301@sina.com [b] yjxie@opt.ac.cn [c] zhaoxin19840302@163.com

Key words: Helicoid, Reflective mirror, B270 glass, Three-coordinate measuring machine.

Abstract. A novel processing way for the continuous helicoid reflective mirrors is proposed. We use an intelligent oven to accurately control the glass temperature and successfully produce a helicoid reflective mirror in B270 glass. Then we test the shape and optical properties of the helicod reflective mirror via the three-coordinate instrument measuring and interference experiment.

Introduction

Because of extensive application in engineering design and mechanical manufacturing, the helicoids have been extensively investigated in the past few years [1- 4]. For example, the helicoids always exist in gear, thread, worm, screw pump, metal cutting tools, and so on. With the development of science and technology, the design and manufacturing of helicoids become more simple and accurate by using the CAD/CAM and advanced devices [5, 6]. Especially, the complex helicoids which can not be achieved by the conventional machine, but they can be processed by inputting the simply programs into the numerical control (NC) machine [7]. However, as far as we know that it is difficult to process the helicoid reflective mirrors by this method.

The helicoid reflective mirrors have the widespread applications of optical vortices and optical delay lines, which have generated an immense interest now [8, 9]. R. K. Tyson et al have reported a method for creation of optical vortices by using a deformable mirror and C. L. Wang et al have introduced a straight helicoid mirror to a periodic optical delay device. Whereas, deformable mirrors and segment mirrors generate phase variation is not continues but varies in discrete steps.

In this paper, a novel processing way for the continuous helicoid reflective mirrors is proposed. We use an intelligent oven to control the glass temperature and successfully produce a helicoid reflective mirror in B270 glass. Then we test the shape and optical properties of the helicod reflective mirror via the three-coordinate instrument measuring and interference experiment.

The helicoid design

The helicoid is formed by a straight line generatrix screwed around an axis, and tangent to a cylinder concentric to this axis. The inclination of generatrix is such that it is the tangential continuation of the helix described by the point of the generatrix that touches the concentric cylinder, figure 1 depicts the shape and parameters of the helicoid.

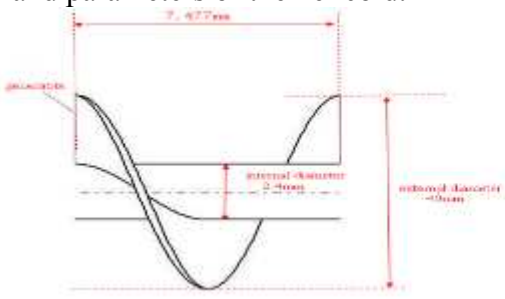

Fig. 1 The shape and parameters of the helicoid

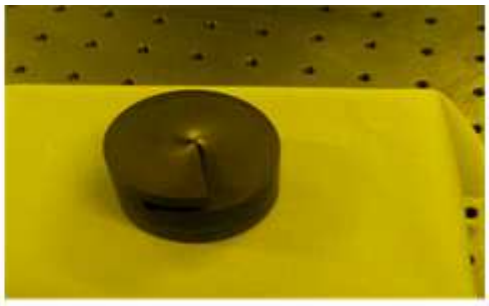

Fig. 2 A processed helicoidal base

The processing of the helicoid reflective mirror

In order to get a helicoid reflective mirror, we need fabricate helicoidal base in copper. The base can be processed according to the helicoid design above. Fig. 2 shows a processed helicoidal base.

After that, Owing to considerable advantages in optical, thermal and mechanical properties, we employ the B270 glass to be the material of the helicoid reflective mirror. Table 1 shows the technical parameters of the B270 glass. Fig. 3 shows the light performance of the B270 glass.

Tabe1 The technical parameters of the B270 glass

Number	Thickness(mm)	λ_{tj}(nm)	λ_o(nm)	$T_{\lambda o}$(%)	K
B270	2	310±10	400	≥89.5	≥1.0

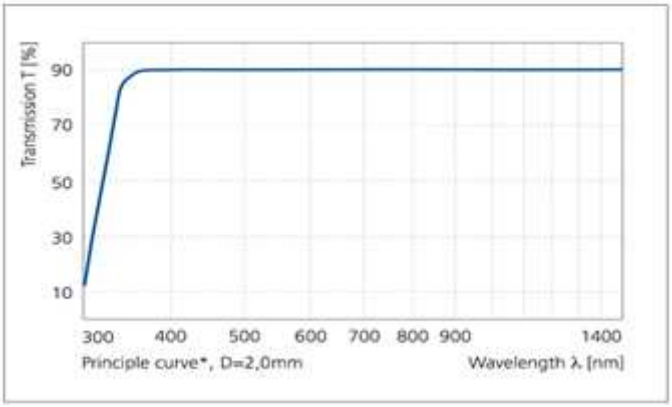

Fig. 3 The light performance of the B270 glass

The beeswaxes are used for sticking the B270 glass and the helicoidal base, which have advantages of the melting point is about 65 ℃, the oil content is as low as 10 %, and the chroma number is as low as 8. Especially, the beeswaxes are odorless, non-metallic inclusions, anhydrous adhesive which suitable for sticking between precision components.

The adhesive substance of B270 glass and the helicodal base is grinded into a 40 mm external diameter and 2.4 mm internal diameter of glass ring. And then the glass ring is carved by using a rotary slice which need water cooling in the process. At last, the processed glass dipped in the gasline for getting rid of beeswaxes.

Since these procedures have been done, we put the adhesive substance of B270 glass and the cleaned helicoidal base into an intelligent oven. The appropriate programs have been used for heating, retaining, and cooling temperature. After repeated experiments we have find the best control program, Fig. 4 shows the relation between heating time and temperature of glass.

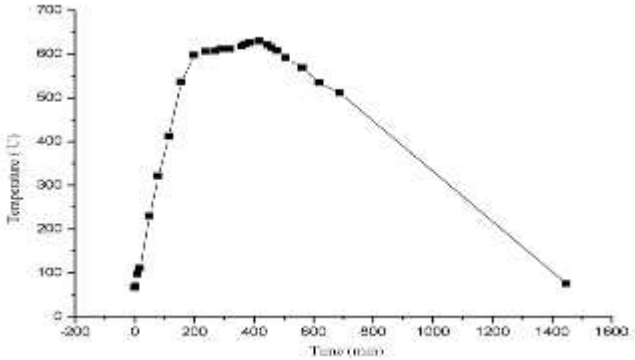

Fig. 4 The relation between heating time and temperature of B270 glass

The process of heating and cooling is very important during the firing, which needs a long time. When the process of the heating is too short, the glass may be broken because of the big difference between the B270 glass and the helicoidal base; When the process of the cooling is too short, quality of the helicoid reflective mirror may be very bad because the glass has not enough time to fuse with the helicoidal base. Finally, we get a helicoid reflective mirror which is showed in Fig. 5.

Fig. 5 The processed helicoid reflective mirror

Fig. 6 The three-coordinate instrument measuring

Evaluation the helicoid reflective mirror

The shape of the helicoid reflective mirror is tested by using the three-coordinate instrument measuring with high precision. The three-coordinate instrument measuring has many functions of scanning, touch trigger, non-contact optical probe. Therefore it is appropriate to test complex contour and shape surface with high precision. Fig. 6 shows the shape structure of three-coordinate instrument measuring.

We pick out 238 measuring points from the processed helicoid reflective mirror by using three-coordinate instrument measuring, and every point has four value which include Z-axis, polar angle, and polar radius value. These points are connected by using the MATLAB.

There are a little differences between the theoretical and measured value, but the reflective mirror is feasiable within tolerance, as shown in Fig. 7.

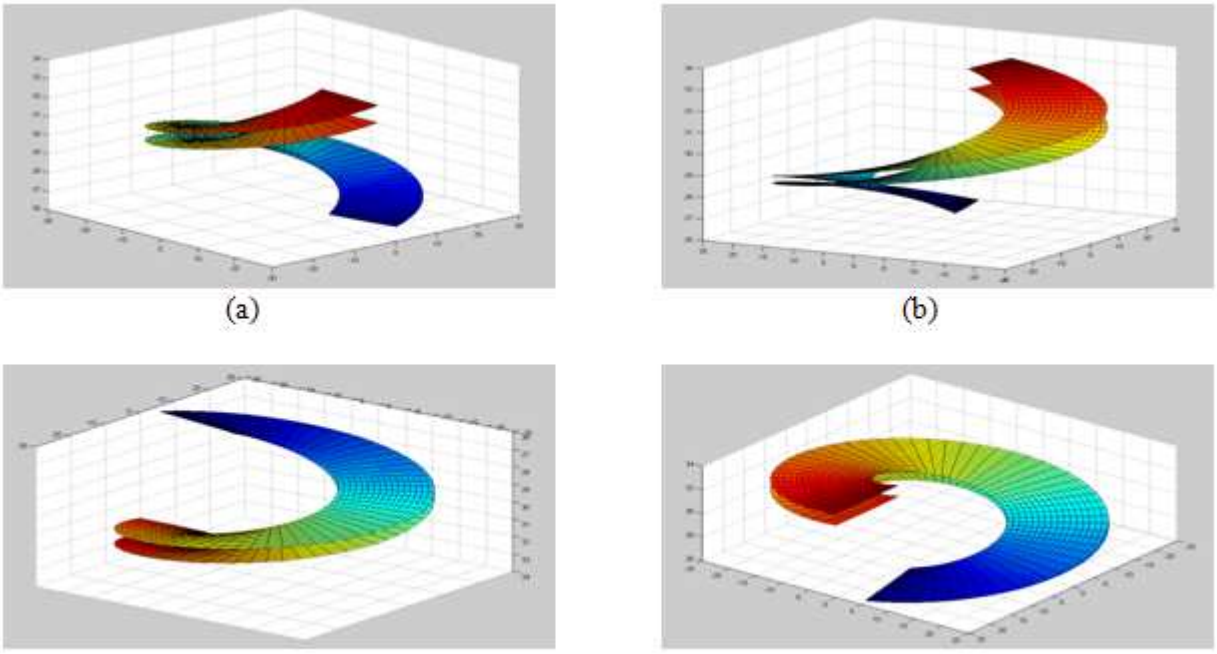

Fig.7 The helicoid reflective mirror synthesized by theoretical and measured value at different rotation angle

Interferometric techniques are used for testing the optical properties of the helicoid reflective mirror. Fig. 8 depicts the experimental scheme for testing the helicoid reflective mirror. The helicoid reflective mirror has a good optical quality, as shown in Fig. 9.

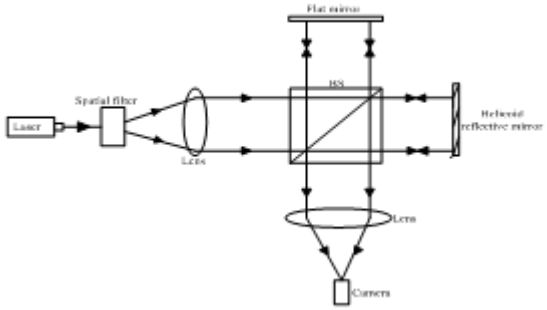

Fig. 8 Experiment scheme for testing the helicoids reflective mirror

Fig. 9 Interference result of the helicoid reflective mirror

Conclusion

In conclusion, we propose a novel processing way for the helicoid reflective mirror and successfully produce a helicoid reflective mirror in B270 glass. Then we test the shape and the optical properties of the helicoid reflective mirror via the three-coordinate instrument measuring and the interference experiment. Although there are a little differences between the theoretical and measured value, the helicoid reflective mirror is feasible within tolerance, moreover, the helicoids reflective mirror has a good optical quality.

Acknowledgement

This work was supported by National Nature Science Foundation of China under Grant 60878034 and National High Technology Research and Development Program of China.

References

[1] G. A. S. M. Ribeiro, D. Lopes, O. R. D. Vale, U.S. Patent 6,036,749. (2000).

[2] P. Berger, C. D. Choudens, G. Lombardo, P. Monzie, U.S. Patent 4,088,528.(1978).

[3] F. Pernack, S. F. Miller, E. Z. Krygier, and A. B. Abrahamsson, U.S. Patent 3,299,577 (1967).

[4] A. H. Candee, E. Wildhaber, U.S. Patent 125,232 (1937).

[5] D. S. Sheth , and S. Malkin: International Journal of Machine Tools and Manufacture. 36 (1990) 129-132.

[6] S. K. Kang, K. F. Ehmann, and C. Lin： International Journal of Machine Tools and Manufacture. 36 (1996) 141-153.

[7] Y. Tsai, J. Hsieh: Journal of Materials Processing Technology. 117 (2001) 183-192.

[8] R. K. Tyson, M. Scipioni, and J. Viegas: App. Opt. 47 (2008) 6300-6306.

[9] CL. Wang, CL. Pan, U.S. Patent 5,907,423 (1999).

Advanced Materials Research Vols. 314-316 (2011) pp 98-101

doi:10.4028/www.scientific.net/AMR.314-316.98

Effect of Working Current on Microstructure and Properties of Cylinder Hardened by Plasma Beam at Junction of the Hardening Traces

Li Yang[1,2,a], Yinghuai Qiang[1,b], Fushan Chen[2,a], Yang Gao[2,a] and Yuntian Zhong [2,a]

[1]School of Materials Science & Engineering China University of Mining and Technology Xuzhou China 221116

[2]Mechanical and Electronic Engineering Department Xuzhou Institute of Technology Xuzhou, China 221008

[a] linlideyu@126.com, [b] yhqiang@cumt.edu.cn

Keywords: Cylinder; working current; plasma beam; junction; properties

Abstract. To improve wear resistance and service life of boron cast iron cylinder, plasma beam hardening on surface is adopted.Scanning electron microscope,X-ray diffractometer and micro-hardness tester is used to analyze the effect of working current on the structure and properties of plasma beam hardening layer at the junction of the hardening traces. The results show that the microstructure of hardening layer at the junction is hidden acicular martensite, retained austenite and flake graphite. With the increase of working current, the content of retained austenite decreases, the hardness and depth of the hardening layer increases. The highest hardness is not achieved at the surface of hardening layer but at the second-surface layer which has a certain distance to the surface. The uneven distribution of hardness in hardening layer leads to large gradient at the both sides of the highest hardness and the gradient decreases with the increase of working current.

Introduction

As key part of engine, cylinder's service life has a great relationship with the reliability of engine. Because of the bad working conditions, the main failure of cylinder is wear. Especially the abnormal wear on the surface has great impact on cylinder. If the wear value exceed an allowing standard, blow-by and oil expelling will emerge, the power and economy of diesel engine will decline seriously [1-2].

In order to improve part's wear resistance and service life, high-energy beam heat treatment such as laser, plasma beam is used. After the treatment, phase transformation or micromelted-solidified modification can be obtained on the surface of part and its mechanical properties increase largely [1 ~ 4]. At present, cylinder with diamond grid shape hardening traces is often used as shown in figure 2. Only thus can the high energy beam hardening strap play their functions of high hardness and high wear-resistance, and the washboard effect is avoided.

But such hardening traces have trace junctions. In papers of [5] and [6], some basic studies have been carried out to confirm whether microstructure and property of hardening layer at junctions is damages to the wear resistance. Therefore, it is important to research the structure and hardness distribution of hardening layer at junctions of hardening traces of boron cast iron cylinder.

The chemical composition, microstructure and properties of boron cast iron

Boron cast iron is melted in cupola and the pouring temperature is between 1470℃ and 1480 ℃ .After the inoculation with 75SiFe, the specimens of 95-cylinder are poured with horizontal centrifugal casting. The specimens contain 3.19% C, 2.34%Si, 0.69%Mn, 0.24%P, 0.12%S,and 0.07B. It can be seen in Fig.1 that the metallographic microstructure as cast state is pearlite + ferrite + some free ferrite +some eutectic cell + some compound boride. The iron's tensile strength meets the requirement of HT250 and$\sigma_b \geq 250$MPa, the hardness is 230 ~ 240 HBS.

Test method

The plasma surface treatment test is carried out on numerically-controlled plasma cylinder hardening equipment of DGR- III type which takes argon gas as protection gas. The cylinder is hardened with the cylinder's rotary motion and the plasma torch's linear movement. So the meshed hardening traces forms on the inside wall of cylinder(Fig.2).The protection gas flow is $0.7m^3/h$. Working current, scanning rate and wave head are adjustable. In the test, with constant parameters of arc voltage (50V), scanning rate (70), wave head counts(16), whereas the working current is increased form 50A to 90A, the effects of working current on the depth, hardness and structure on junction B–B of hardening layer is studied. To get the exactly change rule of depth, hardness and structure of hardening layer at different working currents, the JOT80-1 CNC wire cutting equipment is used to get vertical intercepted sample along A-A and B-B (Fig. 2), single-channel and junction hardening strap are get separately. The depth, hardness and structure of hardening layer at single-channel and junction is examined with HV-1000-based digital vickers hardness tester and CMM-22 metallographic microscope, and the X-type of PertMPDpro X-ray diffractometer is used to analyze the phase of hardening strap.

Experimental results and analysis

Structural analysis of hardened layer. The appearance of single-channel (A-A) and junctions (B-B) on hardening layer are both bright white, the structure is hidden acicular martensite + retained austenite + flake graphite + broide (Fig. 3) .The reason is summed up as follows: the temperature and energy density of plasma beam are very high, so with fast heating rate($> 5\times10^3$℃/ s)and high superheat degree, the cylinder's surface can be heated above the phase transition temperature in a very short time, which lead to a high nucleation rate of austenite, but the short heating time and residence time above phase transition temperature (< 100ms) made the austenite has not enough time to grow up and homogenize, thus forming a uniform fine grain structure of austenite. In the subsequent rapid cooling (cooling rate> 10^4°C / s) process, most of austenite transforms into hidden acicular marstentie , the rest is exist in the form of retained austenite[5].

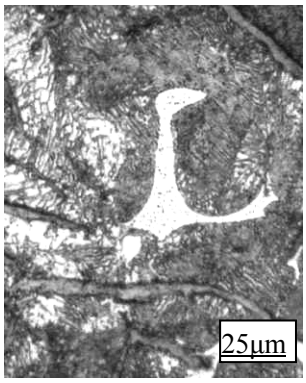

Fig.1 Microstructure of boron cast iron

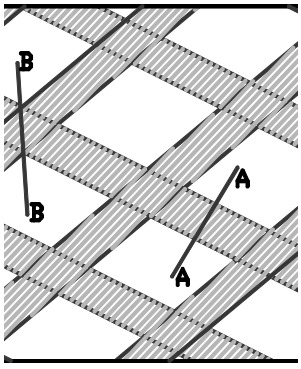

Fig.2 Hardening layer trajectory and sampling sites

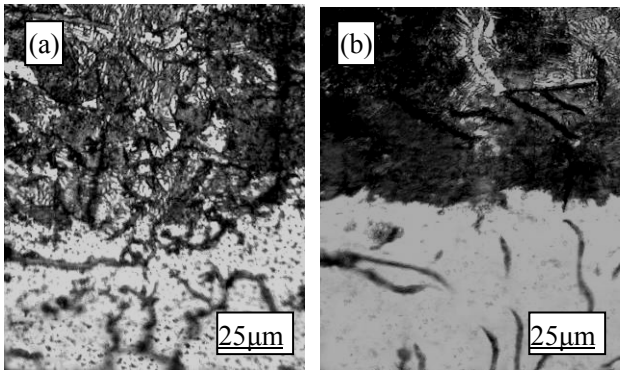

Fig.3 The structure of single-channel (a) and junctions (b) on hardening layer

The effects of working current on residual austenite content on hardening layer surface. The quantitative analysis of hardened samples is made with an appropriate diffraction angle at 1.2 o/ min scanning speed. The analysis and calculation uses G factors, and the sum of martensitic phase content and the retained austenite phase content is thought as 100%. The quantitative analysis result is shown in Table 1.

It is clear that with the increase of working current, the content of retained austenite decreases. This is due to plasma beam surface hardening belonging to a short time quenching; the holding time of hardening is a primary factor in the course of the formation of hardening layer. But in the case of rapidly heating, no matter how much the working current, the surface of the plasma beam hardening traces has basically all austenitizing. With the increase of working current, heating rate increases,